Design and Implementation of Magnetic Bearings in Rotary Blood Pump

by

Haris Sheh Zad

A Dissertation Submitted to the
Graduate School of Sciences and Engineering
in Partial Fulfillment of the Requirements for
the Degree of

Doctor of Philosophy

in

Electrical & Electronics Engineering

KOÇ
UNIVERSITY

August 2017

Design and Implementation of Magnetic Bearings in Rotary Blood Pump

Koç University

Graduate School of Sciences and Engineering

This is to certify that I have examined this copy of a doctoral thesis by

Haris Sheh Zad

and have found that it is complete and satisfactory in all respects,

and that any and all revisions required by the final

examining committee have been made.

Committee Members:

Prof. Dr. Alper Erdoğan, (Advisor)

Prof. Dr. Ismail Lazoğlu,(Co-Advisor)

Sedat Nizamoglu

Asst. Prof. Dr. Sedat Nizamoğlu

Kaan Güven

Assoc. Prof. Dr. Kaan Güven

Assoc. Prof. Dr. Çetin Yılmaz

Asst. Prof. Dr. Ali Fuat Ergenç

Date: August 17, 2017

DEDICATIONS

To my Parents

ABSTRACT

Magnetic bearings have applications in the fields of moment wheels, molecular pumps, high speed motors, flywheel energy storage systems and ventricular assist devices. They have the advantages of non-contact operation, lower friction, less heat generation and less power consumption as compared to the conventional mechanical bearings. There are two types of the magnetic bearings, *active magnetic bearings* and *passive magnetic bearings*. Passive magnetic bearings make use of permanent magnets to generate the bearing forces. Their advantage is that no electrical power is needed for their operation and also easier control of the bearing stiffness and damping. Passive magnetic bearings can stabilize a rotor in only four out of five degrees of freedom. Therefore, active control is needed in the fifth degree of freedom to completely stabilize the rotor. Electromagnets are used for the operation of active magnetic bearings. The combination of these two types is known as the *hybrid magnetic bearings*. Hybrid magnetic bearings are used in the blood pumps, vacuum pumps, and machine tools etc.

For designing the hybrid magnetic bearings, the distribution of the magnetic fields across the electromagnets and the permanent magnets is a major factor because the damping and the stiffness of the hybrid magnetic bearings depend upon the strength of the magnetic field. However, the measurement of the magnetic flux density is not easier because of the smaller airgaps between the rotor and the stator. Also, the damping and the stiffness are nonlinearly related to the control currents, magnetic flux and the airgaps. For designing the magnetic bearings, magnetic circuit method is used widely. However, in this method, the leakage flux, eddy currents, effects of fringing, the hysteresis effects, reluctances and the nonlinearities are ignored. As there are lot of assumptions and simplifications involved in the magnetic circuit method, the models obtained through this method do not provide the exact distribution of the magnetic fields. Also, the damping and the stiffness obtained through this method have low precision. Therefore, a field method more precise than the magnetic circuit

method should be used for designing the hybrid magnetic bearings. Finite element Method (FEM) analysis is based on numerical tools. As compared to the magnetic circuit method, the models obtained using FEM analysis are more identical to the corresponding physical prototype system.

In this research, a hybrid magnetic bearing prototype setup is designed using the FEM analysis. The damping, stiffness, magnetic flux distribution, forces in the radial and axial direction, the number of turns and the current for the electromagnets are optimized using FEM analysis. Based upon the optimization performed, a prototype setup is manufactured and the different properties of the hybrid magnetic bearing prototype are experimentally verified.

The control of the magnetic bearing system is a critical problem in the presence of the disturbances, unmodeled dynamics and nonlinearities. The classical control techniques such as PID control cannot give robustness against theses disturbances and parameter variations. Therefore, an advanced adaptive sliding mode controller is designed for the hybrid magnetic bearing system and experimentally applied to the prototype setup to see the effectiveness of the designed controller.

The third-generation axial flow blood pumps utilizing the magnetic bearings suffer from the problem of longer rotor size in the axial direction. The rotor of the axial flow pump resembles a column, therefore only one magnetic bearing cannot stabilize the rotor in the tilt direction and in the radial direction. At least two radial magnetic bearings are needed for the axial flow pump to fully stabilize the impeller of the pump with additional motor unit as well to rotate the impeller. Also, at least two bearingless motor units are required for the complete operation of the third-generation axial flow pumps.

The aim of this research is to design a third-generation axial flow blood pump using only one bearingless motor unit for the rotation as well the levitation of the impeller. The computational fluid dynamics (CFD) analysis is performed in order to optimize the design of the impeller and overall pump system. An enclosed impeller based rotor system is proposed based upon the optimization performed, in which the rotor axial length is much smaller as compared to the diameter of the rotor. Therefore, only one bearingless motor system is required for the complete operation of the pump.

Generally, eddy current sensors are used for measuring the rotor radial position in the bearingless brushless DC motors and bearingless permanent magnet synchronous motor systems, while Hall Effect sensors are used for measuring the rotor angular position. The eddy current sensor's application in the proposed optimized design of the third-generation blood pump is not possible due to the much smaller diameter of the pump. Therefore, a sensor system must be developed in order to measure the radial position of the rotor in the proposed design.

In this research, a novel design for the rotor assembly of the novel blood pump is proposed, in which the rotor radial position is measured with the linear Hall Effect sensors in addition to the rotor angular position. The working principle of the sensor assembly is explained in detail and the rotor control system is explained based upon the Hall Effect radial position sensors. Finite element analysis of the novel design of bearingless motor for the miniature axial flow blood pump is also performed. The passive and active stiffness, damping, magnetic flux distribution, forces and currents are obtained through the finite element analysis and compared with the experimental data. The results obtained through finite element analysis show a good agreement with the experimental data. An experimental setup of the designed bearingless motor system is manufactured. The performance of the proposed bearingless permanent magnet motor is evaluated under various test conditions.

The designed adaptive controller is applied to the novel design of the bearingless motor in which the radial direction displacement of the rotor is measured using Hall Effect sensors. There are two permanent magnet rings in the rotor assembly, one ring is used for measuring the rotor radial direction displacement and one ring is used for generating the

torque for the bearingless motor and the radial bearing forces. Therefore, strong magnetic coupling exists in the rotor system and accurate radial position is required for the advanced controller implementation. Therefore, the radial position of the rotor is first adaptively estimated and then a sliding mode controller is designed for the position control of the proposed bearingless motor system. The simulation and experimental results show better position tracking of the proposed bearingless motor using the designed adaptive controller as compared to the classical control techniques.

ÖZET

Manyetik rulmanların moment tekerlekleri, moleküler pompalar, yüksek hızlı motorları, volan enerji depolama sistemleri ve ventriküler yardımcı cihazlar gibi alanlarda uygulamaları bulunmaktadır. Geleneksel mekanik rulmanlara kıyasla temassız çalışma prensibi daha düşük sürtünme, daha az ısı üretimi ve daha az güç tüketimi avantajlarını beraberinde getirir. Manyetik rulmanların iki tipi vardır: *aktif manyetik rulmanlar* ve *pasif manyetik rulmanlar*. Pasif manyetik rulmanlar rulman kuvvetlerini üretmek için kalıcı mıknatıslardan yararlanmaktadır. Avantajları arasında çalışma için herhangi bir elektrik enerjisine ihtiyaç duyulmaması ve rulman rijitlik ve sönümlemesinin daha kolay kontrolü bulunur. Pasif manyetik rulmanlar, bir rotoru beş serbestlik derecesinin sadece dördünde dengeleyip sabit hale getirebilir. Bu nedenle, rotorun tamamen stabilize edilmesi için beşinci serbestlik derecesinde aktif kontrol gereklidir. Aktif manyetik rulmanların çalışmasında ise elektromıknatıslar kullanılır. Bu iki tip rulmanın kombinasyonu *hibrit manyetik rulman* olarak adlandırılır. Hibrit manyetik rulmanlar kan pompalarında, vakum pompalarında ve üretim tezgâhı takımlarında kullanılmaktadır.

Hibrit manyetik rulmanların tasarımı için manyetik alanların elektromıknatıslar ve sürekli mıknatısların arasında dağılımı önemli bir faktördür, çünkü hibrit manyetik rulmanların sönümlenmesi ve sertliği manyetik alanın toplam gücüne bağlıdır. Bununla birlikte, manyetik akı yoğunluğunun ölçümü, rotor ve stator arasında daha küçük hava boşlukları bulunması nedeniyle kolay değildir. Ayrıca, sönümleme ve rijitlik; kontrol akımları, manyetik akı ve hava boşlukları ile doğrusal olmayan bir şekilde ilişkilidir. Manyetik rulmanların tasarımı için manyetik devre yöntemi yaygın olarak kullanılmaktadır. Ancak bu yöntemde kaçak akı, girdap akımları, saçaklanma etkisi, histerezis etkileri, isteksizlik ve doğrusalsızlık faktörleri dikkate alınmaz. Manyetik devre yönteminde birçok varsayım ve basitleştirme olduğu için, bu yöntemle elde edilen modeller manyetik alanların

kesin dağılım bilgisini sağlamazlar. Ayrıca, bu yöntemle elde edilen sönümlenme ve sertlik düşük hassaslığa sahiptir. Bu nedenle, manyetik devre yönteminden daha hassas bir manyetik alan yöntemi, hibrit manyetik rulmanların tasarımı için kullanılmalıdır. Sonlu Elemanlar Yöntemi (FEM) analizi sayısal araçlara dayanmaktadır. Manyetik devre yöntemi ile karşılaştırıldığında, FEM analizi kullanılarak elde edilen modeller, ilgili fiziksel prototip sisteme özdeşlik bakımından daha yakındır.

Bu araştırmada, bir hibrit manyetik rulman prototipi kurulumu FEM analizi kullanılarak tasarlanmıştır. Sönümleme, sertlik, manyetik akı dağılımı, radyal ve aksiyal (axial) yöndeki kuvvetler, dönüş sayısı ve elektromıknatıslar için akım FEM analizi kullanılarak optimize edilmiştir. Yapılan optimizasyona dayanarak, bir prototip kurulumu üretilmiştir ve hibrit manyetik rulman prototipinin farklı özellikleri deneysel olarak doğrulanmıştır.

Manyetik rulman sisteminin kontrolü; sistem bozuklukları, modellenmemiş dinamikler ve doğrusal olmayan etkiler varlığında kritik bir sorundur. PID kontrolü gibi klasik kontrol teknikleri, bu bozulmalara ve parametre değişimlerine karşı sağlam bir çözüm sağlayamamaktadır. Bu nedenle, gelişmiş bir adaptif kayma modu denetleyicisi, hibrit manyetik rulman sistemi için tasarlanmış ve denetleyicinin etkinliğini görmek için deneysel olarak prototip kurulumuna uygulanmıştır.

Manyetik rulmanları kullanan üçüncü nesil aksiyal akışlı kan pompalarının, aksiyal yönde normalden uzun rotor boyutları barındırmaları bir problem teşkil etmektedir. Eksenel akış pompasının rotoru bir sütun şeklindedir ve bu nedenle yalnızca tek bir manyetik rulman, rotoru eğilme yönünde ve radyal yönde dengeleyemez. Pervanenin kendisini döndürmek ve ilave motor ünitesi ile pompanın pervanesini tam olarak dengelemek için, aksiyal akış pompasının en azından iki adet radyal manyetik rulmana sahip olması gereklidir. Ayrıca, üçüncü nesil aksiyal akışlı pompaların tamamen çalışabilmesi için en az iki adet rulmansız motor birimi gereklidir.

Bu araştırmanın amacı, çarkın dönme ve havaya kaldırılma işlemi için sadece bir adet rulmansız motor birimi içeren, üçüncü nesil aksiyal akışlı bir kan pompası tasarlamaktır. Pervanenin ve toplam pompa sisteminin tasarımını optimize etmek için hesaplamalı akış dinamikleri (CFD) analizi yapılmıştır. Yapılan optimizasyona dayanarak, rotor aksiyal uzunluğunun rotor çapından çok daha küçük olduğu kapalı bir pervane bazlı rotor sistemi önerilmektedir. Bu nedenle, pompanın komple çalışması için sadece bir adet rulmansız motor sistemi gereklidir.

Genel olarak, girdap akım sensörleri, rulmansız ve fırçasız DC motorlarda ve rulmansız sabit mıknatıslı senkron motor sistemlerinde, rotorun radyal konumunu ölçmek için kullanılırken, Hall Efekt sensörleri rotorun açısal konumunu ölçmek için kullanılır. Üçüncü nesil kan pompasının önerilen optimize edilmiş tasarımında girdap akım sensörünün kullanılması, pompanın çok daha küçük çapı olması nedeniyle mümkün değildir. Bu nedenle, önerilen tasarımdaki rotorun radyal konumunu ölçmek için bir algılayıcı sistemi geliştirilmelidir.

Bu araştırmada, rotorun radyal ve açısal konumunun doğrusal Hall Efekti sensörleri ile ölçülmekte olduğu, yeni bir kan pompasının rotor düzeneği için yeni bir tasarım önerilmiştir. Sensör grubunun çalışma prensibi ayrıntılı olarak açıklanmış ve rotor kontrol sistemi, Hall Efekt radyal konum sensörlerine dayanılarak açıklanmıştır. Minyatür aksiyal akışlı kan pompası için rulmansız motorun yeni tasarımının sonlu elemanlar analizi (FEM) de yapılmıştır. Pasif ve aktif rijitlik, sönümlenme, manyetik akı dağılımı, kuvvetler ve akımlar; sonlu elemanlar analizi ile elde edilmiş ve bu simülasyon verileri, deneysel elde edilmiş veriler ile karşılaştırılmıştır. Sonlu elemanlar analizi ile elde edilen sonuçların deneysel veriler ile iyi bir uyum gösterdiği gözlemlenmiştir. Tasarlanan motor sisteminin deneysel bir düzeneği üretilmiştir ve önerilen rulmansız sabit mıknatıslı motorun performansı, çeşitli test koşulları altında değerlendirilmiştir.

Tasarlanan adaptif kontrol cihazı, rotorun radyal yöndeki yer değişiminin Hall Efekti sensörleri ile ölçüldüğü rulmansız motorun yeni tasarımına uygulanmıştır. Rotor düzeneğinde iki sabit mıknatıs halkası bulunmaktadır. Bu halkalardan biri rotorun radyal yönünün yer değiştirmesini ölçmek için kullanılırkenö diğer halka da rulmansız motor ve radyal rulman kuvvetleri için tork üretimini sağlamaktadır. Bu nedenle, rotor sisteminde kuvvetli manyetik kuplaj mevcuttur ve gelişmiş kontrolör uygulaması için doğru radyal pozisyon bilgisi gerekmektedir. Bu nedenle, rotorun radyal konumu ilk önce adaptif olarak tahmin edilmektedir ve buna bağlı olarak önerilen rulmansız motor sisteminin pozisyon kontrolü için bir sürmeli mod kontrolörü tasarlanmıştır. Simülasyon ve deney sonuçları, klasik kontrol tekniklerine kıyasla, tasarlanmış uyarlanabilir kontrol cihazı kullanılan rulmansız motorun, daha iyi konum takibini başardığını göstermiştir.

ACKNOWLEDGEMENTS

First and Foremost, I would like to express my sincere gratitude to Prof. Dr. Ismail Lazoğlu for providing me with an excellent opportunity to work in a very dynamic research center (MARC). Without his utmost support, this research wouldn't be possible. I really appreciate his motivation, patience and immense knowledge. His guidance helped me in all the time of my research and writing of this thesis.

I would like to thank Prof. Dr. Alper Erdoğan, Prof. Dr. Sedat Nizamoğlu, Prof. Dr. Kaan Güven for their time, guidance and effort for the evaluation of my thesis. Furthermore, I would like to thank my friend and project partner Talha Irfan Khan for helping me to bring the project to this stage by working day and night for the past 4 years. Additionally, I am thankful to KOC University Istanbul, Turkey and Higher Education Commission, Pakistan for providing me funding for the accomplishment of my PhD degree.

I would like to thank my family for believing in me and taking care of my responsibilities at home, especially my Parents, and my brothers Adil Zohaib and Sultan Farhad Pasha for missing me a lot during this time.

I specially thanks to Abasin Ulasyar for helping me get through the difficult times, and for all the emotional support, entertainment, camaraderie, and caring he provided throughout my PhD studies in Turkey.

I am very grateful to all the lab members and friends especially Omer, Sarmad, Abbas, Enes, Çağlar, Başar, Isa, Erdem and Muzaffer Abi. I am very thankful to Mohammad Akmal for the help and support in my PhD studies. Last but not the least, I am very thankful my house mates Hamza, Rehan, and Abbas for such an amazing time and memories.

Finally, I would like to thank Allah for blessing me with a wonderful life and amazing people around me.

I wish a healthy and wealthy life to all of you!

Haris Sheh Zad!

TABLE OF CONTENTS

LIST OF TABLES

LIST OF FIGURES

Chapter 1
INTRODUCTION

1.1 Magnetic Bearings

A magnetic bearing uses magnetic field to maintain the relative rotor and shaft position with respect to the stationary stator part. According the control action, there are two types of magnetic bearings: *passive magnetic bearings* and *active magnetic bearings*. The passive magnetic bearings generally make use of permanent magnets in order to passively stabilize the rotor. It does not require any control system but it has a disadvantage that it can only stabilize four degrees of freedom out of five. Therefore, in order to stably suspend the rotor, it has to be combined with active magnetic bearings. Active magnetic bearings make use of electromagnets in order to generate the levitation forces for stably suspending the rotor. The combination of active magnetic bearings and passive magnetic bearings is called *hybrid magnetic bearings.* Hybrid magnetic bearings make use of both the electromagnets and the permanent magnets in order to stably suspend the rotor in five degrees of freedom.

According to the forcing action, there are two types of magnetic bearings: *attractive type magnetic bearings* and *repulsive type magnetic bearings*. In attractive type magnetic bearings, the levitation forces are generated by the interaction between the opposite magnetic poles and in repulsive type magnetic bearings, the levitation forces are generated by the interaction between the similar magnetic poles. Figure 1.1 shows the different structural forms of radial and axial passive magnetic bearings including the concept of attracting type and repelling type. There are normally two ring permanent magnets used in the passive magnetic bearings. One ring is superimposed on the shaft and another ring is fixed on the stator. When the rotor magnet is not aligned with the stator permanent magnet, then an axial force is exerted on the rotor, the magnitude of which depends upon the axial distance between the centers of rotor permanent magnet and stator permanent magnet. Figure 1.2 shows the axial force vs the axial displacement of the shaft for the passive magnetic bearings. Therefore, in order to counter this axial force, active control is needed in the axial direction to bring the shaft back to the center position using electromagnets. The stiffness of the passive magnetic bearings depends upon the strength of the permanent magnets, radial distance between the two permanent magnet rings, axial length of the permanent magnet rings radial thickness of the permanent magnet rings.

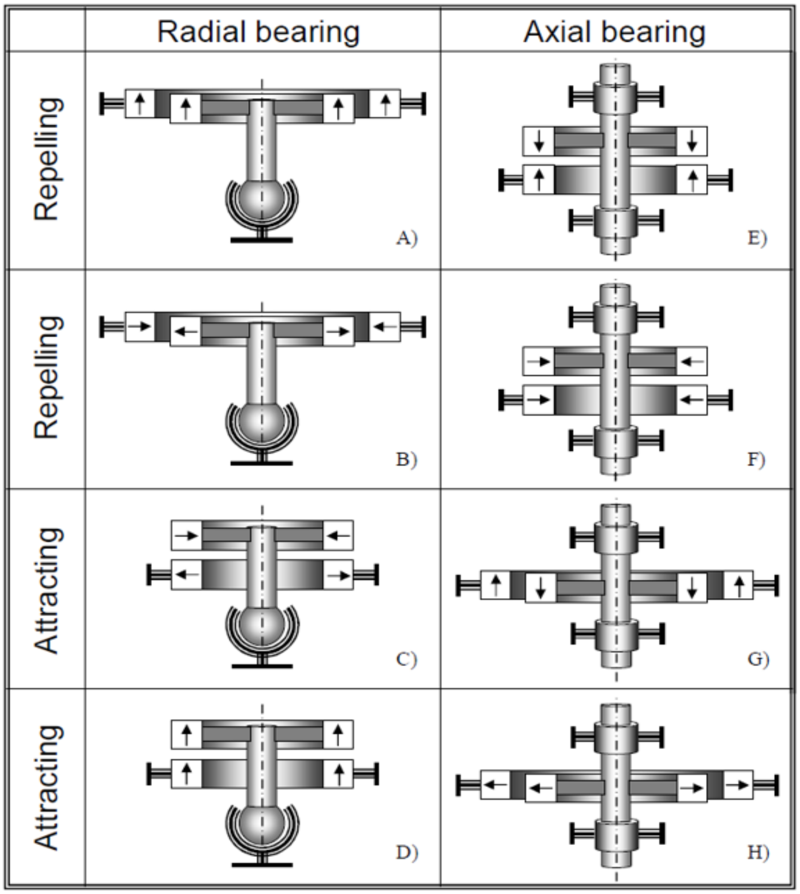

Figure 1.1: Passive magnetic bearings structural forms [1]

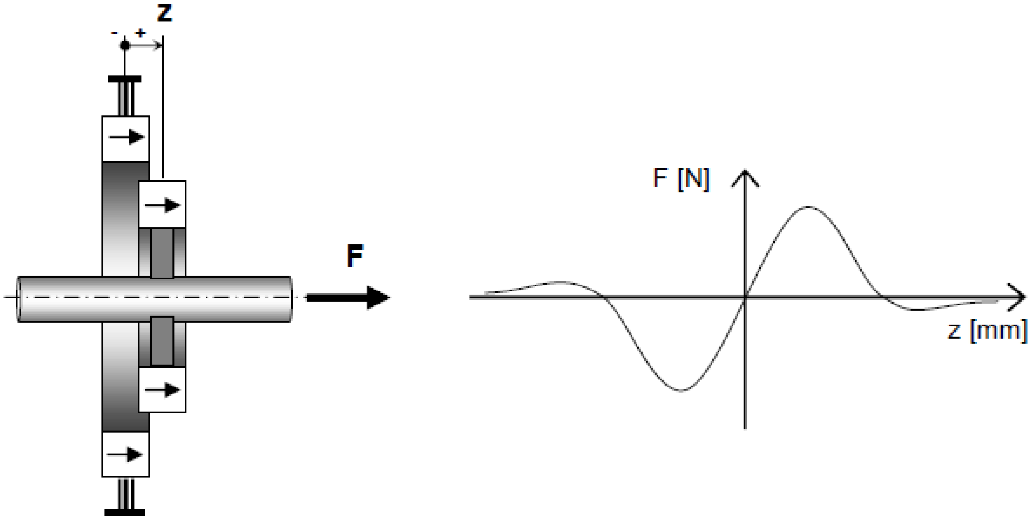

Figure 1.2: Passive magnetic bearing axial force vs axial displacement [1]

As the stiffness of the passive magnets increases, the axial force on the shaft also increases. Therefore, there should be a tradeoff between the stiffness and axial disturbance force exerted on the shaft.

According to the sensing action, magnetic bearings can be classified into *sensor-sensing magnetic bearings* and *self-sensing magnetic bearings*. In sensor-sensing magnetic bearings, the radial and axial direction displacements of the rotor are measured with sensors, like Hall Effect sensors, optical sensors, inductive sensors, and eddy current sensors etc. In self-sensing magnetic bearings, the rotor radial or axial direction position is estimated by using different techniques i.e. by designing an observer or by sensing the rotor position from the currents going into the coils of the electromagnets etc.

Active magnetic bearings use electromagnets and position sensors in order to control the shaft position. The currents in the electromagnets are adjusted based on the position feedback from the sensors and therefore closed loop control system is needed in order to stably levitate the rotor. Figure 1.3 shows the basic structure of the active magnetic bearings. The rotor radial position is measured with the gap sensor and is fed back to the microprocessor, where the required control signal is generated for the power amplifier in order to apply the desired currents to the electromagnets to bring the rotor to the desired position.

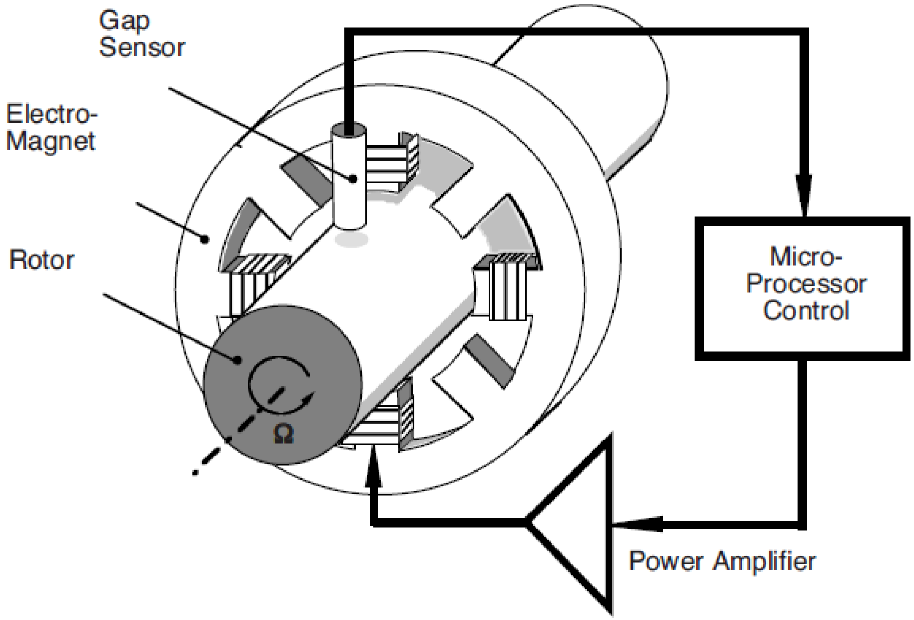

Figure 1.3: Basic working principle of active magnetic bearings [2]

The combination of the active magnetic bearings and the passive magnetic bearings is called *hybrid magnetic bearings*. Hybrid magnetic bearings have the advantages of lesser electrical power consumption, complexity of the controller and cost as compared to fully active magnetic bearings. Figure 1.4 shows an axial flow blood pump utilizing the hybrid magnetic bearing concept. Permanent magnets are used for the axial stability of the rotor while electromagnets are used for the radial stability of the rotor. A brushless DC motor is included for rotating the shaft around its axis. Figure 1.5 shows an axial flow blood pump having hybrid magnetic bearings. In this design, permanent magnets are used for the radial passive stability of the rotor, while electromagnets are used for actively controlling the shaft position in the axial direction. A motor is also included in the design for rotating the shaft around its axis. The axial length of the rotor increases with the inclusion of the radial and axial magnetic bearings to the design.

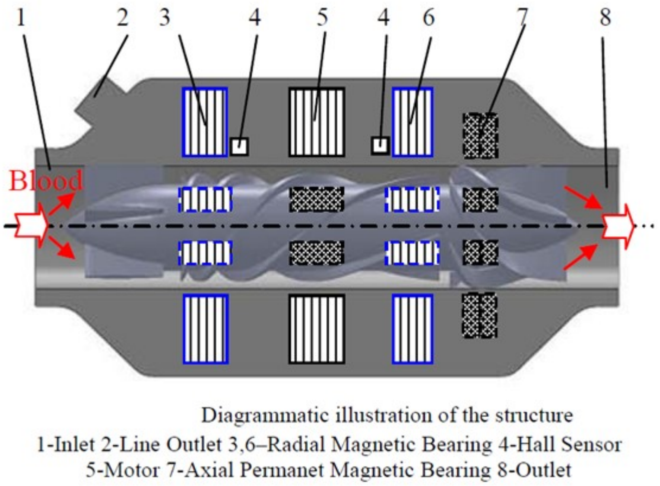

Figure 1.4: Axial flow blood pump with hybrid magnetic bearing [3]

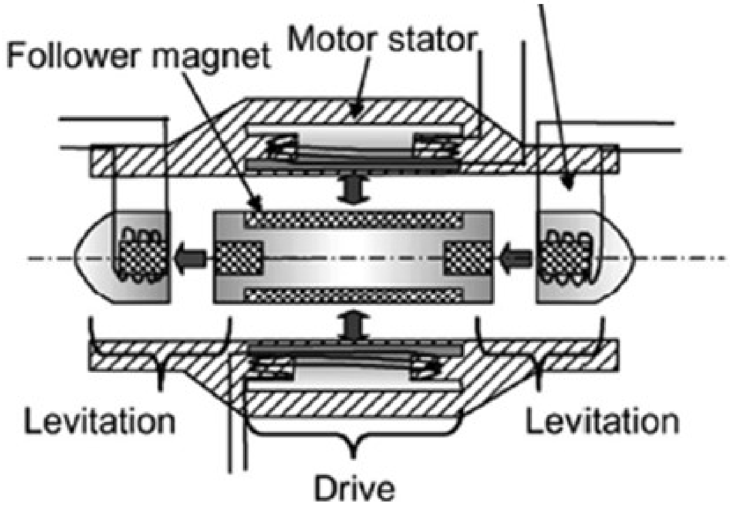

Figure 1.5: Axial flow blood pump using the concept of the hybrid magnetic bearings [4]

Magnetic bearings have the advantages of low friction, less heat generation, and non-contact operations as compared to the conventional mechanical bearings.

1.2 Stiffness and Damping of the Magnetic Bearings

The two main characteristics of both the magnetic bearings and mechanical bearings are the damping and the stiffness of the bearings. The stiffness of the bearing is analogous to the force displacement constant or spring constant as given in Hooke's law. However, the stiffness for the magnetic bearings may be negative unlike the Hooke's law. For an active magnetic bearing, when the shaft position is controlled by a constant current passing through the coils of the electromagnets, then for a negative stiffness, any disturbance acting on the rotor will cause the rotor to move it away from the equilibrium position as shown in Figure 1.6. Therefore, the rotor will keep on moving away from the equilibrium position resulting in an unstable system. Therefore, the active magnetic bearing system is an unstable system in open loop. The stiffness of the active magnetic bearing can be made positive by the application of the feedback control system. The rotor position is fed back to the controller, where a corresponding current is generated for the coils of the electromagnets in order to bring the rotor back to the equilibrium position.

The stiffness of the passive magnetic bearings utilizing the permanent magnets depends upon the geometric parameters of the permanent magnets and the type of the permanent magnets. The stiffness increases with the decrease of the radial air gap between the rotor permanent magnets and the stator permanent magnets. Also, the axial length of the permanent magnets is directly proportional to the stiffness of the passive magnetic bearings. However, with increase in stiffness of the passive magnetic bearings, the disturbance forces acting on the rotor due to the repelling on attracting forces between the permanent magnets also keep on increasing.

The damping coefficient of the magnetic bearings is the measure of the ability of the bearing to diminish the oscillations of the rotor and stabilize the system. The damping of the active magnetic bearings is controlled by injecting the control current into the windings of the electromagnets. For passive magnetic bearings, the damping is usually low and fixed for a specific design of permanent magnets as compared to the active magnetic bearings. Therefore, active magnetic bearings have widest range of applications as compared to the passive magnetic bearings.

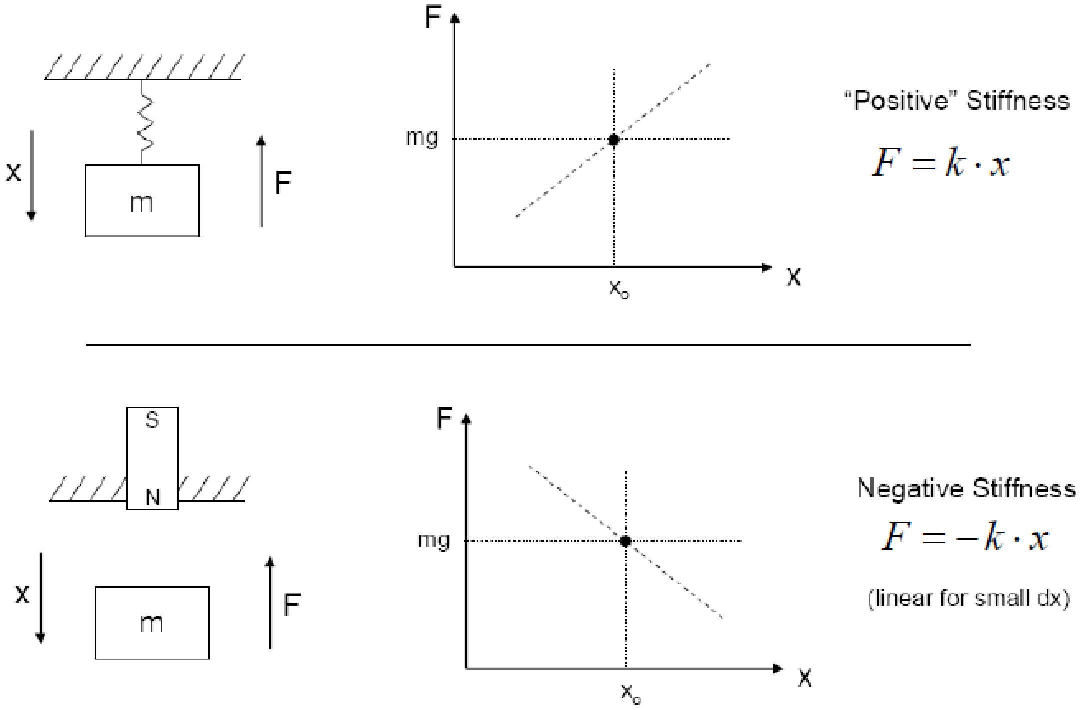

Figure 1.6: Concept of the positive stiffness and negative stiffness [5]

1.3 Control of Active Magnetic Bearings

The position control of the active magnetic bearings is a critical problem. Active magnetic bearings utilize the attractive forces between the rotor and the stator in order to stably levitate the rotor. Figure 1.7 shows the detailed diagram of the single degree of freedom active magnetic bearing system. The rotor is balanced between the two electromagnets actively by the currents i_1 and i_2. When the distance x increases in the positive direction, then based on the feedback of the position sensor, the current of the electromagnet 1 is decreased and he current of the electromagnet 2 is increased. Therefore, robust control is needed to keep the rotor at the equilibrium position in the presence of the external disturbances by controlling the currents going into the two electromagnets.

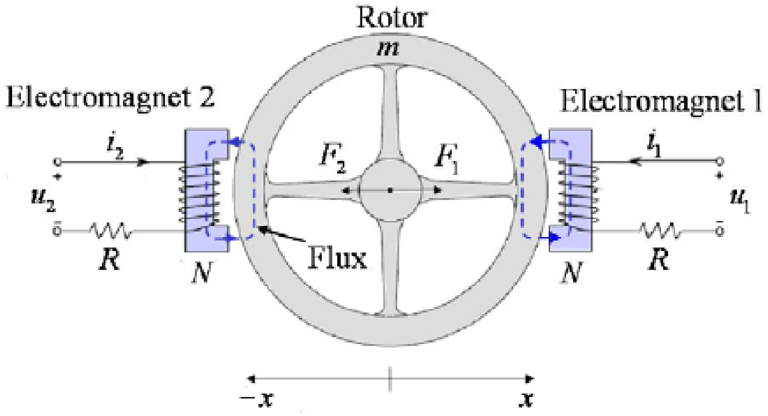

Figure 1.7: A single degree of freedom active magnetic bearing system [6]

1.4 Bearingless Motors

Magnetic bearings require one additional motor unit for rotating the shaft around its axis making the system stable in 6 degrees of freedom. This additional motor unit increases the length of the shaft. The functionality of both the motor unit and the magnetic bearings are combined in the bearingless motor system. One stator unit is used for both the levitation and rotation of the motor. There are two windings wound on each stator leg. One winding is used for the rotation of the shaft while another winding is used for stably levitating the rotor at the equilibrium position.

Figure 1.8 shows the schematic diagram of a bearingless motor unit. The stator consists of alternate coils for the rotation and levitation of the rotor. The rotor consists of permanent magnets with alternate polarity of north and south. Figure 1.9 shows the schematic diagram of a bearingless motor with two coils wound on each stator leg. One coil is used for the levitation of the rotor while another coil is used for generating the torque for the motor. The winding denoted by *drv* is used for rotating the rotor and the winding represented by *bng* is used for generating the bearing forces. The rotor consists of a permanent magnet which is diametrically magnetized.

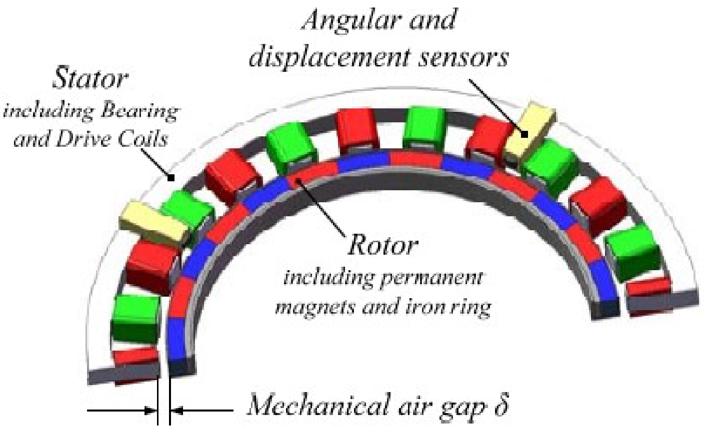

Figure 1.8: Schematic view of the bearingless motor with alternate coils for levitation and rotation [7]

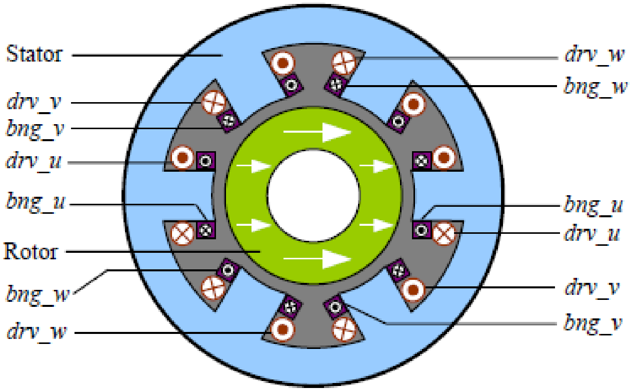

Figure 1.9: The arrangement of bearing and drive windings in a bearingless motor [8]

1.5 Application of Magnetic Bearings in Blood Pumps

Figure 1.10 shows the main components of a left ventricular assist device.

Figure 1.10: A left ventricular assist device and its drive components

Second generation blood pumps suffer from the problem of the red blood cell damage due to the stresses introduced by the mechanical bearings. Magnetic bearings are applied in the third-generation rotary blood pumps in order for the blood cells to move freely through the pump without being exposed to the shear stresses. The blood pump life is increased by the advantages of lesser heat generation, lower material wear, and minimization of the blood clotting. Application of hybrid magnetic bearings provide the advantage of simpler control structure and electronic complexity as compared to a fully actively levitated third generation blood pump. Figure 1.11 shows the cross section of an axial third generation rotary blood pump.

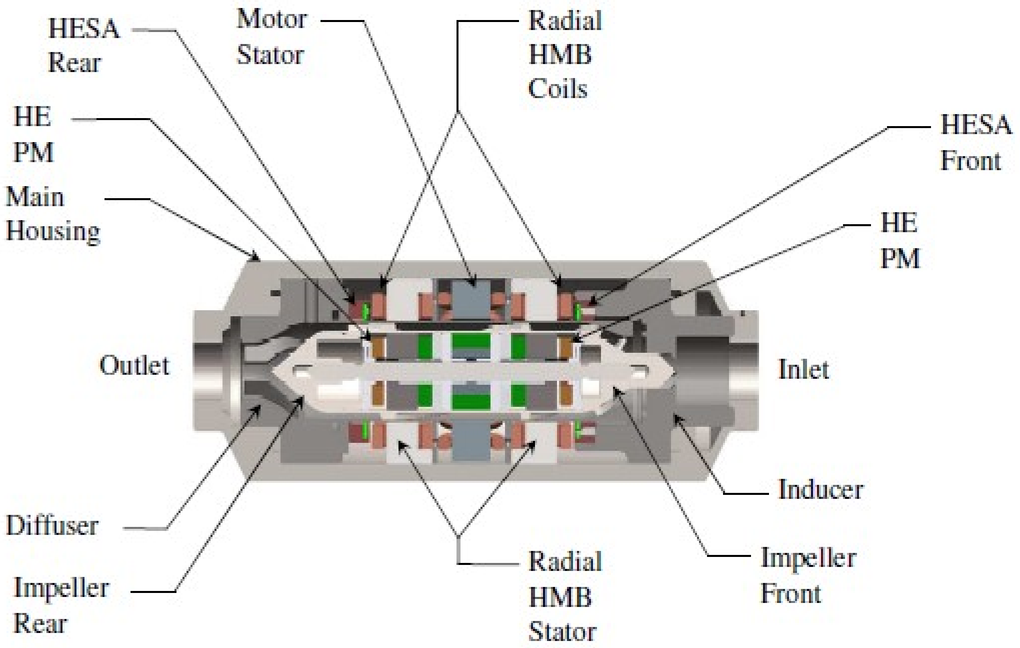

Figure 1.11: Schematic diagram of a third-generation axial flow blood pump [9]

The rotor is radially stabilized by electromagnets employing an active control. In axial direction, the rotor is stabilized using permanent magnets using the concept of passive magnetic bearings. Bearingless motor concept is used in centrifugal blood pumps in order to rotate and stably suspend the rotor in all six degrees of freedom using only stator unit. The rotor is passively stabilized in the axial and tilt direction by the reluctance forces present between the stator iron and the permanent magnets embedded into the rotor. The currents in the stator windings are adjusted in such a way so as to stably levitate the rotor. There are either two separate coils wound on each stator leg, in which one coil is used for the levitation and another coil is used for the rotation of the rotor. Also, there are bearingless motor pumps, in which only one coil is wound on each stator leg and the currents in each of these coils is adjusted in such a way that the rotor is rotated as well as levitated at the same time.

1.6 Research Objectives

The third-generation axial flow pumps utilizing the magnetic bearings suffer from the problem of longer rotor size in the axial direction. The rotor of the axial flow pump resembles a column, therefore only one magnetic bearing cannot stabilize the rotor in the tilt direction and radial direction. At least two radial magnetic bearings are needed for the axial flow pump to fully stabilize the impeller of the pump with additional motor unit as well in order to rotate the impeller. Also, at least two bearingless motor units are required for the operation of the third-generation axial flow pump.

The aim of this research is to design a third-generation axial flow pump using only one bearingless motor unit for the rotation as well the levitation of the impeller. The computational fluid dynamics (CFD) analysis is performed in order to optimize the design of the impeller and overall pump system. An enclosed impeller based rotor system is proposed based on the optimization in which rotor axial length is much smaller as compared to the diameter of the rotor. Therefore, only one bearingless motor system is required for the complete operation of the pump.

Generally, eddy current sensors are used for measuring the rotor radial position in the bearingless brushless DC motors and bearingless permanent magnet synchronous motor systems and Hall Effect sensors are used for measuring the rotor angular position. The eddy current sensor's application in the proposed optimized design of the third-generation blood pump is not possible due to the much smaller diameter of the pump. Therefore, a sensor system must be developed in order to measure the radial position of the rotor in the proposed design.

In this research, a novel design for the rotor assembly of the proposed blood pump is proposed in which the rotor radial position is measured with the linear Hall Effect sensors in addition to the rotor angular position. The working principle of the sensor assembly is explained in detail and the rotor control system is explained based on the Hall Effect radial position sensors.

Magnetic circuit method is generally employed for the design of the magnetic bearings and calculating the different parameters of the bearings, such as stiffness, damping, forces, currents etc. But in this method, the effects of eddy currents, fringing flux, leakage flux and hysteresis effect is ignored. Therefore, due to lot of assumptions and simplifications, the magnetic circuit method does not give an accurate distribution of the magnetic flux densities in the air gaps and on the rotor and stator surfaces. The equivalent damping and stiffness of the magnetic bearings have low precision if obtained through the magnetic circuit method.

The control of the magnetic bearing system is a critical problem in the presence of the disturbances, unmodeled dynamics and nonlinearities. The classical control techniques such as PID control cannot give robustness against theses disturbances. Therefore, a magnetic bearing prototype system is first designed and manufactured and an advanced adaptive sliding mode controller is designed for the magnetic bearing prototype system and experimentally applied to the prototype system. The radial direction stability is obtained through passive magnetic bearings, while in the axial direction, the prototype system is balanced with active magnetic bearings using electromagnets. The designed controller is applied to the novel design of the bearingless motor in which the radial direction displacement of the rotor is measured with Hall Effect sensors. There are two permanent magnet rings in the rotor assembly, one ring is used for measuring the rotor radial direction and one ring is used for generating the torque of the bearingless motor and the radial suspension forces for the motor system. Therefore, strong magnetic coupling exists in the rotor system and accurate radial position is required for the advanced controller implementation. Therefore, the radial position of the rotor is first adaptively estimated and then a sliding mode controller is designed for the bearingless motor system. The results show better position tracking of the bearingless motor as compared to the classical control techniques.

Finite element method is a field method which is more accurate as compared to the magnetic circuit method. The models obtained through the finite element method are more identical to the physical systems. In this research, finite element method based analysis of the magnetic bearing prototype system is performed. Based on finite element analysis, the forces, stiffness, damping, currents, magnetic flux densities and flux linkages of the magnetic bearing prototype system are obtained which are compared to the experimental data. Based on the finite element analysis, the controller is designed for the magnetic bearing prototype system.

Finite element analysis of the novel design of bearingless motor for the miniature axial flow blood pump is also performed. The passive and active stiffness, damping, magnetic flux distribution, forces and currents are obtained through the finite element analysis and compared with the experimental data. The results obtained through finite element analysis show a good agreement with the experimental data.

Chapter 2

LITERATURE REVIEW

2.1 Overview

In this thesis, a magnetic bearing prototype system is designed and an advanced adaptive controller is designed for the active position control of the prototype system. A novel bearingless motor based design of the axial flow impeller is proposed and manufactured. The advance controller is applied to the bearingless motor system for the position control. Finite element analysis of the overall magnetic bearing prototype system is performed and experimentally verified. In this chapter, the detailed literature review about magnetic bearings, control of magnetic bearings, bearingless motors and their control, and application of magnetic bearings and bearingless motors in the rotary blood pumps is provided.

2.2 Magnetic Bearings

The basic principle of magnetic bearings is to provide contact free operation of the rotor system. Figure 2.1 shows the basic principle of the single axis magnetic bearing system. The rotor position is measured with the gap sensor and then the controller generates the command signal to the power amplifier circuit. The Power amplifier then drives the electromagnet which keeps the rotor stable at the equilibrium position.

A real rotor needs more than one magnets for its suspension and motor unit for its rotation. Figure 2.2 shows the classical demonstration model of a magnetic bearing prototype system [10]. The rotor length is 0.8 m and have 12 kg of weight. A CCD-array is used to measure the rotor displacement, which is fed to the microcontroller, where digital command signals are generated for the electromagnets. The rotor airgap of this demonstration setup is 10 mm.

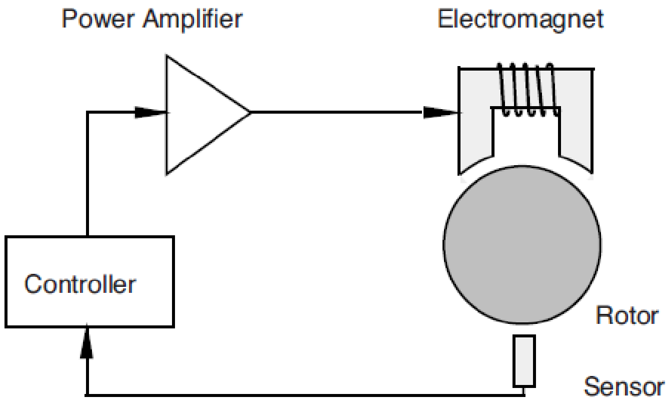

Figure 2.1: Active electromagnetic suspension principle [2]

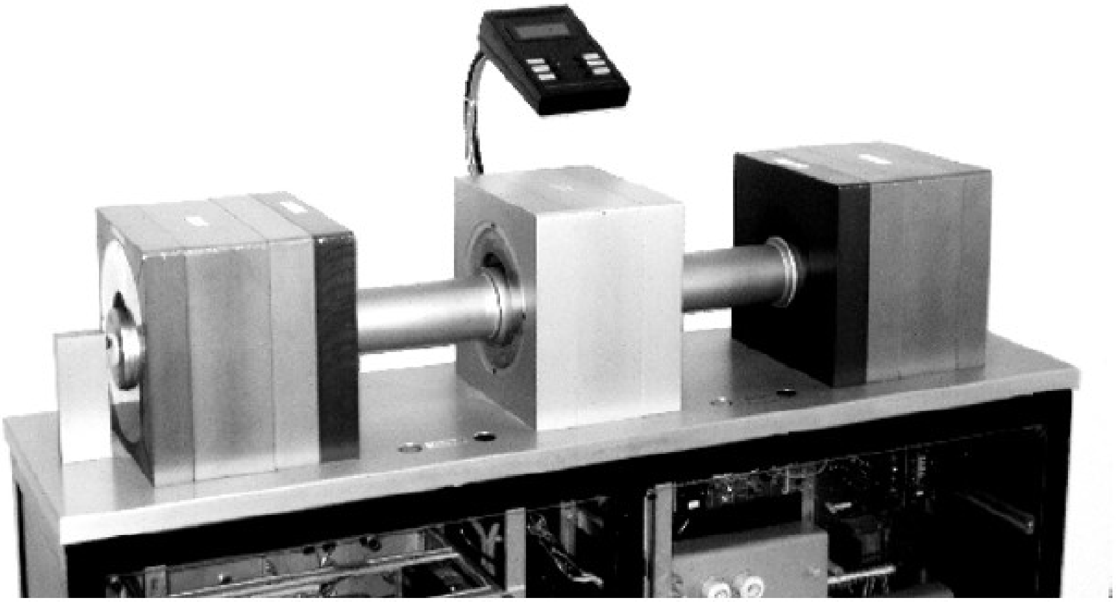

Figure 2.2: Zurich Exhibition Phenomena (1984), A magnetically suspended rotor with the magnetic bearings on the left and right, motor in the middle of the setup [10]

In 1842, Earnshaw presented that it is not possible to levitate the rotor stably in all 5 degrees of freedom with only permanent magnets and gravitational force [11]. In 1939, Braunbek gave further insights in to the physics of the magnetic bearings, when there was already a great interest was developing in the applications of the magnetic bearings [12]. The *Levitron*, which is a gyro top, shows that under certain conditions, a body can spin freely in a permanent magnet array. The gyroscopic effect present in the Levitron prevents it from flipping. [13, 14] gave the theoretical derivations for this phenomenon. [15, 16] gave further detailed explanations in terms of the dynamics of the classical rotor. The optimization of the magnetic field and the magnetic flux distribution is calculated in [17]. Diamagnetic fields can be used to stably suspend the rotor in a magnetic field. Diamagnetic materials respond with mild repulsion to the magnetic fields. Diamagnetic materials flout the Earnshaw's theorem because of having negative susceptibility [18]. Therefore, by using the materials feeble diamagnetism, the stable suspension of the magnet can be achieved.

For a hovering suspension, Kemper applied for the patent in 1937 as new way of transportation [19]. He performed an experiment, in which a load consisting of 210 kg was transported on airgap of 15 mm [20]. The pole face area of the electromagnet was 30 by 15 cm having magnetic flux density of 0.25 T and power consumption of 250 W. The capacitive or inductive sensors and valve amplifiers were used for the control of the prototype setup. For the vehicles based on the magnetic levitation, this prototype setup was a predecessor. The MAGLEV, which is a vehicle based on the magnetic levitation, works on the suspension forces produced by the magnets installed in the iron track as shown in Figure 2.3 [2].

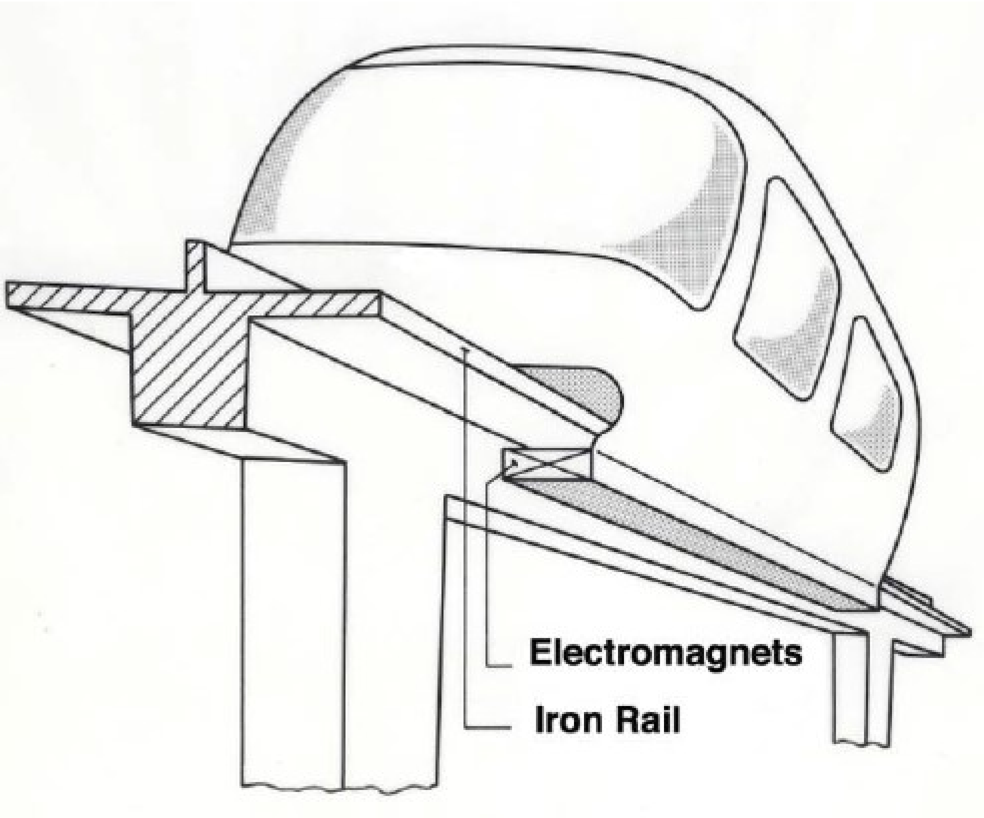

Figure 2.3: Schematic diagram of the MAGLEV vehicle [2]

The control diagram of the MAGLEV is shown in Figure 2.4 [21]. Separated control is implemented for each electromagnet. The electromagnet voltage is the control input. The current for each electromagnet, the acceleration for each magnet and the airgap are measured in order to generate the control signal.

[22] used magnetic bearings control signals in order to derive the angular rate of a magnetically levitated rate gyro. [23] worked on the satellites attitude control based on the magnetically levitated moment wheel.

In the past decades, the use of magnetic bearing technology in the rotors used for technical purposes has been greatly developed. The basic reason for this the availability of the power electronics and the advancements in the signal processing techniques. Also, the theoretical developments in the modeling of the rotor dynamics has been played a good role in the magnetic bearings applications. By 1975, the theoretical and experimental investigations of the self-excited vibration's active damping control for the centrifuges were carried out [24]. Magnetic bearings were introduced to the industrial applications by [25]. A website of the University of Vienna consists of the industrial and research activities related to the active magnetic bearings [26].

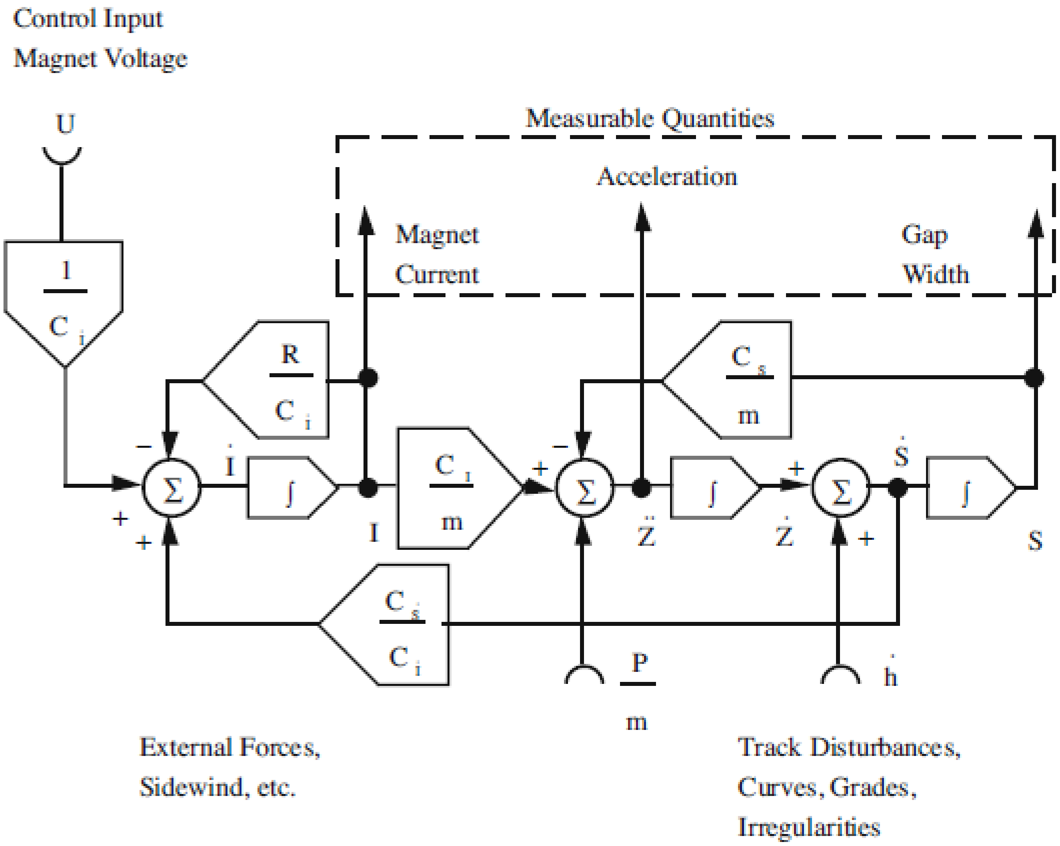

Figure 2.4: Controller structure for MAGLEV single magnetic wheel [21]

Figure 2.5 shows the different types of magnetic bearings based on the magnetic hovering and magnetic forces in addition to the active magnetic bearings based on the electromagnets [27].

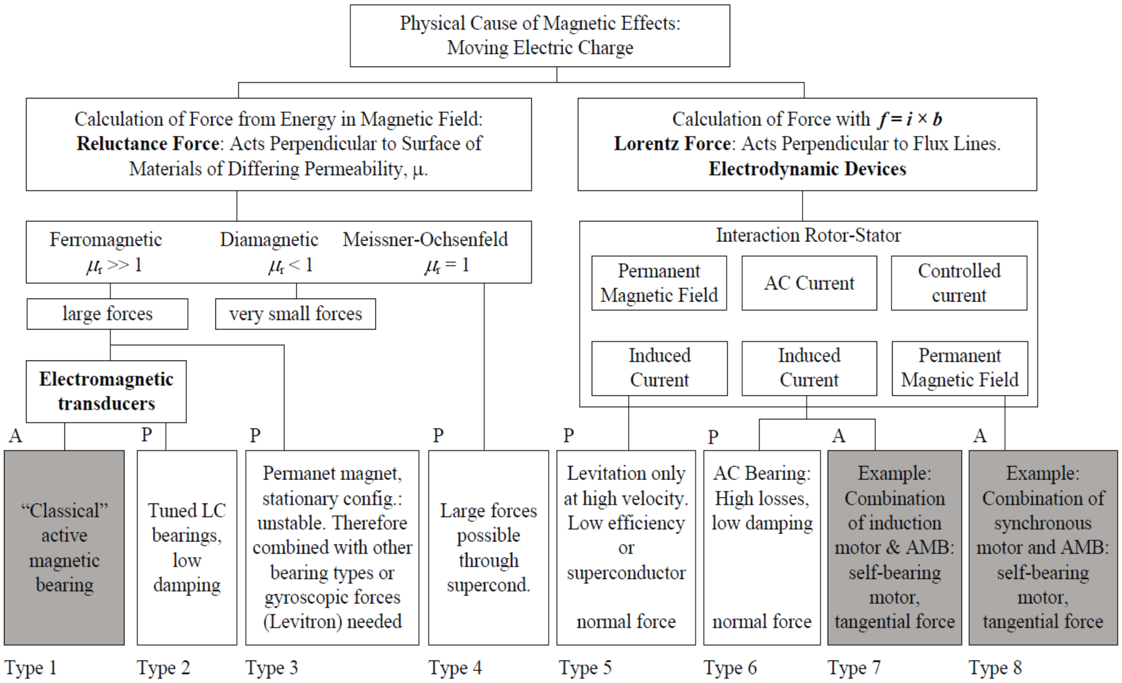

Figure 2.5: Classification of magnetic bearings [27]. A means active magnetic bearings and P means Passive magnetic bearings.

2.3 Control of Active Magnetic Bearings

The control of active magnetic bearings is a critical problem as the active magnetic bearing system is an unstable system in open loop. Therefore, based on the position feedback from the rotor, the electromagnets currents should be regulated accordingly using active control. The controllers design for the active magnetic bearings control started in the 1940's with their inception. The decentralized PID controller design was the main control technique for the active position control of more than 90 percent active magnetic bearings setups until last ten years. In the decentralized control, the active magnetic bearing system is being decoupled into loops of single-input and single-output (SISO) systems. As an example, a two degrees of freedom active magnetic bearing system can be decoupled into two SISO system loops and each loop current is obtained by the rotor displacement within the corresponding axis only. However, using PID controllers for the active control of the magnetic bearings suffer from the problem that velocity signal of the rotor is required for feedback which is not possible in small magnetic bearings prototypes. Also, PID controllers require the linearized model of the magnetic bearings and the gains of the PID controller are fixed. The PID controller is not robust against the parameter variations of the system, non-linearities and unmodeled dynamics of the system.

A variation of the classical PID controller is proposed by [28] in the form cased PI/PD controller for the position control of the active magnetic bearing system. The PI/PD controller has the advantages of simple realization, higher closed loop stiffness and damping and transparent design as compared to the classical PID controller.

The optimal H_∞ controller design for the control of active magnetic bearings started soon after the H_∞ controller theory in 1981 by George Zames [29, 30]. A most important parameter for the magnetic bearings design is the stiffness of the bearing system. The stiffness of the magnetic bearing should not become less than a certain threshold value after the application of the loads or unknown disturbances for a specified range of frequencies. The new theory to the H_∞ optimal controller design was done by Herzog and Bleuler [30] in order to determine the effectiveness of the controller in the presence of worst case interferences in the specified range of frequencies. The optimal H_∞ controller was designed and experimentally tested for the position control of the active magnetic bearings system prototype by [31] in the presence of external disturbances.

Vischer introduced the concept of self-sensing active magnetic bearing systems in 1988 [32]. Later Vischer and Bleuler did research on estimating the rotor position from the currents flowing through the coils of the electromagnets in the magnetic bearing system [33-35]. The main advantage of this method is the reduced cost, lesser complexity of the hardware and improved reliability. But the self-sensing technique for the active magnetic bearings is very difficult in practice and therefore as of 2005 there were no applications present in the industry based on the concept of self-sensing [35].

Kucera in 1997 stated after analyzing the effects of the variations in parameters of the controllers on the self-sensing active magnetic bearing system sensitivity that stability of the rotor in the entire airgap can be obtained at the cost of the robustness of the system [36]. Noh and Maslen in the same year 1997 developed a technique for measuring the airgap length using the current ripples present in the windings of the electromagnets. This ripple can be demodulated in order to get the airgap length information and also rejecting the effect of the control voltage at the same time [37]. Another technique was presented by Schammass in 2005 [35]. In this technique, the rotor position is extracted by the measure of the inductance change of the coils of the actuator after the injection of a high frequency signal to the coils. After the demodulation of the current waveform and by utilizing the current's first harmonic component, the position signal is extracted for the rotor system.

Gao [38] and Han [39] developed a new controller which is called Active Disturbance Rejection Control (ADRC) and was simulated for the position control of self-sensing active magnetic bearing system by Su-Alexander in 2006 [40]. The controller proved to be very robust against the disturbance rejection and plant parameter variations. This controller is easier in tuning as compared to the classical PID controller because of having only two parameters to be tuned.

Smith and Thibeault in 2002 stated that the self-sensing control of the active magnetic bearings systems is impractical because the closed loop has a limited robustness [41]. This idea of [41] was later rejected by Maslen et al. [42] in 2003, in which they showed that a significant robustness of the self-sensing active magnetic bearing system can be achieved by the modeling the magnetic bearing system as linear periodic system in contrast to the linear time-invariant system which was modeled by Smith et al. in 2002. This idea of linear periodic system was further analyzed more precisely in order to achieve a good robustness of the system by [43].

Extended Kalman filter was used for estimating the state vector of the active magnetic bearings system axis by [44-46]. A linear quadratic Gaussian controller was proposed for the control of the active magnetic bearings system by [47]. Feedback linearization technique was used by [48] in order to design an extended state observer.

However, all of these control techniques discussed above required an accurate mathematical model for the position control of the active magnetic bearings system which is very difficult to obtain in the presence of the parameter variations, load disturbances and nonlinearities.

Sliding mode control is a nonlinear control technique, in which multiple controller structures are utilized in order to make sure that the trajectories of the system will always move towards the switching condition. The uncertainties, the parameter variations, and the external disturbances does not affect the sliding mode controller performance make it a good robust controller [49-52]. The uncertainties present in the system dynamics can be approximated by the adaptive control techniques. [53] proposed an adaptive sliding mode controller for the dynamic systems using radial basis functions (RBF). [54] proposed a double loop recurrent neural network based sliding mode controller. [55] developed an adaptive sliding mode controller using the fuzzy neural network combined structure in order to eliminate the chattering present in the sliding mode controller without losing the precision and robustness of the system. Time delay estimation was used by [56, 57] in order to design the adaptive sliding mode controller for the robot manipulators. [58, 59] designed a robust sliding mode controller for the position control of the active magnetic bearing system with flexible rotor system. A robust and nonsingular terminal sliding mode controller was proposed for the position control of the active magnetic bearing system by [60]. [61] proposed a sliding mode controller for the active magnetic bearing system control based on the observer design. [61] proposed an adaptive sliding mode controller for the position control of the active magnetic bearing system based on the neural network.

However, in the literature, the adaptive controller design for the magnetic bearing system with unknown system dynamics as well as the with the unknown system input function is not present. In this thesis, an adaptive sliding mode controller is designed for the magnetic bearing prototype system based on the RBF network system. The stability of the controller is done by using the Lyapunov stability criterion. The system dynamics and the input function of the system are estimated by using adaptive RBF network and then a robust sliding mode controller is designed for the active position control of the active magnetic bearing system. An experimental prototype setup is built for the active magnetic bearing system and the designed adaptive controller is tested and verified experimentally in the presence of the external disturbances, unmodeled dynamics and the parameter variations. The performance of the designed adaptive sliding mode controller is compared with the classical PID controller for the position tracking of active magnetic bearing prototype setup. The adaptive controller shows good robustness and disturbance rejection abilities as compared to the PID controller.

2.4 Bearingless Motors

The first bearingless motors were the induction motors. [62] proposed the axial bearingless motor firstly. It consisted of an bearingless induction motor with axial gap. [63] presented the first radial bearingless motor. Unbalanced line currents were used for controlling the radial position using an induction machine. Current regulators with very accurate high power were required for this bearingless motor and also there were difficulties in controlling the position of the rotor when it was located in the center of the stator. [64] provided more details on this bearingless induction motor.

The next step of the bearingless motors were the bearingless synchronous reluctance motors as stated in [65, 66]. These bearingless synchronous reluctance motors consisted of four pole standard machines with additionally having two pole windings. The motoring torque was provided by the conventional three phase stator winding and four pole motor system. The currents in the suspension windings of these motors are synchronous with the mechanical speed of the motor in order to generate the forces in the x and y direction. Constant forces are generated in the x and y direction by the use of this modulation technique. The magnitude of the x and y direction forces depend upon the x and y direction coil currents as well as upon the d-axis current.

As a next step, the technique of the bearingless synchronous reluctance motors was applied to the bearingless induction motors [67]. [67] presented a standard induction motor with four poles and additionally two pole windings with two phases were wound on the stator in order to provide the suspension force action for levitating the rotor. The motor speed was synchronous with the x and y direction currents in the windings in order for the suspension force flux to be aligned with the flux of the rotor.

[68, 69] proposed the bearingless permanent magnet motors. [69] presented a bearingless motor based on the principle of the Lorentz forces and consisted of additional windings for the levitation wound on the stator. The Lorentz forces are produced when current passes through the magnetic field and therefore, the stator in this motor does not have any teeth. Because the stator consisting of teeth does not produce higher values of Lorentz forces. The reason for this is that all the magnetic flux density is confined on the teeth of the stator rather than in the slots of the stator. [68] developed a bearingless permanent magnet motor similar to the principles presented in the bearingless synchronous reluctance motors and bearingless induction motors. Two poles and two phase windings were used for generating the bearing action and a four pole rotor was used.

The last main type of bearingless motors were the bearingless switched reluctance motors. [70] levitated the first switched reluctance motors by using individual stator coils. The windings which are connected in series in the general switched reluctance motors were not applied in these bearingless switched reluctance motors. A net force was generated by using this technique using a differential flux on various sides of rotor. After that, the bearingless switched reluctance motors were designed by using the standard winding techniques of the switched reluctance motors. Additional windings were installed on the stator for controlling the radial direction suspension force. This configuration had the advantage of having zero back EMF at all speeds in the control windings. This design of the bearingless switched reluctance motors were studied by [71-73].

The bearingless permanent magnet motors are studied in greater detail in the literature. The design described in [68] was explored in much detail in the [74] and [75]. These articles focused on the effect of varying the magnet thickness on the radial force of the bearingless motor. [76] worked on the research of the demagnetization of the thin permanent magnets in these motors. Lorentz type bearingless permanent magnet motors are not studied in detail until now. The main reason is that there is not any trade off present between the radial suspension force and the motoring torque as presented in [77, 78]. [79, 80] researched on the different configurations of the torque and the radial force mechanisms for the bearingless permanent magnet motors. [81] and [82] developed a control technique which was applicable to both the bearingless induction motors and bearingless permanent magnet motors. [83-85] researched on the performance and control of the inset type permanent magnet motors. [86] worked on the internal permanent magnet type motors and stated that the such motors have radial force much closer to the induction motors which have the radial force higher than any other type of the machine. Surface mounted bearingless permanent magnet motors provide greater torque while the internal permanent magnet bearingless motors provide higher values of radial suspension forces. [87, 88] proposed a design consisted of a hybrid typed rotor having the properties of both the interior motors and surface mounted motors. [89] presented a toothless bearingless permanent magnet motor, not using the Lorentz forces. This motor had the advantage of generating lesser torque ripples but due to absence of teeth, it generated smaller values of the suspension forces. [90] proposed an axial gap bearingless permanent magnet motor having higher value of power density as compared to the radial type. [91] presented a novel exterior topology of the rotor for the bearingless brushless synchronous motors. The proposed motor has a power rating of 200 W. This motor has the applications in the low-shear and high-purity fields. [92] presented a control method for bearingless brushless DC motors based on the mathematical model of the radial suspension force.

[93] proposed a nonlinear feedback controller structure for the bearingless brushless DC motors. The tilting and the axial direction stabilization in this motor is achieved using the passive reluctance forces present between the permanent magnets of the rotor and the stator iron. [94] proposed a control topology for the bearingless permanent magnet synchronous motors based on the mathematical model derived by the inductance matrix technique. [95] proposed a new design of the permanent magnet flux-switching bearingless motor having the properties of good decoupling between the force and torque and also good controllability of the radial suspension forces. The teeth configuration of the stator for the permanent magnet synchronous motor are studied in detail in [96]. [97-99] proposed a novel control topology for the time-divided suspension force and torque control of the bearingless permanent magnet motor. The surge voltages are suppressed in the switching devices in the proposed design.

[100] proposed a new winding arrangement in order to increase the radial suspension forces in the bearingless brushless DC motors. [101] compared the performance of the two phase, three phase and four phase bearingless slice motors based on the electronic power, cost and power losses. [91, 102-106] researched on the performance of the high speed bearingless drives and bearingless torque drives.

However, in the literature, all bearingless permanent magnet motors use eddy current sensors for the detection of the radial airgap of the rotor. In this thesis, a novel design of the bearingless permanent magnet motor is presented in which the radial position of the rotor is measured using linear Hall Effect sensors. A novel mechanical design of the motor is proposed and the finite element analysis of the proposed design is performed. The motor stiffness, damping, radial forces, axial forces, electrical currents and torque of the motor are evaluated at different operating conditions. The experimental prototype setup is manufacture and the performance of the proposed bearingless permanent magnet motor is experimentally verified with novel radial position sensing.

2.5 Third-Generation Rotary Blood Pumps

The flow rate requirement for the adult pumps is 5 l/min and pressure of 100 mmHg, while for the pediatric pump, 0.9-2.0 l/min and pressure of 65-75 mmHg. The second-generation rotary blood pumps suffer from the problem of the red blood cell damage due to the friction present between the rotor and the mechanical bearings and also blood clotting. Third-generation blood pumps use magnetic bearings instead of mechanical bearings. Therefore, the red blood cells are not damaged because there is no friction present in the magnetic bearings. There is also less heat generation in third-generation blood pumps and also the blood clotting is minimized. Much research is being done on the third-generation blood pumps regarding their mechanical structure and control.

[9] developed a hybrid magnetic bearing setup for the axial flow blood pump. Permanent magnets are used in this design for generating the biased flux. Hall Effect sensors are used measuring the rotor radial direction displacement. Axial direction stability of the rotor is obtained using permanent magnets passively. A brushless permanent magnet DC motor is installed in the middle of the pump in order to drive the rotor at the operating speed. The finite element analysis of this axial flow pump is provided in the [107] in detail. [108] provide the blood test results of this axial flow blood pump.

[109] developed a centrifugal blood pump comprising of magnetic bearings. A bearingless motor concept is used in this design. The developed pump consists of a thin rotor

having a semi open and type-6 vane impeller. The rotor outer surface consists of four pole permanents installed on the circumference of the rotor. Because of having the thin rotor structure, the tilt and the axial direction stability of the rotor are obtained passively. The radial airgap was 1 mm. The maximum flow rate, head and rotational speed were 11 L/min, 270 mm Hg and 2800 rpm respectively. [110] developed a brushless DC motor which is magnetically levitated for the left ventricular device. The designed motor has twelve stator poles and a permanent magnet on the rotor consisting of eight poles. [111] developed a magnetic bearing system for the third-generation blood pump based on the parameters of hemodynamic stability, mechanical stability, efficiency, occupying volume, and stiffness of the rotor system. The designed pump has one degree of freedom active control in the axial direction while in the radial direction the rotor is stabilized passively using permanent magnets. Eddy current gap sensor having outer diameter of 2.38 mm are used for measuring the rotor radial direction displacement. The rotational speed is 5000 rpm. The outer diameter is 22 mm and the length is 97 mm.

[112] provided a review of different third-generation blood pumps with magnetic bearings. The article has provided details about the third-generation blood pumps having (i) motor system externally driven (ii) motor systems with direct drive technique and (iii) the bearingless motor system configuration. [113] provided the details on the design and the performance analysis of the hybrid magnetic bearings in a centrifugal rotary blood pump. [114] proposed a design for the miniature third-generation axial flow blood pump utilizing the passive magnetic bearings. [115] developed an axial magnetic bearing system for the BiVACOR rotary BiVAD and total artificial heart. [116] proposed a design of the magnetically levitated centrifugal blood pump having an axially suspended motor system. [117] presented a novel design of the levitated blood pump having hybrid magnetic bearings. [118] proposed a new design of the compact centrifugal rotary blood pump having a rotor that was magnetically levitated. [119] developed a compact design of the centrifugal rotary

blood pump using a magnetically levitated rotor. The designed blood pump had a low hemolysis value and high efficiency.

However, these third-generation blood pumps have axial length which resembles a column, which require at least two bearingless motors in the radial direction. In this thesis, a novel design of an enclosed impeller system is proposed, which has an optimized shorter axial length. Therefore, only one bearingless motor is needed for driving the rotor. A four-pole permanent magnet is installed on the rotor in order to provide the motoring torque and also the radial suspension forces. Another permanent magnet is installed on the rotor as well in order to measure the radial displacement of the rotor. In the axial and the tilt direction the rotor is passively stabilized using the reluctance forces between the permanent magnet of the rotor and the stator iron. Two separate coils are wound on each stator leg. One winding is used for generating the torque for the motor and one winding is used for generating the radial levitating forces. The decoupling between the two windings is obtained and the rotor is stabilized in all six degrees of freedom with the proposed bearingless motor.

Chapter 3

DESIGN OF HYBRID MAGNETIC BEARING PROTOTYPE

3.1 Introduction

In this chapter, a hybrid magnetic bearing prototype system is designed and analyzed. The hybrid magnetic bearing system consists of permanent magnets and electromagnets. The radial stability is achieved using the passive magnets and axial stability is achieved by using the electromagnets. The electromagnets are actively controlled using the currents of windings in order to keep the rotor at the equilibrium position. A brushless DC motor is designed for the hybrid magnetic bearing system to rotate the shaft around its axial axis.

3.2 Design

The three-dimensional (3D) model of the hybrid magnetic bearing prototype system is shown in Figure 3.1.

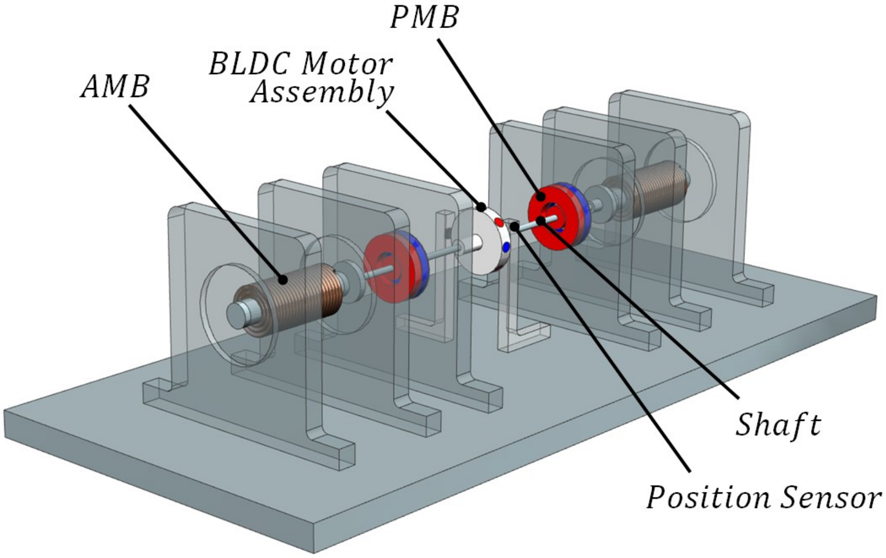

Figure 3.1: 3D model of the hybrid magnetic bearing prototype system

The prototype system consists of two electromagnets for controlling the axial displacement of the rotor. The shaft consists of two permanent magnet rings. Two permanent magnet rings are attached with the stator. These permanent magnet rings are used as the passive magnetic bearings for the prototype system. The permanent magnets rings of the shaft and the permanent magnet rings of the stator are axially magnetized and they are placed in such a way that they are in a configuration of repelling passive magnetic bearings. The two corresponding ring magnets on the rotor and the stator repel each other when they are placed as shown in Figure 3.1. Therefore, a strong axial force acts on the rotor when the rotor permanent magnet and the stator permanent magnet centers are not aligned. A brushless DC motor is placed in the middle of the bearing system. This brushless DC motor works on the principle of the single-phase DC motor. The schematic diagram of the hybrid magnetic bearing prototype system along with the dimensions of different parts is shown in Figure 3.2.

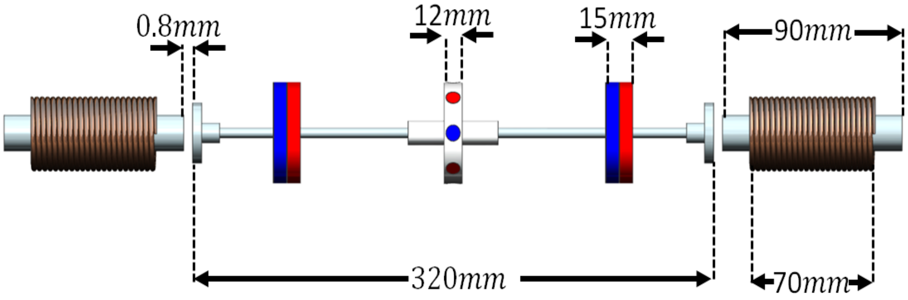

Figure 3.2: Schematic diagram of the hybrid magnetic bearing prototype system showing dimensions of different parts of the prototype

An axial position sensor measures the position of the shaft and sends the corresponding voltage signal based on the sensitivity of the sensor to the microprocessor. The control algorithm is then applied based on the position of the shaft and corresponding currents are applied to the two electromagnets in order to stabilize the shaft at the equilibrium position. The neodymium iron boron (NdFeB) N48 grade permanent magnets are used for the passive magnetic bearing permanent magnet rings. These magnets have higher values of the magnetic flux densities as compared to other permanent magnets e.g. ferrite magnets.

3.3 Parametric Analysis of the Design Variables

The design of the hybrid magnetic bearing prototype system is optimized using finite element analysis. The overall prototype of the magnetic bearings is simulated for the stiffness, magnetic forces, damping, electrical currents, number of turns, diameters of the permanent magnets rings other design parameters. Based on this analysis, optimized values of the mechanical design and electrical parameters are selected for the hybrid magnetic prototype system are selected. The detailed analysis of the passive magnetic bearings and active magnetic bearings is provided as following.

3.3.1 Passive Magnetic Bearings

The schematic diagram of the passive magnetic bearing used in the prototype system is shown as below in Figure 3.3.

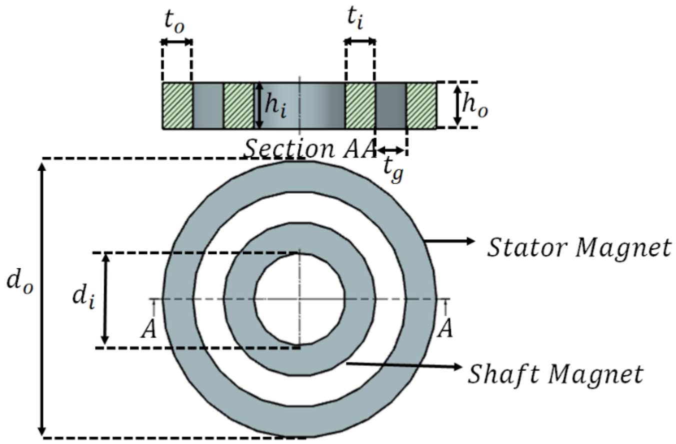

Figure 3.3: Cross section of the hybrid magnetic bearings

The inner diameter of the ring magnet superimposed on the rotor is represented by d_i. The outer diameter of the ring magnet superimposed on the stator is represented by d_o. The thickness of the outer ring magnet is represented by t_o and the thickness of the inner ring magnet is represented by t_i. The axial length of the inner ring magnet is represented by the h_i and the axial length of the outer ring magnet is represented by h_o. The passive magnetic bearing magnetic circuit is analyzed using the finite element method. The complete mesh of radial passive magnetic bearing is shown in Figure 2. The mesh is consisted of 2266843 domain elements, 1844 edge elements and 54056 boundary elements. The complete mesh of the passive magnetic bearing system is shown in Figure 3.4.

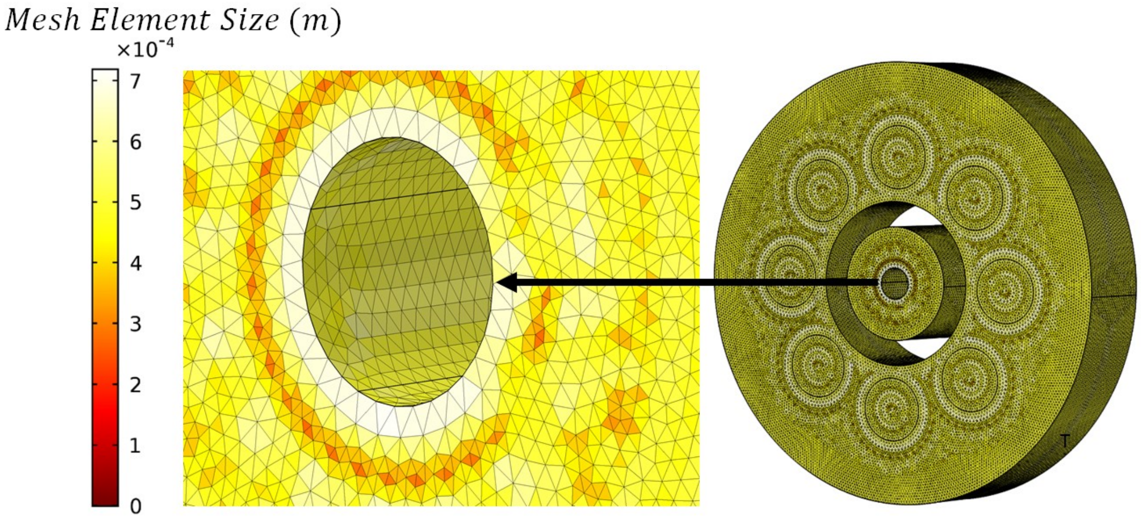

Figure 3.4: Mesh of the passive magnetic bearing system

The magnetic flux density plot of the passive magnetic bearing is shown in Figure 3.5. The maximum magnetic flux density distribution is at the edges of the permanent magnets ranging up to 800 mT. The corresponding contour plot of the passive magnetic bearing system is as shown in Figure 3.6.

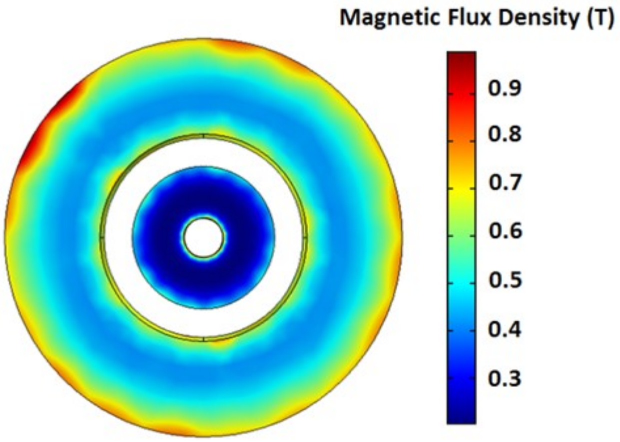

Figure 3.5: Magnetic flux density plot of the passive magnetic bearing

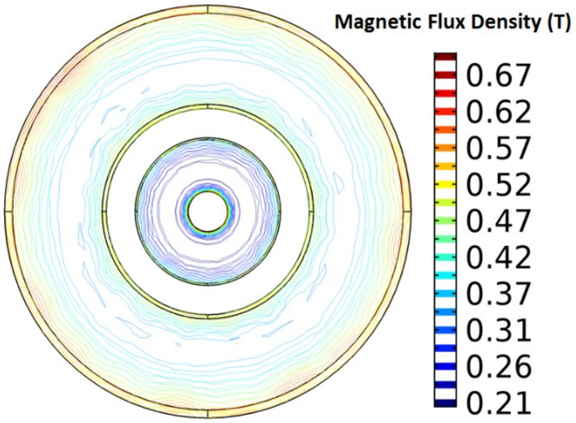

Figure 3.6: The contour plot of the magnetic flux density for the passive magnetic bearing

The radial stiffness of the passive permanent magnetic bearing changes with the thickness and axial length of the ring permanent magnets installed on the shaft and the stator. The axial length of the stator permanent magnet h_o and the axial length of the rotor ring permanent magnet are varied from 5 mm to 20 mm in order to see the effect of these axial lengths on the stiffness of the overall permanent magnetic bearing. Figure 3.7 shows the results of varying the length of the axial lengths with respect to the radial stiffness of the passive permanent magnetic bearing.

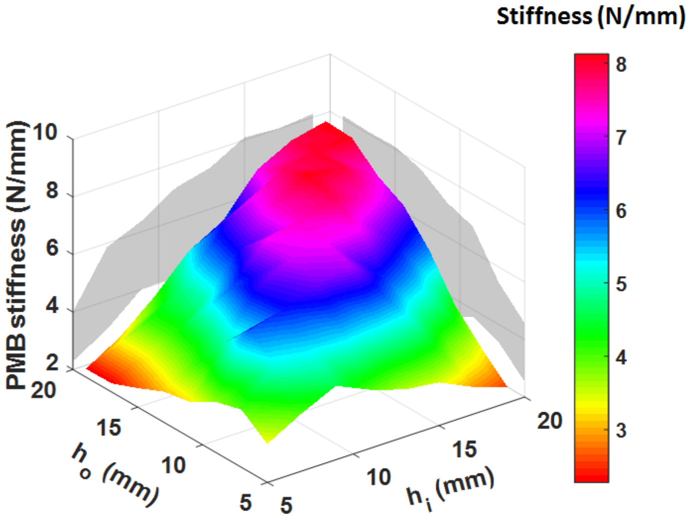

Figure 3.7: The variation of the stiffness of the passive permanent magnetic bearing with the axial lengths of the ring magnets installed on the rotor and the stator. The thicknesses of the two magnets are kept constant.

The thicknesses of the two ring permanent magnets are kept constant in this analysis. The thickness of the ring magnet installed on the rotor is kept fixed with $t_i = 7.5\ mm$ and $t_o = 10\ mm$. The outer diameter of the stator ring permanent magnet is 50 mm and the inner diameter of the rotor ring magnet is 5 mm.

A parametric sweep is given to the thickness of the rotor ring magnet and the stator ring magnet and the corresponding effect upon the stiffness of the passive permanent magnetic bearings is calculated. The axial lengths of the ring magnets are kept constant. Figure 3.8 shows the corresponding results.

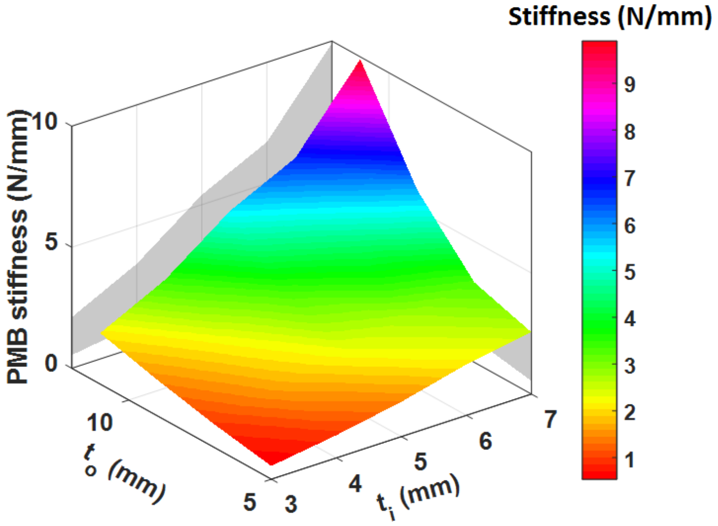

Figure 3.8: The variation of the stiffness of the passive permanent magnetic bearing with respect to the thicknesses of the ring permanent magnets. The axial lengths of the permanent magnets are kept constant.

The axial lengths of the ring permanent magnets are kept as constant. The axial length of the rotor ring permanent magnet, as well as the axial length of the stator ring permanent magnet is kept as 15 mm. The outer dimeter of the stator magnet is again 50 mm and the inner diameter of the rotor ring permanent magnet is 5 mm. Figure 3.9 shows the overall magnetic flux density norm across the passive permanent magnetic bearings. At the surface of the permanent magnets, the magnetic flux density norm is 515 mT.

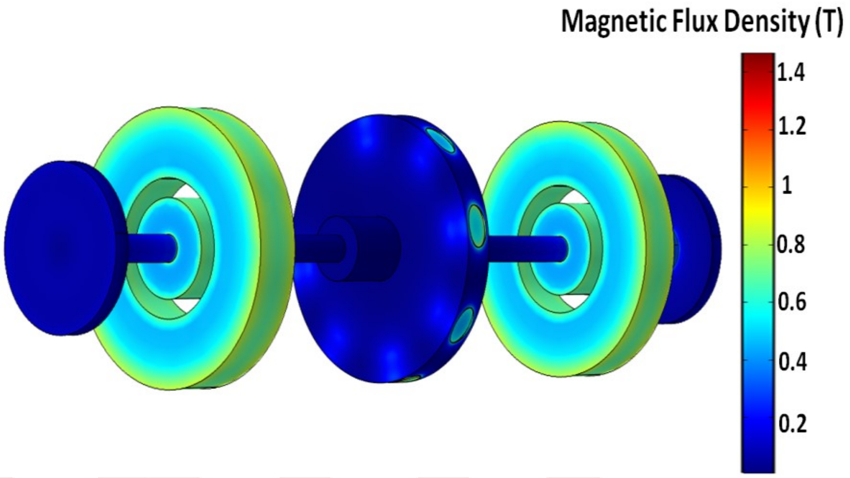

Figure 3.9: The overall magnetic flux distribution across the permanent magnets used in the passive permanent magnetic bearing system

Based on the optimization performed, the parameters are selected as $t_i = 7.5\ mm$, $h_i = 15\ mm$, $t_o = 10\ mm\ h_o = 15\ mm$. The stiffness of each of the passive permanent magnetic bearing is 8.09 N/mm in the radial direction. The overall radial stiffness of the combined two passive magnetic bearings is 16.18 N/mm. The passive permanent magnet bearings exert a force in the axial direction on the rotor. This force acts as a disturbance force and the electromagnets should control this axial disturbance force by adjusting the currents in the electromagnets in order to stabilize the rotor at the equilibrium position. This force increases as the stiffness of the passive magnetic bearing increases. A parametric sweep is given to the rotor in the axial direction and the force on the rotor due to the two passive permanent magnet bearings is calculated. Figure 3.10 shows the axial force exerted on the rotor with respect to the axial displacement of the rotor. At a distance of 0.8 mm from the equilibrium position, the force exerted on the rotor is 16.26 N. This is the maximum force which the axial direction electromagnets should overcome in order to displace the rotor back to the equilibrium position.

A parametric sweep is given to the rotor permanent ring magnet from -4 mm to +4 mm and the force on the rotor is calculated in the radial direction on different radial locations. Figure 3.11 shows the rotor magnet and the stator magnet location when the rotor is displaced to the +4 mm distance in the positive direction and Figure 3.12 shows the forces on the rotor in the radial direction at different rotor positions in the radial direction form +4 mm to -4 mm.

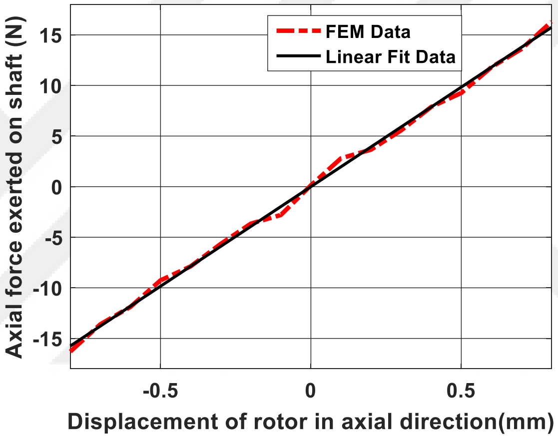

Figure 3.10: Axial force exerted on the rotor with respect to the axial displacement of the rotor due to the passive magnetic bearings

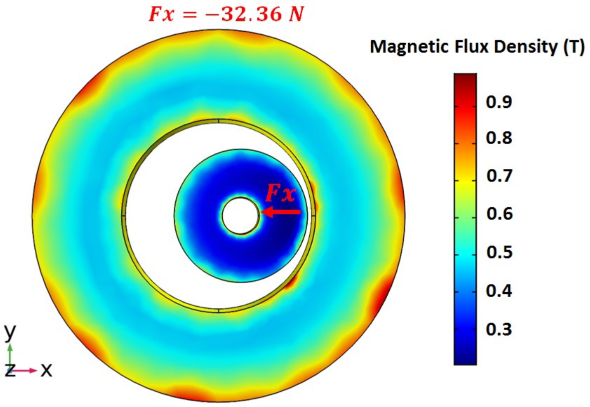

Figure 3.11: Force experienced by the rotor at a distance of 4 mm in the x direction

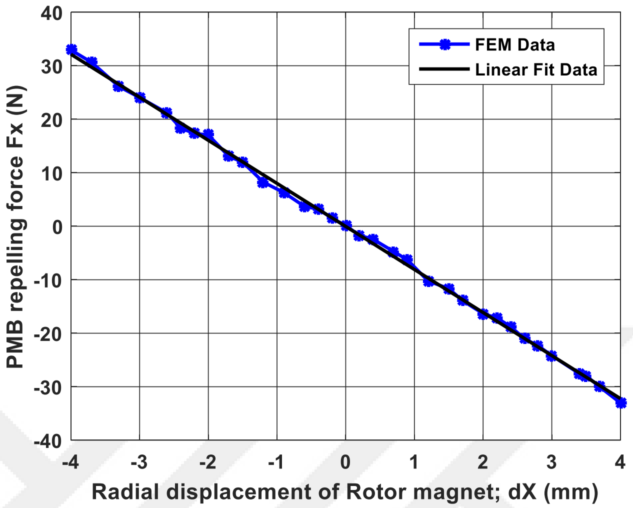

Figure 3.12: The force exerted on the rotor in the radial direction with respect to the radial displacement of the rotor

The force on the rotor at different locations in the radial direction is as shown in Figure 3.12. At a distance of 4 mm in the x direction, the force magnitude on the shaft is -32.36 N in the x direction. The radial stiffness of the PMB is calculated from the results presented in Figure 3.8. The radial stiffness of the PMB comes out to be 8.09 N/mm. The combined stiffness of the two passive permanent magnetic bearings come out to b 16.18 N/mm in the radial direction.

3.3.2 Active Magnetic Bearings

There is always a disturbance force which acts on the rotor in the axial direction. In order to overcome this axial force, and bring back the rotor to the center equilibrium position, the axial electromagnets should be actuated in such a way that the rotor always remains at the equilibrium position. The currents are injected in the coils of the electromagnets in a controlled way in order to control the rotor axial position.

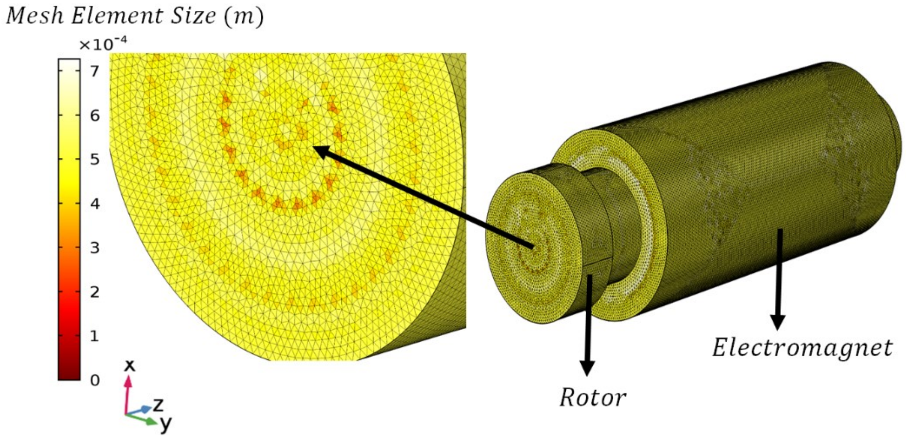

Figure 3.13: Complete mesh of the electromagnet for finite element analysis

There is a position sensor, which measures the axial position of the rotor, and then based the rotor axial position, a control signal is generated by the microprocessor to the power amplifier. The power amplifier drives the two electromagnets accordingly in order to stabilize the rotor. The electromagnet is analyzed using finite element analysis. Figure 3.13 the finite element mesh of the electromagnet. The complete mesh is consisted of 2108 edge elements and 7987026 domain elements.

Figure 3.14 shows the plot of number of turns and current vs the force generated by the electromagnet. Based on the required maximum axial force of 16.26 N, the number of turns are selected as 1600 and the corresponding current is 2 A with an air gap of 0.8 mm.

Figure 3.15 shows the magnetic flux density plot of the electromagnet with the corresponding current and number of turns. The magnetic flux density at the pole surface is 489 mT while at the rotor surface it is 481 mT. Therefore, the leakage flux is negligible in the airgap and almost all the flux is confined inside the airgap between the rotor surface and the electromagnet pole surface.

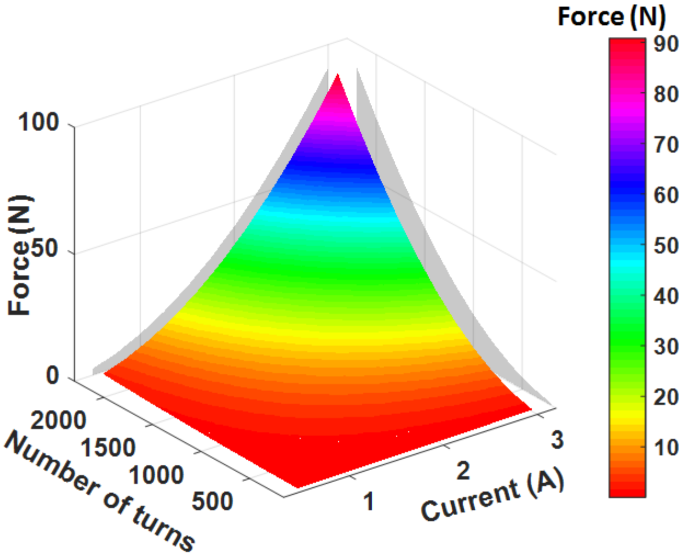

Figure 3.14: The force of the electromagnet vs the number of turns and the current

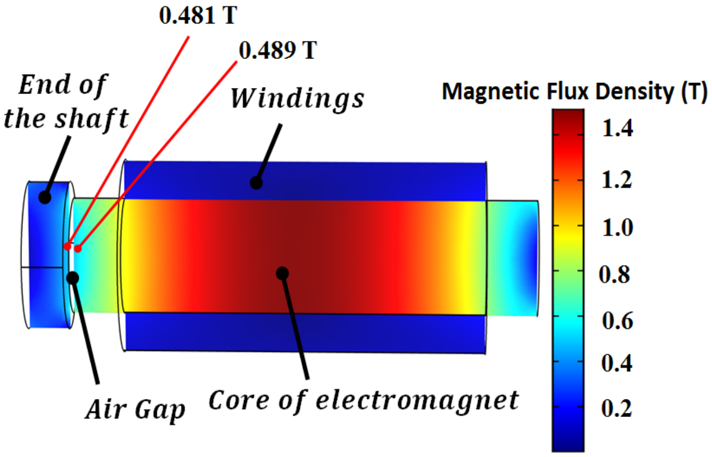

Figure 3.15: The magnetic flux density plot of the electromagnet with number of turns 1600, current of 2 A and airgap of 0.8 mm

3.4 Summary

In this chapter, the design optimization of the hybrid magnetic bearing prototype system is performed. Finite element analysis of the passive permanent magnetic bearing and active magnetic bearing is done. The forces, stiffness, magnetic flux densities, number of turns and current of the electromagnets are optimized according to the design requirements. The overall flow diagram of the design optimization process of the hybrid magnetic bearing prototype system and its control is as shown in Figure 3.16.

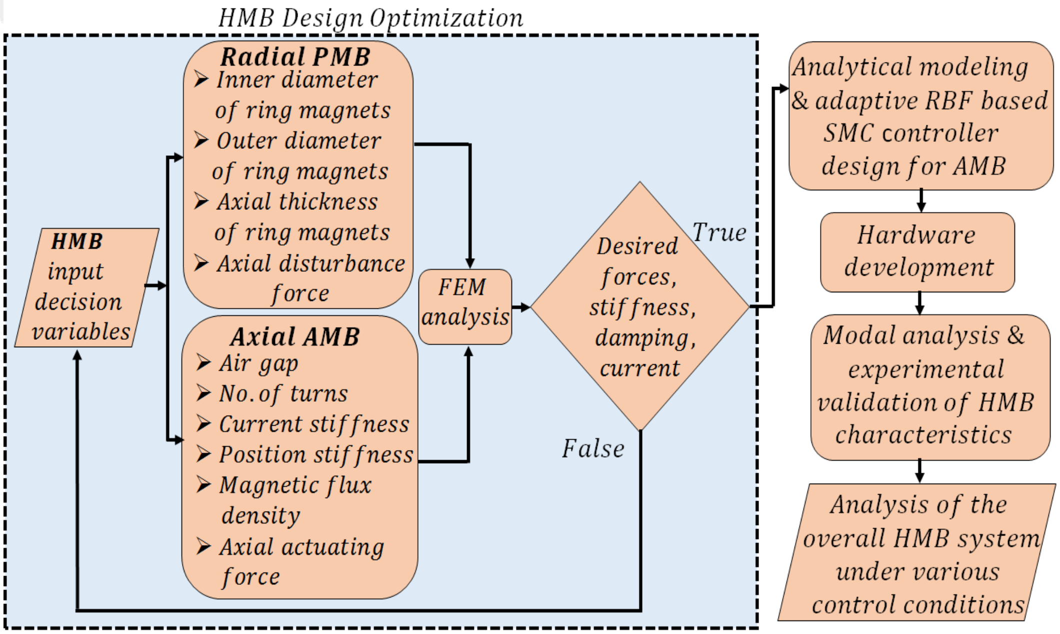

Figure 3.16: Flow diagram of the hybrid magnetic bearing system design, optimization and control

Chapter 4

CONTROL OF HYBRID MAGNETIC BEARING PROTOTYPE

4.1 Introduction

The radial direction of the rotor is stabilized passively using the permanent magnets. In the axial direction, the rotor is stabilized actively by injecting the control currents into the windings of the electromagnets. A position sensor measures the axial position of the rotor and then fed back it to the controller. The controller generates a control signal to the power amplifier, which controls the currents in the windings of the two electromagnets. In this chapter, the analytical modeling of the active magnetic bearing is provided. Based on the developed analytical model, an adaptive sliding mode controller is designed for the active magnetic bearing system.

4.2 Analytical Modeling of Active Magnetic Bearing

Two identical I-core electromagnets are used for controlling the axial direction. Figure 4.1 shows the I-core electromagnet with a part of the rotor end.

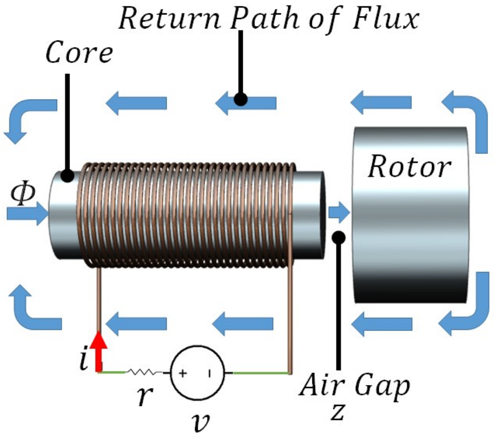

Figure 4.1: The I-core electromagnet with the part of rotor and flux path

As the airgap is small, therefore the leakage flux and fringing flux is neglected. The electrical equivalent circuit of the Figure 4.1 is shown in Figure 4.2.

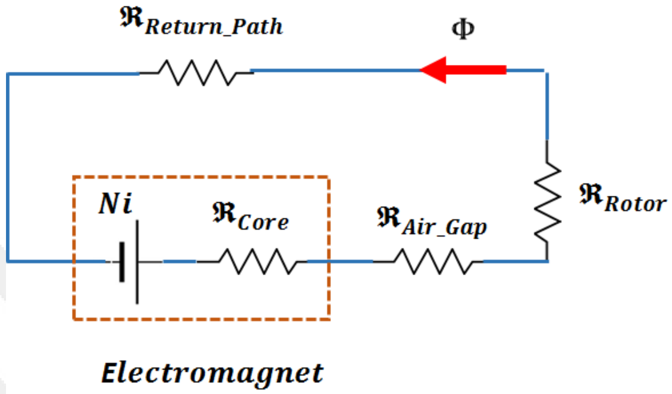

Figure 4.2: The electrical equivalent circuit of the I-core electromagnet, airgap and the rotor part

The electromagnet is driven by a power supply of voltage v with current i. The electrical loop equation of the system given in Fig. 4.2 can be written as below;

$$v = ri + \frac{d\mathcal{L}}{dt} \tag{4.1}$$

where $\mathcal{L} = N\phi$. The magnetic loop equation of the system can be written as:

$$Ni = (\phi_{leakage} + \phi_M)\Re$$

where ϕ is the total magnetic flux, $\phi_{leakage}$ is the leakage flux, ϕ_M is the magnetizing flux, $\Re$ is the total magnetic reluctance, N is the no. of turns and i is the current in electromagnet.

$$\phi_{leakage} = \frac{Ni}{\Re_{leakage}}$$

$$\phi_M = \frac{Ni}{\Re_M}$$

where $\Re_M$ is the sum of all reluctances in the closed magnetic circuit and is given as follows:

$$\Re_M = \Re_{Core} + \Re_{Air\_Gap} + \Re_{Rotor} + \Re_{Return\_Path}$$

Defining $\Re_C = \Re_{Rotor} + \Re_{Core} + \Re_{Return\_Path}$ = Constant

Therefore,

$$\mathcal{L} = (L_M + L_{leakage})i = (\frac{N^2 i}{\Re_M} + \frac{N^2 i}{\Re_{leakage}})$$

where L_M is the magnetizing inductance and $L_{leakage}$ is the leakage inductance.

By putting $\Re_{Air\_Gap} = \frac{z}{\mu_0 A_g}$, we get;

$$L_M = \frac{N^2}{\Re_C + \frac{z}{\mu_0 A_g}} = \frac{\mu_0 A_g N^2}{\mu_0 A_g \Re_C + z}$$

where A_g is the cross section area of air gap and z is the air gap width. The leakage inductance is assumed to be constant and negligible.

When z becomes $z(t)$, then $L_M = L_M(z)$ and Equation (4.1) can be written as;

$$v = ri + i\frac{dL_M(z)}{dt}\frac{dz}{dt} + \left(L_M(z)\right)\frac{di}{dt} \tag{4.2}$$

$$L_M(z) = \frac{\mu_0 A_g N^2}{\mu_0 A_g \Re_C + z} = \frac{k}{\propto + z} \cong \frac{k}{z} \quad for\ z > 0 \tag{4.3}$$

where $k = \mu_0 A_g N^2$ and $\propto = \mu_0 A_g \Re_C$

Therefore, the electromagnetic force exerted on the shaft one side by the I-core electromagnet is given as follows:

$$F_m(i, z) = \frac{1}{2} i^2 \frac{dL_M(z)}{dt} = -K\frac{i^2}{z^2} \tag{4.4}$$

where K= $\frac{\mu_0 A_g N^2}{2}$ and the negative sign shows that the electromagnetic force is always exerted in the direction in which it will reduce the overall magnetic reluctance.

For the prototype of the magnetic bearing system shown in Figure 4.3, the equation of motion can be written as shown in Equation 4.4.

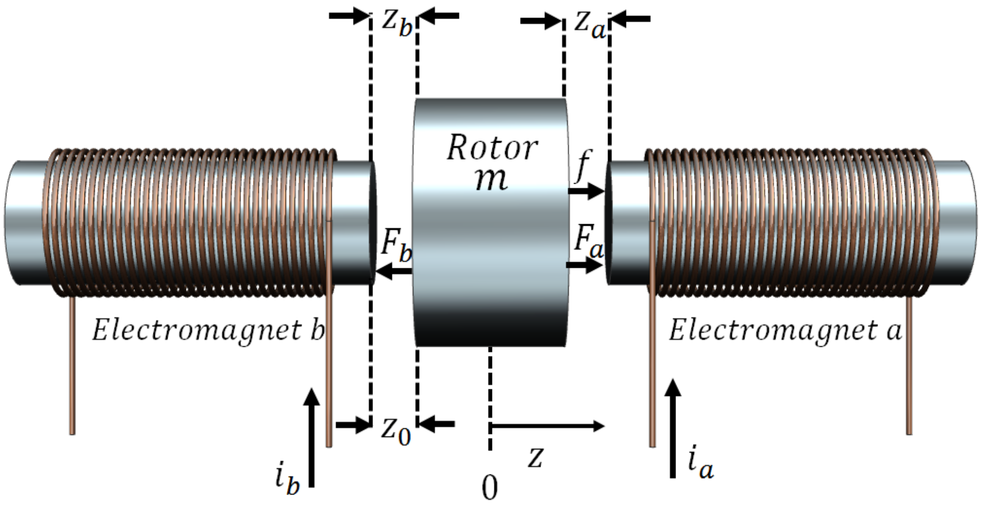

Figure 4.3: The active magnetic bearing prototype with the two I-core electromagnets

$$m\ddot{z} = F_a - F_b + f_d$$

$$m\ddot{z} = -K\left(\frac{i_a}{z_a}\right)^2 + K\left(\frac{i_b}{z_b}\right)^2 + f_d \tag{4.6}$$

or

$$m\ddot{z} = -K\left(\frac{i_a}{z_0 - z}\right)^2 + K\left(\frac{i_b}{z_0 + z}\right)^2 + f_d \tag{4.7}$$

where i_a is the current in the electromagnet a, i_b is the current in the electromagnet b, z_0 is the distance of the rotor from each of the electromagnets when the rotor is stabilized at the equilibrium position, m is the mass of the shaft, z is the displacement covered by the shaft and $f_d$is the external force acting on the shaft as a disturbance. The two I-core electromagnets which are shown in Figure 4.3 are working in a differential driving mode, in which the current in one electromagnet will increase and the current in the second electromagnet will decrease accordingly based upon the displacement z of the rotor. The biased current i_{bias} is the fixed current going to each of the electromagnets and the controlling current i_z is added and subtracted to the bias current accordingly in the two electromagnets. Equation (4.7) can be written as follows.

$$m\ddot{z} = -K\left(\left(\frac{i_{bias}+i_z}{z_0-z}\right)^2 - \left(\frac{i_{bias}-i_z}{z_0+z}\right)^2\right) + f_d \tag{4.8}$$

Equation (4.8) shows that the active magnetic bearing prototype has a strong nonlinear relation between the currents and the displacements and it is a nonlinear and a nonaffine system. By choosing the variables as below:

$z_1 = z$, $z_2 = \dot{z}$ and $u_c = i_z$, the equation (4.8) can be written as follows:

$$\begin{cases} \dot{z_1} = z_2 \\ \dot{z_2} = f_z(z_1, u_c) + \varphi_d \\ c = z_1 \end{cases} \tag{4.9}$$

where $f_z = -\frac{K}{m}\left(\left(\frac{i_{bias}+i_z}{z_0-z}\right)^2 - \left(\frac{i_{bias}-i_z}{z_0+z}\right)^2\right)$ and $\varphi_d = \frac{f_d}{m}$

For the system shown in Equation (4.9), a time varying system which is affine and nonlinear can be obtained using the expansion given by Taylor series. The linearization is performed around a linearization point μ_l and is given as follows:

$$\begin{gathered} \dot{z_1} = z_2 \\ \dot{z_2} = f_z(z_1, \mu_l) + g_z(z_1, \mu_l)\Delta u_c + f_d(t) \\ c = z_1 \end{gathered} \tag{4.10}$$

where $\Delta u_c = u_c - \mu_l$, $g_z(z_1, \mu_l) = \left.\frac{\partial f_z(z_1,\mu_l)}{\partial u_c}\right|_{u_c=\mu_l}$ and $f_d(t)$ is the disturbances and the unmodeled dynamics and with $f_d(t) \leq F_0$.

A nonlinear affine system can be obtained from Equation (4.10) as follows:

$$\begin{cases} \dot{z_1} = z_2 \\ \dot{z_2} = f_{zl}(z_1, \mu_l) + g_{zl}(z_1, \mu_l)u_c + f_d(t) \\ c = z_1 \end{cases} \tag{4.11}$$

where $f_{zl}(z_1, \mu_l) = f_z(z_1, \mu_l) - g_z(z, \mu_l)\mu_l$ and $g_{zl}(z_1, \mu_l) = -\frac{2K}{m}\left(\frac{i_{bias}+\mu_l}{(z_0-z_1)^2} + \frac{i_{bias}-\mu_l}{(z_0+z_1)^2}\right)$.

4.3 Adaptive Sliding Mode Controller Design

Let the reference output of the active magnetic bearing be represented by z_r. Then the error between the actual output and the reference output is given as follows:

$$s = \vartheta e + \dot{e} \tag{4.12}$$

where $\vartheta > 0$. After the derivative of Equation (4.12), the following expression is obtained:

$$\dot{s} = \ddot{z_r} - f_{zl} - g_{zl}u_c - f_d(t) + \vartheta\dot{e} \tag{4.13}$$

The control law can be derived from Equation (4.13) as follows:

$$u_c = \frac{1}{g_{zl}}(\ddot{z_r} + \vartheta\dot{e} - f_{zl} + \zeta sgn(s)) \tag{4.14}$$

The $L = \frac{1}{2}s^2$ is selected as the Lyapunov function. Hence;

$$\dot{L} = s\dot{s} = s(\ddot{z_r} - f_{zl} - f_d(t) - g_{zl}u_c + \vartheta\dot{e})$$

$$= s(\ddot{z_r} - f_{zl} - \left(-f_{zl} + \ddot{z_r} + \vartheta\dot{e} + \zeta sgn(s)\right) - f_d(t) + \vartheta\dot{e})$$

$$= -s(f_d(t)) - \zeta|s|$$

where ζ is a rate parameter with constant value and $\zeta > 0$. Therefore, if we choose $\zeta > F_0$, then we obtain $s\dot{s} \leq 0$.

In this thesis, Radial Basis Function (RBF) based adaptive approximation of the functions f_{zl} and g_{zl} is performed. The radial basis function can be written as follows:

$$\xi_j = e^{-\left(\frac{\|z_t - c_j\|}{\sqrt{2}b_j}\right)^2} \tag{4.15}$$

where ξ is the output of the radial basis function, $\boldsymbol{z_t}$ is the input vector to the RBF network, and $\boldsymbol{z_t}$ is chosen as $\boldsymbol{z_t} = \begin{bmatrix} e \\ \dot{e} \end{bmatrix}$, j is the hidden layer nodes of network, The two functions can be approximated as follows:

$$f_{zl} = \boldsymbol{P}^{\boldsymbol{T}}\boldsymbol{\xi}_{\boldsymbol{f}}(\boldsymbol{z}) + \delta_f$$

$$g_{zl} = \boldsymbol{Q}^{\boldsymbol{T}}\boldsymbol{\xi}_{\boldsymbol{g}}(\boldsymbol{z}) + \delta_g$$

where $\boldsymbol{P}$ and $\boldsymbol{Q}$ are the weights of the ideal RBF network, $\xi = \left[\xi_j\right]^T$ represents the output of the Gaussian function, the approximation errors are represented by the δ_f and δ_g and also $\delta_g \le \delta_{Ng}$ and $\delta_f \le \delta_{Nf}$ and f_{zl} and g_{zl} are the RBF network ideal outputs.

Therefore,

$$\hat{f}_{zl}(z) = \widehat{\boldsymbol{P}}^{\boldsymbol{T}}\boldsymbol{\xi}_f(\boldsymbol{z})$$

$$\hat{g}_{zl}(z) = \widehat{\boldsymbol{Q}}^{\boldsymbol{T}}\boldsymbol{\xi}_g(\boldsymbol{z})$$

Equation (4.14) can be written as follows:

$$u_c = \frac{1}{\hat{g}_{zl}}\left(\ddot{z}_r + \vartheta\dot{e} - \hat{f}_{zl} + \zeta sgn(s)\right) \tag{4.16}$$

From Equation (4.13) we can write that:

$$\dot{s} = \ddot{z}_r - \hat{f}_{zl} - f_d(t) - \hat{g}_{zl}u_c + (\hat{g}_{zl} - g_{zl})u_c + \vartheta\dot{e}$$

$$= \ddot{z}_r - \hat{f}_{zl} - f_d(t) - \hat{g}_{zl}\frac{1}{\hat{g}_{zl}}\left(\ddot{z}_r + \vartheta\dot{e} - \hat{f}_{zl} + \zeta sgn(s)\right) + (\hat{g}_{zl} - g_{zl})u_c + \vartheta\dot{e})$$

$$=(\hat{f}_{zl} - f_{zl}) - f_d(t) + (\hat{g}_{zl} - \hat{g}_{zl})u_c - \zeta sgn(s)$$

$$=\tilde{f}_{zl} - f_d(t) + \tilde{g}_{zl}u_c - \zeta sgn(s)$$

$$=\widetilde{\boldsymbol{P}}^{\boldsymbol{T}}\boldsymbol{\varphi}_f(\boldsymbol{z}) - \delta_f - f_d(t) + (\widetilde{\boldsymbol{Q}}^{\boldsymbol{T}}\boldsymbol{\xi}_g(\boldsymbol{z}) - \delta_g)u_c - \zeta sgn(s)$$

where $\tilde{f}_{zl} = \hat{f}_{zl} - f_{zl} = \widetilde{\boldsymbol{P}}^{\boldsymbol{T}}\boldsymbol{\xi}_f(\boldsymbol{z}) - \delta_f$

$\tilde{g}_{zl} = \hat{g}_{zl} - g_{zl} = \widetilde{\boldsymbol{Q}}^{\boldsymbol{T}}\boldsymbol{\xi}_g(\boldsymbol{z}) - \delta_g$

$\widetilde{\boldsymbol{P}} = \widehat{\boldsymbol{P}} - \boldsymbol{P}$ and $\widetilde{\boldsymbol{Q}} = \widehat{\boldsymbol{Q}} - \boldsymbol{Q}$

The Lyapunov function is selected as follows:

$$L = \frac{1}{2}s^2 + \frac{1}{2\kappa_1}\widetilde{\boldsymbol{P}}^{\boldsymbol{T}}\widetilde{\boldsymbol{P}} + \frac{1}{2\kappa_2}\boldsymbol{Q}^{\boldsymbol{T}}\widetilde{\boldsymbol{Q}} \tag{4.17}$$

After taking the derivative of Equation (4.17), we get:

$$\dot{L} = s\dot{s} + \frac{1}{\kappa_1}\widetilde{\boldsymbol{P}}^{\boldsymbol{T}}\dot{\widetilde{\boldsymbol{P}}} + \frac{1}{\kappa_2}\widetilde{\boldsymbol{Q}}^{\boldsymbol{T}}\dot{\boldsymbol{Q}}$$

$$= \mathrm{s}(\widetilde{\boldsymbol{P}}^{\boldsymbol{T}}\boldsymbol{\xi}_f(\boldsymbol{z}) - \delta_f - f_d(t) + \left(\widetilde{\boldsymbol{Q}}^{\boldsymbol{T}}\boldsymbol{\xi}_g(\boldsymbol{z}) - \delta_g\right)u_c - \zeta sgn(s)) + \frac{1}{\kappa_1}\widetilde{\boldsymbol{P}}^{\boldsymbol{T}}\dot{\widehat{\boldsymbol{P}}} + \frac{1}{\kappa_2}\widetilde{\boldsymbol{Q}}^{\boldsymbol{T}}\dot{\widehat{\boldsymbol{Q}}}$$

$$= s\left(-\delta_g u_c - \delta_f - f_d(t) - \zeta sgn(s)\right) + \boldsymbol{P}^{\boldsymbol{T}}\left(s\boldsymbol{\xi}_f(\boldsymbol{z}) + \frac{1}{\kappa_1}\dot{\widehat{\boldsymbol{P}}}\right) + \widetilde{\boldsymbol{Q}}^{\boldsymbol{T}}\left(s\boldsymbol{\xi}_g(\boldsymbol{z})u_c + \frac{1}{\kappa_1}\dot{\widehat{\boldsymbol{Q}}}\right)$$

Therefore, the adaptive laws are designed as follows:

$$\dot{\widehat{\boldsymbol{P}}} = -\kappa_1 s\boldsymbol{\xi}_f(\boldsymbol{z})$$

$$\dot{\widehat{\boldsymbol{Q}}} = -\kappa_2 s\boldsymbol{\xi}_g(\boldsymbol{z})u_c \tag{4.18}$$

Therefore,

$$\dot{L} = s\left(-\delta_g u_c - \delta_f - f_d(t) - \zeta sgn(s)\right)$$

$$= s\left(-\delta_g u_c - \delta_f - f_d(t)\right) - \zeta|s|$$

Hence, if we choose:

$\eta \geq max\{\delta_g u_c + \delta_f + f_d(t)\}$, then we get the expression $\dot{L} \leq 0$ and it completes the proof of the stability. The complete block diagram of the control structure is shown in Figure 4.4.

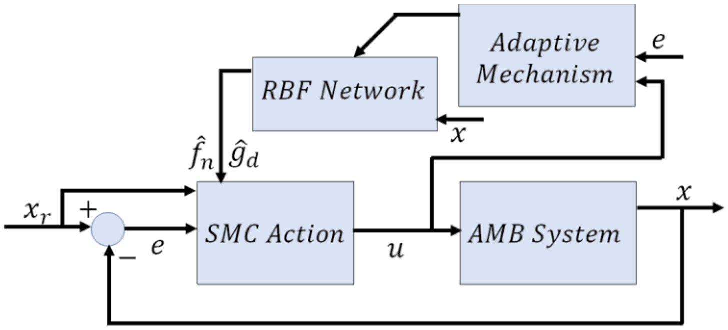

Figure 4.4: Overall control block diagram

4.4 Simulation Results

By utilizing the proposed adaptive sliding mode controller, a simulation is run using the same design parameters, as those of the physical prototype system. The mass of the shaft is 0.132 kg. The force constant of the electromagnet K is 3.6×10^{-6}. The bias current i_{bias} is 2 A. The radial basis function has two inputs, five hidden layers and one output. The value for the parameter c_j is selected as 0.25 and for b_j is 6. The initializing value for the parameter of weight is 0.1.

The Equation (4.14) is used for designing the control law and the Equation (4.18) is used for designing the adaptive law for the prototype system position control. The parameter ϑ is selected as 20 and the parameter ζ is selected as 10. The parameter κ_1 is 10 and the parameter κ_2 is 1. These are the optimal values for the two parameters because the output response tends to oscillate beyond these values.

Figure 4.5 shows the output displacement of the rotor in response to the step command of 0.8 mm which is the axial airgap between the rotor and the surface of the electromagnet. The control current in each of the electromagnet is shown in the Figure 4.6. A sinusoidal disturbance of 0.1 sin(t) is included to the system dynamics in order to model the unmodeled dynamics. This disturbance if not controlled properly, will result in an acceleration of 0.75 m/s^2 in the output response of the bearing.

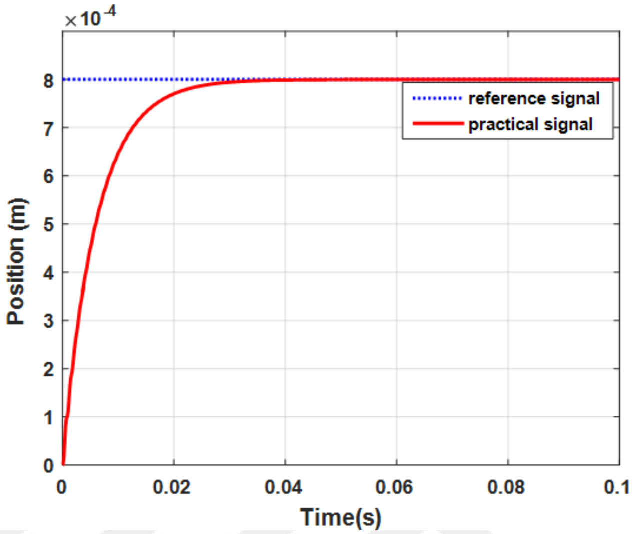

Figure 4.5: The active magnetic bearing position reference following a step of 0.8 mm

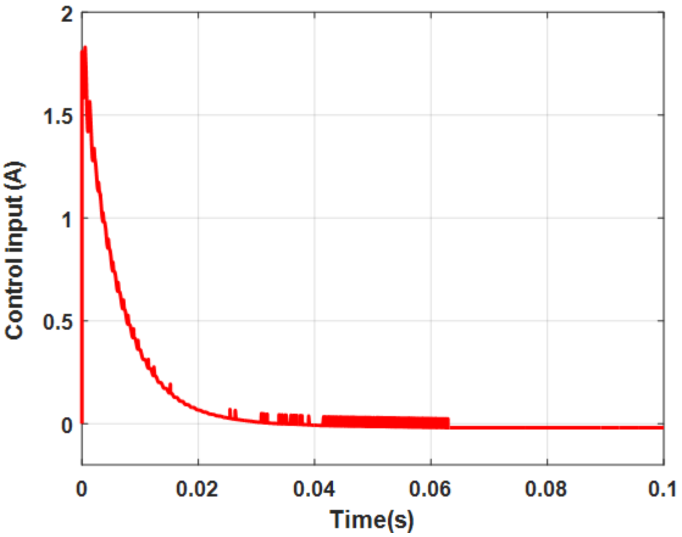

Figure 4.6: The corresponding control current in each of the electromagnet

The corresponding plots for the functions f_{zl} and g_{zl} are shown in Figure 4.7 and Figure 4.8 respectively.

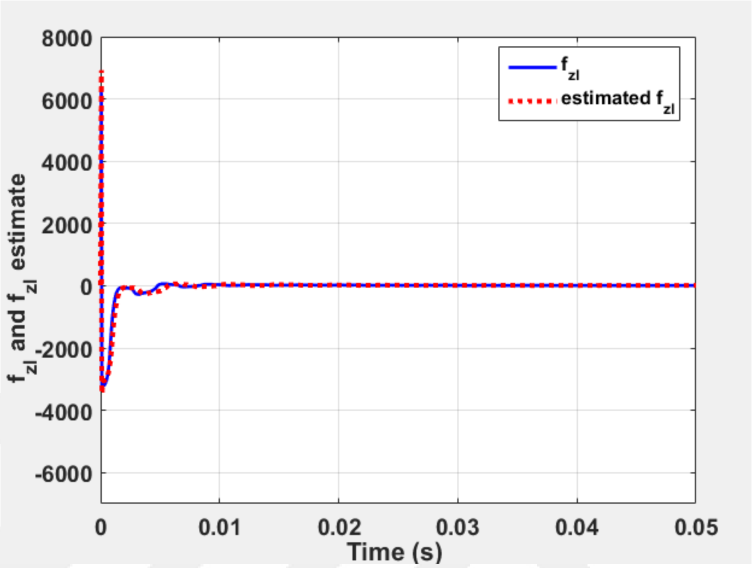

Figure 4.7: f_{zl} and estimated f_{zl}

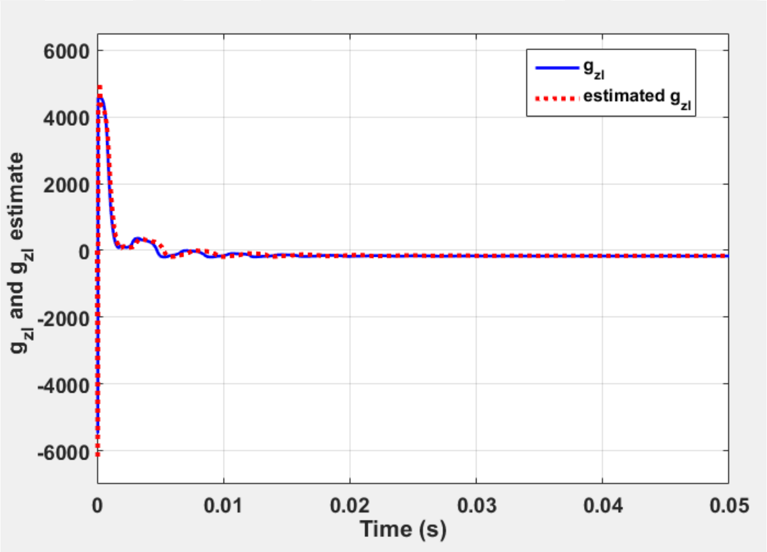

Figure 4.8: g_{zl} and estimated g_{zl}

The corresponding phase plane trajectories for the error and the change in error are shown in Figure 4.9 and Figure 4.10. The Figure 4.9 shows the phase place trajectories with 0.1sin(20πt) included as the sinusoidal interference and Figure 4.10 shows the phase plane trajectory wit 1sin(20πt) added as the unmodeled dynamics.

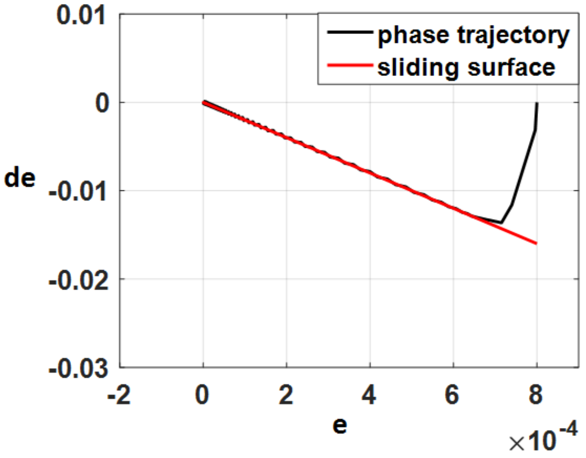

Figure 4.9: Phase plane trajectory with 0.1sin(20πt) as the added interference

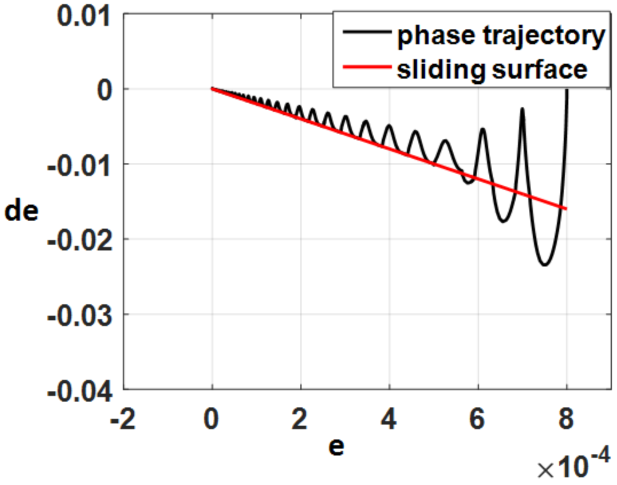

Figure 4.10: Phase plane trajectory with 1sin(20πt) as the added interference

For seeing the anti-interference property of the proposed controller, a constant interference force of 5.18 N is included in the system at time 2 sec. The resulting position and current of the active magnetic bearing system are shown in Figure 4.11 and Figure 4.12 respectively.

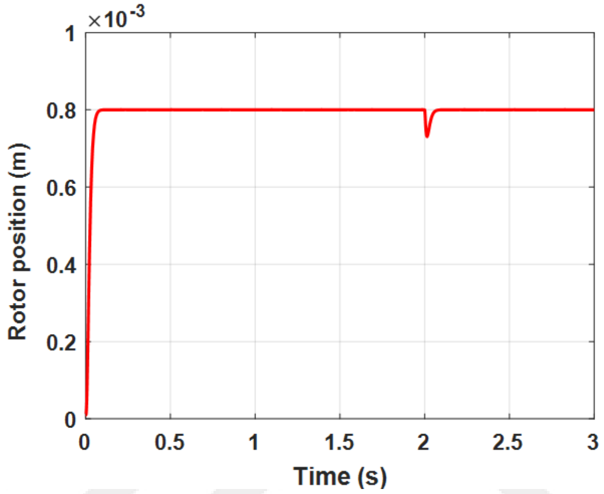

Figure 4.11: The output response of the controller with the 5.18 N step disturbing force applied at 2 secs

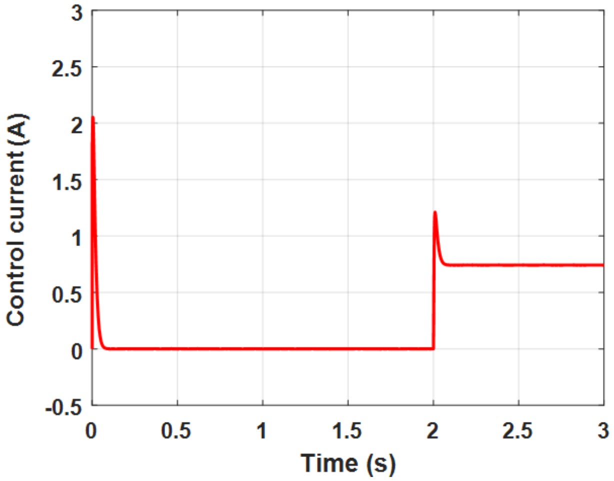

Figure 4.12: The control current after the 5.18 N step disturbing force applied at 2 secs

The corresponding plots for the estimates of the functions f_{zl} and g_{zl} are shown in Figure 4.13 and Figure 4.14 respectively after the application of disturbance at 2 secs.

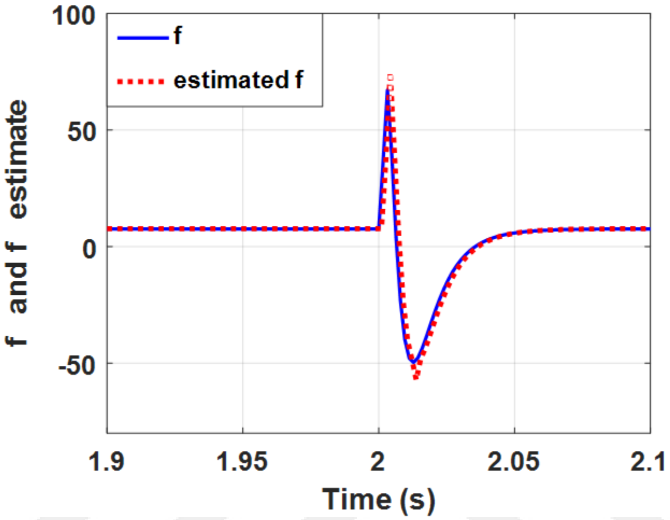

Figure 4.13: f_{zl} and estimated f_{zl}

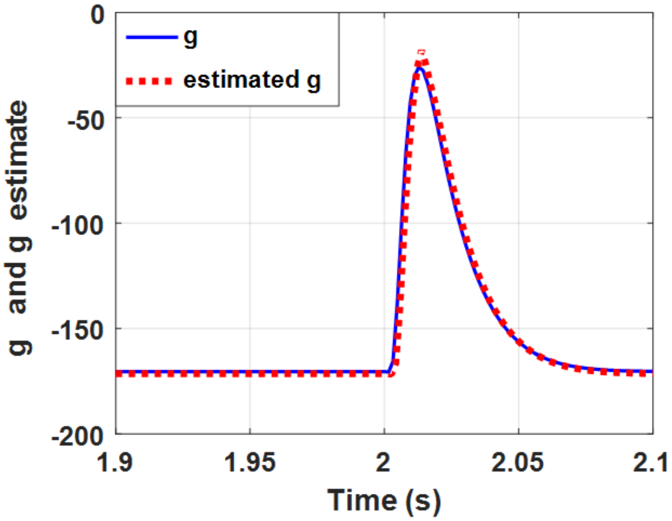

Figure 4.14: g_{zl} and estimated g_{zl}

For seeing the robustness of the proposed controller, the mass of the shaft is varied between the double and half of the original value and the corresponding response is shown in Figure 4.15.

A disturbance of 10 Hz is also included to the system and the resulting response is shown in Figure 4.16. The system gives good robustness against the variation of the parameters as shown in these two Figures.

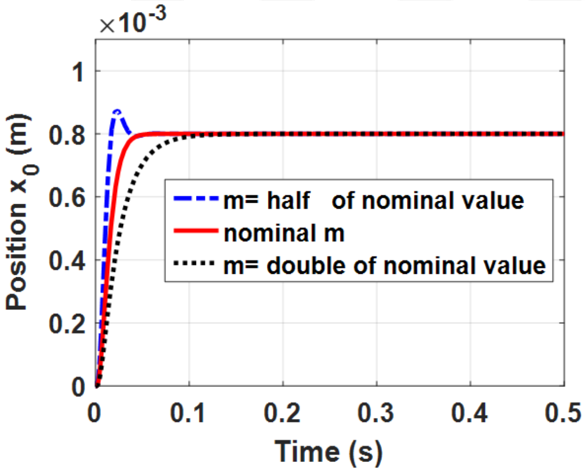

Figure 4.15: The response of the system with mass halved and doubled

For the comparison of the proposed adaptive controller response to the classical control, the proposed controller performance is compared to a well-tuned PID controller. The value of K_p is 13.73, K_i is 127.45 and K_d is 7.25. The corresponding comparison is shown in Figure 4.17 and Figure 4.18.

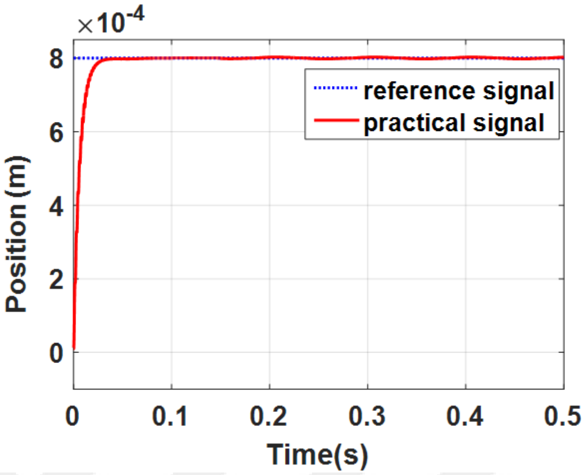

Figure 4.16: The response of the system with the 10 Hz sinusoidal interference included

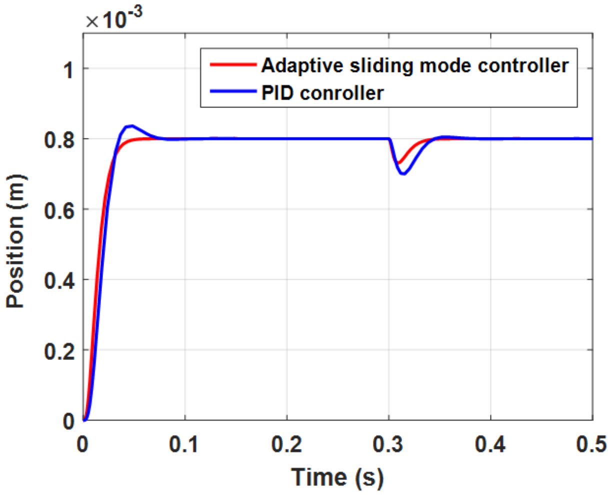

Figure 4.17: The comparison of the proposed adaptive controller and PID controller for step disturbance rejection

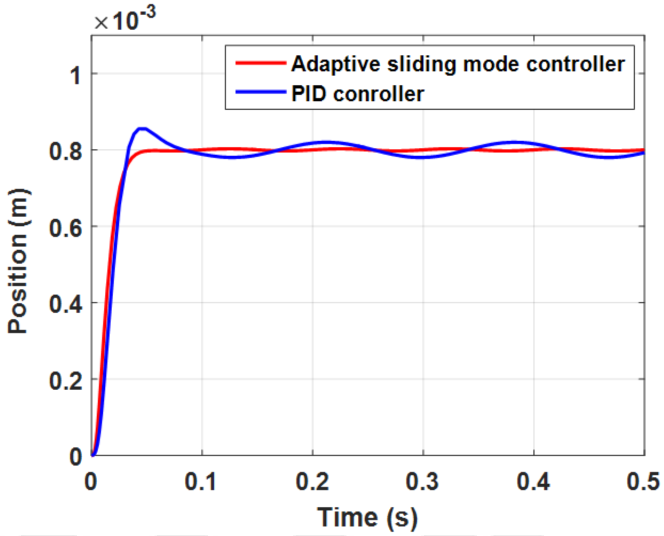

Figure 4.18: The comparison of the proposed adaptive controller and PID controller with sinusoidal interference added

4.5 Summary

In this chapter, an adaptive sliding mode controller is designed for the position tracking of the active magnetic bearing system. The analytical modeling of the system is done and then based on the analytical equations, an adaptive sliding mode controller is designed using the radial basis function. The simulations are done for the designed controller and the performance of the controller is evaluated under different conditions. The performance of the controller is compared with PID controller and the proposed controller shows good robustness against the variations in the parameters of the system and better disturbance rejection property as compared to the PID controller.

Chapter 5

EXPERIMENTAL SETUP AND RESULTS OF HYBRID MAGNETIC BEARING PROTOTYPE

5.1 Introduction

In this chapter, the experimental setup for the designed hybrid magnetic bearing prototype system is provided. The setup is manufactured based on the optimization performed in chapter 3. The magnetic flux, forces and stiffness and damping are experimentally verified. The proposed controller is implemented for the position control of the bearing system. The rotor is rotated at the operating speed and different performance evaluations are carried out at various operating conditions.

5.2 Experimental Setup

The experimental prototype setup for the hybrid magnetic bearing is as shown in Figure 5.1. The shaft is made up of AISI-1010 low Carbon steel.

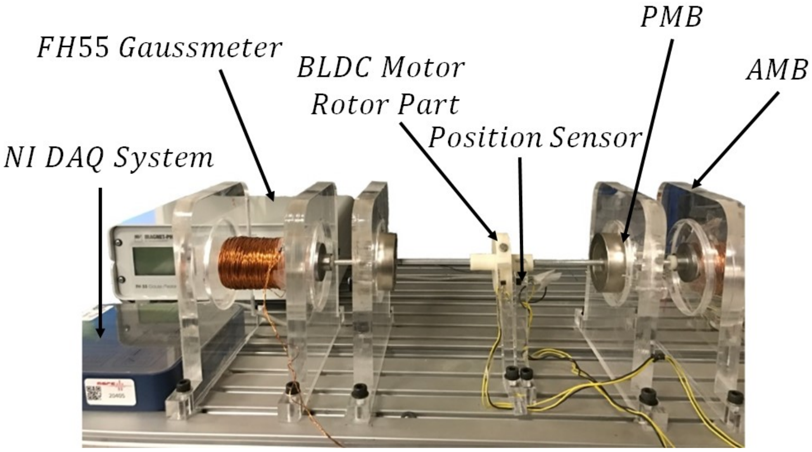

Figure 5.1: Experimental prototype setup for the designed hybrid magnetic bearing

The setup contains two passive permanent magnetic bearings in the radial direction and one active axial direction bearing utilizing two electromagnets. The position of the shaft in the axial direction is measured with an optical sensor. The axial position sensor is QRD1114. It has internal bandwidth of 35 kHz, sensitivity of 1.4 V/mm in the operating range and having a rise time of 10 micro seconds. There is also a filter installed in the sensor in order to block the ambient light effect falling on the surface of the sensor. The noise of the sensor has 0.015 mV standard deviation for the 0 mm to 1 mm range of operation. The shaft mass is 0.131 kg.

The inner diameter of the permanent magnets installed on the rotor is 5 mm, the axial thickness of 15 mm and an outer diameter of 20 mm. The permanent magnets installed on the stator have an inner diameter as 30 mm, axial thickness of 15 mm and an outer diameter of 50 mm. For rotating the shaft around its axis, a two-pole single phase brushless DC (BLDC) motor is designed for the shaft. The shaft contains a section for the BLDC motor containing permanent magnets. FH55 Gaussmeter is used in order to measure the magnetic flux densities of the permanent magnets and the electromagnets at different values of the currents. In order to measure the axial disturbance force generated because of the radial permanent magnet rings, a Kistler table type dynamometer is used as shown in Fig. 5.2.

The stiffness and the damping of the permanent magnetic bearing is found experimentally using the impact hammer test as shown in Figure 5.3. The number of turns of each electromagnet are kept 1600 with copper wire of 19 gauge and the value of the bias current is 2 A. The low carbon steel ISI-1010 is selected for the manufacturing of the electromagnets cores.

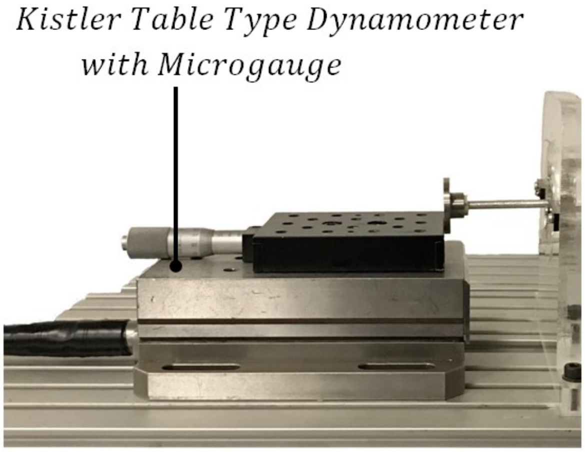

Figure 5.2: A Kistler table type dynamometer for measuring the axial disturbance force exerted on the shaft due to the passive magnetic bearings

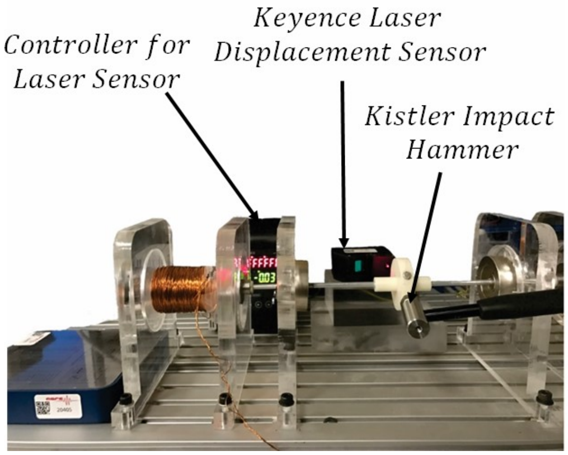

Figure 5.3: Experimental setup for measuring the radial stiffness and damping of the hybrid magnetic bearing

5.3 Experimental Results

The axial disturbance force acting on the shaft in the axial direction is measured using the Kistler table type dynamometer. Figure 5.4 shows the results of the experimental axial force acting on the shaft in the axial direction. The maximum force on the rotor is 15.97 N when the rotor touches one side of the electromagnet.

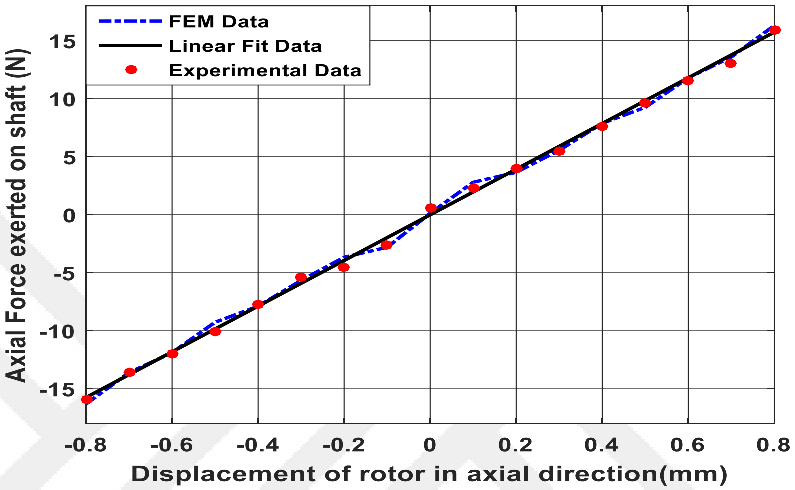

Figure 5.4: The axial force acting on the shaft as a result of the radial passive permanent magnet bearing

Figure 5.5 shows the magnetic flux densities of the two electromagnets as measured with the FH55 Gaussmeter. They have almost same magnetic flux density. The magnetic flux density at the surface of the electromagnets is 486 mT. Using the Kistler dynamometer, the current stiffness and position stiffness of the two electromagnets are experimentally found. The position stiffness is 19.1 N.mm and the current stiffness value is -21.6 N.A as shown in Figure 5.6 and Figure 5.7. The axial stiffness of the active magnetic bearing is found to be 9.9×10^4 N/mm and the axial damping is 215.05 N.s/m. The radial stiffness is 16.43 N/mm and radial damping ratio is 5.1 % as shown in Table 5.1 using the impact hammer test of Figure 5.3.

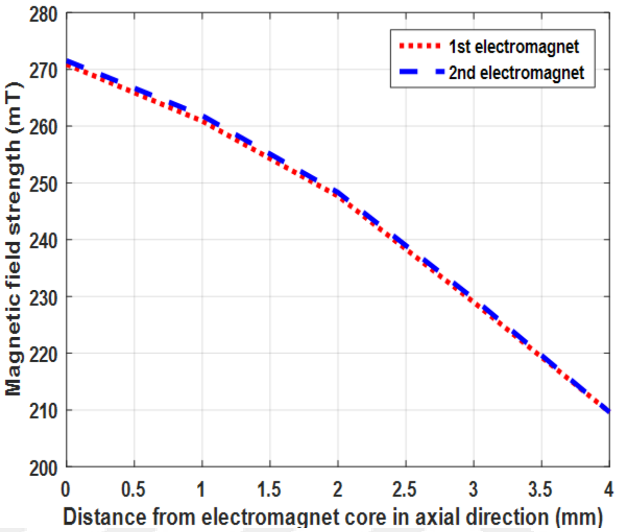

Figure 5.5: Measured magnetic flux densities of the two manufactured electromagnets using the FH55 Gaussmeter

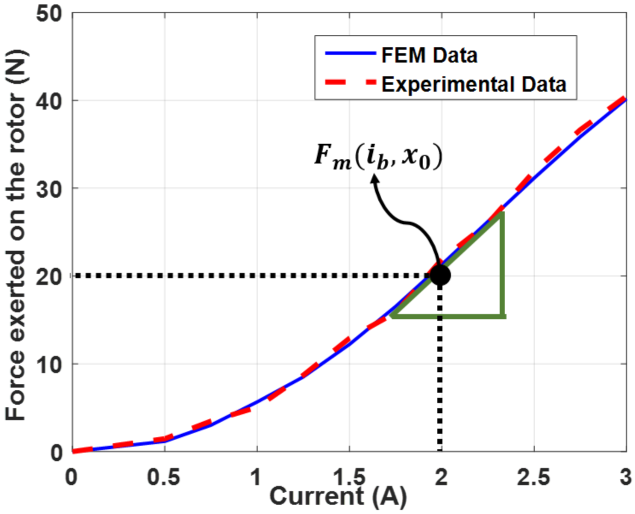

Figure 5.6: The current stiffness of the manufactured electromagnets

Table 5.1: The results obtained from the modal analysis

Natural Frequency [Hz]	Damping Ratio [%]	Modal Stiffness [N/m]	Mass [kg]
59.3	5.1	16430	0.132

The frequency response function (FRF) of the radial direction modal analysis for the passive magnetic bearing is shown in Figure 5.7 and Figure 5.8.

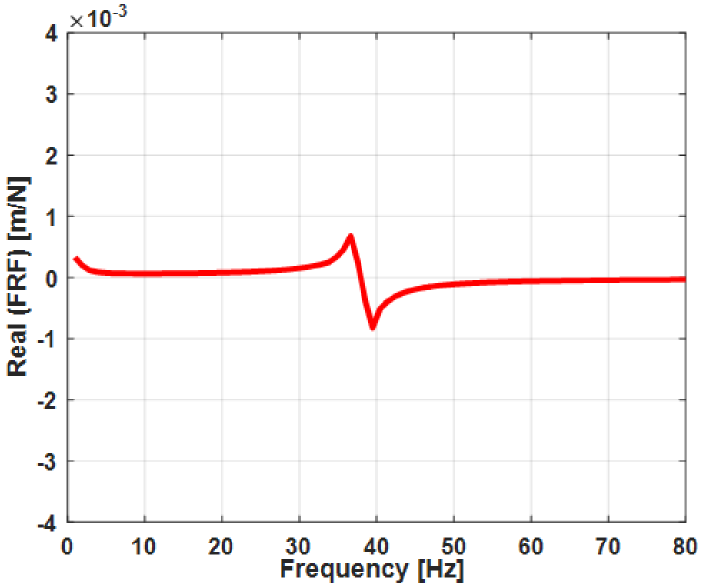

Figure 5.7: The real part of the FRF

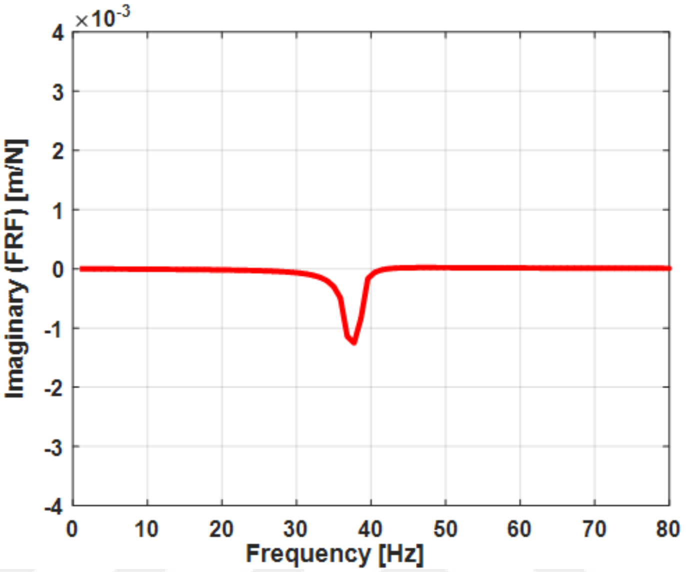

Figure 5.8: The imaginary part of the FRF

The corresponding magnitude and the phase of the passive magnetic bearing radial FRF is as shown in Figure 5.9 and Figure 5.10 respectively.

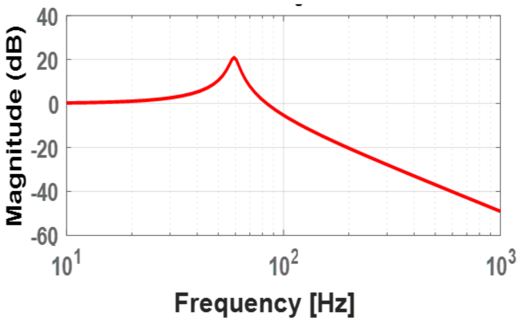

Figure 5.9: The magnitude of the FRF

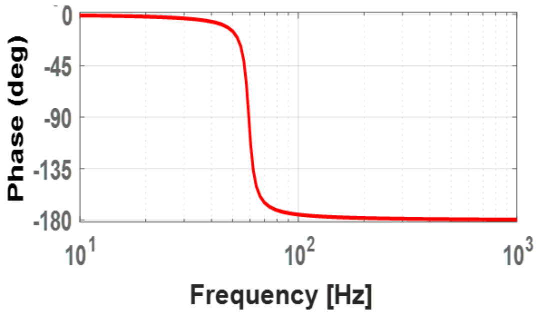

Figure 5.10: The phase of the FRF

The proposed controller is experimentally implemented using the National Instruments (NI) PCIe-6351 data acquisition system with the Simulink xPC Target. For acquiring the data, NI USB-6259 card having analog input of 16 bits is used.

The sampling frequency of 10 kHz is used. In order to drive the electromagnets, a power amplifier circuit is designed. The frequency of the PWM signals is 20 kHz. The bias current used is 2 A.

The experimental result of initial startup of the bearing and the corresponding currents in the two electromagnets are shown in Figure 5.11 and Figure 5.12 respectively. The functions f_{zl} and g_{zl} are measured experimentally and the resulting plots are shown in Figure 5.13 and Figure 5.14 respectively.

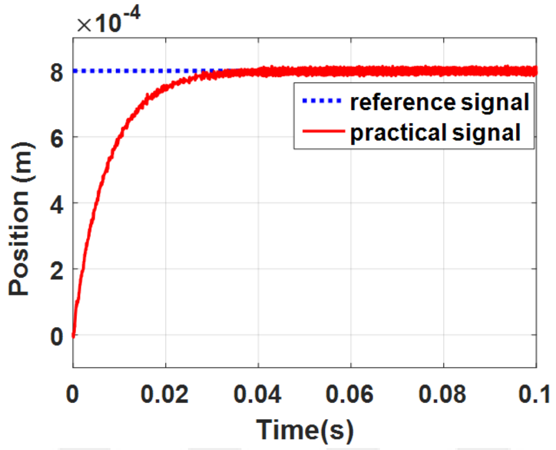

Figure 5.11: The initial startup response of the controller for the active magnetic bearing

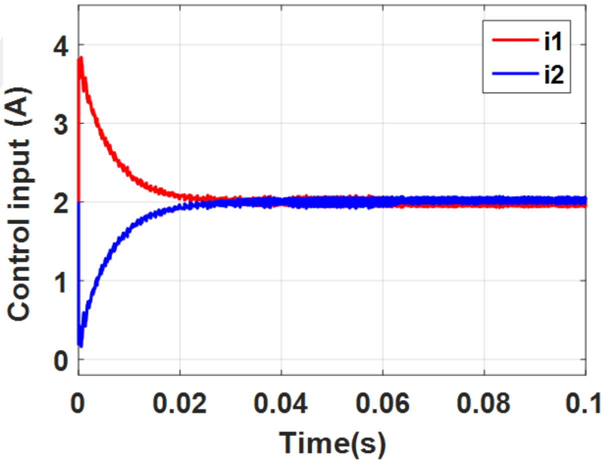

Figure 5.12: The currents in the two electromagnets

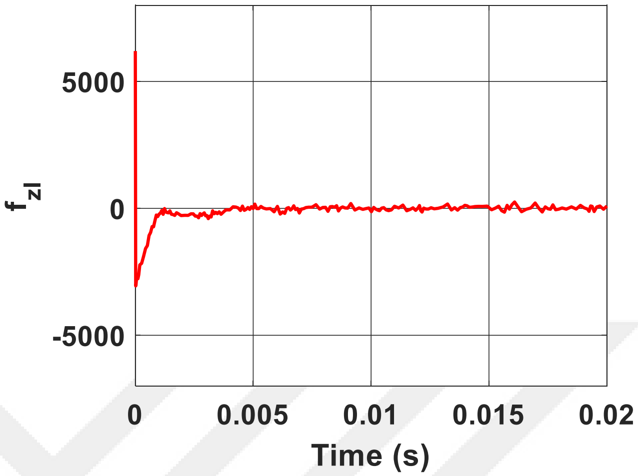

Figure 5.13: Measured f_{zl} function

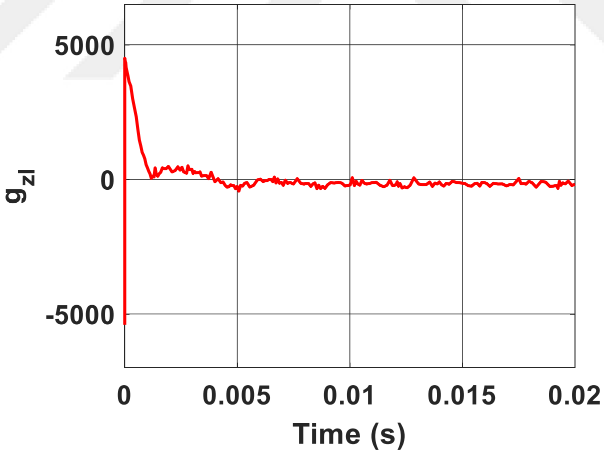

Figure 5.14: Measured g_{zl} function

A step disturbing interference of 5.18 N is added to the system at time 2 secs. The resulting output displacement of the shaft and the corresponding currents in the two I-core electromagnets are as shown in Figure 5.15 and Figure 5.16 respectively.

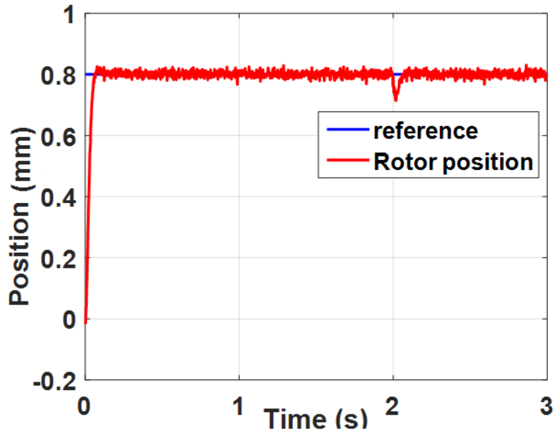

Figure 5.15: Output displacement of the shaft as a result of applying a disturbance of 5.18 N at time 2 secs

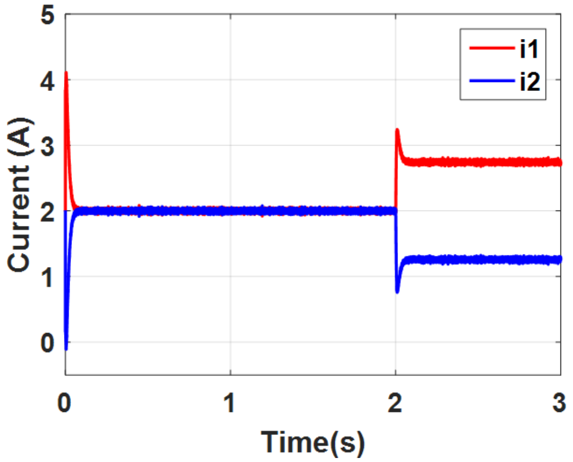

Figure 5.16: The corresponding currents in the two electromagnets after application of the disturbance force at time 2 secs

The shaft is rotated with the speed of 1890 rpm (31.5 Hz) using the single phase brushless DC motor designed for the hybrid magnetic bearing. There are two critical frequencies of the rotor, 47.5 Hz and 51 Hz which are much larger than the operating speed of 1890 rpm (31.5 Hz). The Keyence laser sensor is used for the experimental measurement of the shaft oscillations while rotating. Figure 5.17 shows the radial oscillations and Figure 5.18 shows the axial oscillations of the shaft while rotating at 1890 rpm.

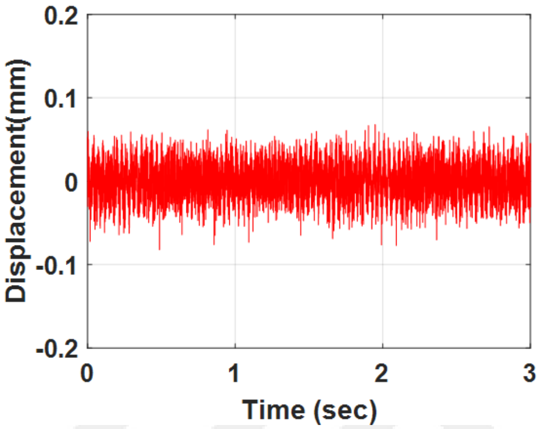

Figure 5.17: Radial oscillations of the shaft while rotating at 1890 rpm

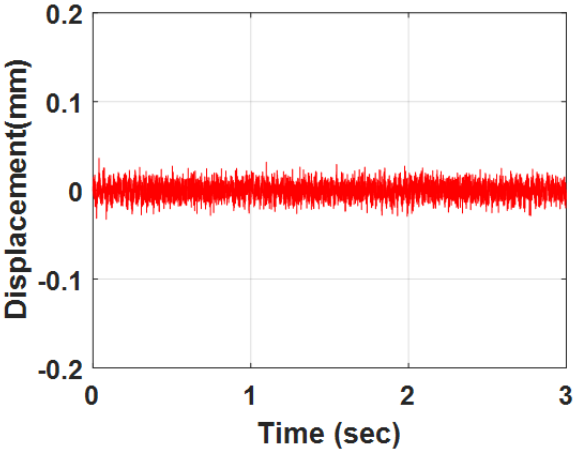

Figure 5.18: Axial oscillations of the shaft while rotating at 1890 rpm

The average peak oscillations in the radial direction are 0.45 mm and in the axial direction 0.19 mm. The magnitude frequency spectrum of the radial and axial oscillations are shown in Figure 5.19 and Figure 5.20 respectively.

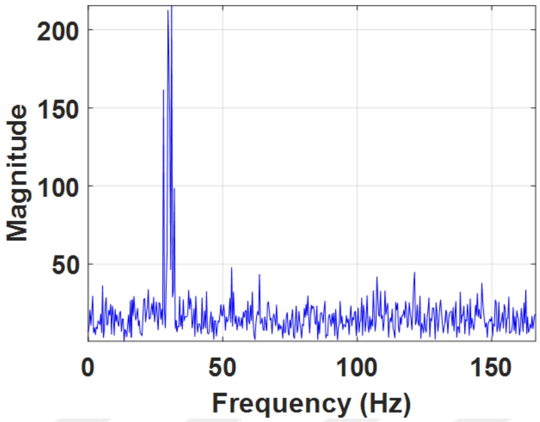

Figure 5.19: Magnitude spectrum of radial oscillations while the shaft rotates at 1890 rpm

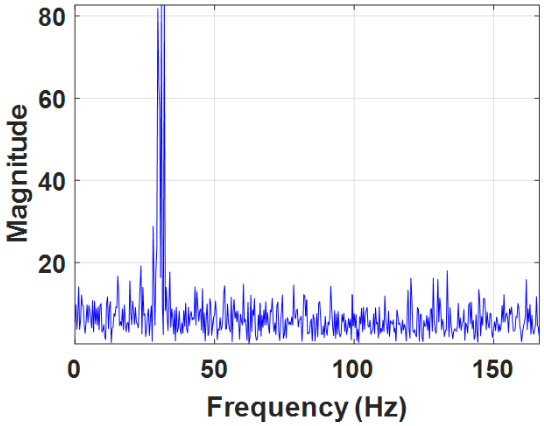

Figure 5.20: Magnitude spectrum of axial oscillations while the shaft rotates at 1890 rpm

5.4 Summary

In this chapter, the experimental setup of the designed hybrid magnetic bearing prototype is provided. The magnetic forces, damping, stiffness, and magnetic flux densities of the experimental prototype are experimentally measured and compared with the simulated results. The comparison of the experimental and simulated results showed good agreement. The designed adaptive controller is implemented on the experimental prototype and the performance of the controller is obtained at different conditions. The shaft is rotated at the desired speed and the oscillations of the shaft are measured. The designed controller showed good robustness against the external acting disturbances and a good set speed for the axial position control of the hybrid magnetic bearing prototype setup.

Chapter 6

DESIGN OF THE NOVEL BEARINGLESS MOTOR FOR MINIATURE AXIAL FLOW BLOOD PUMP

6.1 Introduction

In this chapter, a novel design of the bearingless motor is presented for the miniature axial flow blood pump. The radial position of the rotor is measured with the help of linear Hall Effect sensors. The angular position of the rotor is measured with digital Hall Effect sensors.

The optimization of the impeller for the blood pump is done based on the computational fluid dynamics. Based on the optimization, an enclosed impeller design is selected and the length of the impeller is shortened as compared to the conventional axial flow pumps rotors. Because of the shorter rotor length, only one bearingless motor is needed for the operation of the pump.

In conventional bearingless motors, eddy current sensors are used for measuring the radial position of the rotor. Due the miniaturized size of the pump, eddy current sensors cannot be used in this configuration. Therefore, a sensor assembly based on the linear Hall Effect sensors is proposed in order to measure the rotor radial position. The finite element analysis of the overall magnetic circuit is performed and then experimentally verified in order to get the stiffness, magnetic forces, currents, number of turns and magnetic flux densities on the rotor, in the airgap and on the stator surface. The radial position measurement assembly is verified experimentally. Experimental setup is manufactured in order to verify the design process and the performance of the proposed controller is obtained using different testing conditions.

6.2 Mechanical Design

The proposed rotor design for the novel bearingless motor is shown in Figure 6.1. The rotor has a permanent magnet m_p installed on the back side in order to measure the rotor radial position. Another permanent magnet M_b is installed on the rotor for producing the radial suspension forces and torque.

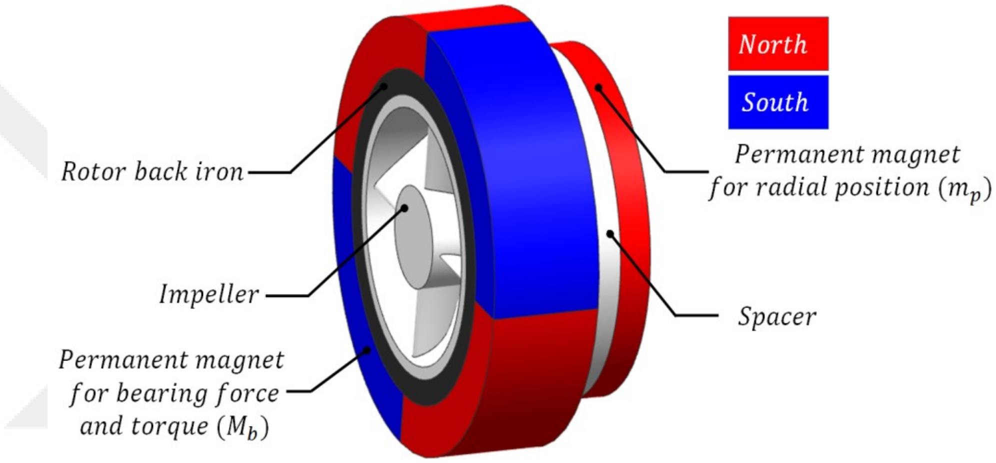

Figure 6.1: Mechanical design of the proposed rotor for the novel bearingless motor

Additionally, the rotor consists of the back iron, an impeller and a spacing which is placed between the two permanent magnet so that to minimize the cross talk between the two permanent magnets. Neodymium Iron Boron (NdFeB) based N48 grade permanent magnets in arc shape are utilized in the rotor of the novel bearingless motor. The rotor schematic diagram is provided in Figure 6.2 and Table 6.1 provides the different dimensions of the various parts of the rotor. The number of permanent magnets installed for producing the torque and bearing forces is four and they are magnetized diametrically. The permanent magnet used for measuring the radial position is magnetized radially. Four linear Hall Effect sensors are mounted on the stator assembly in order to measure the rotor radial position. Two Hall Effect sensors are mounted on the stator assembly for measuring the angular position of the rotor.

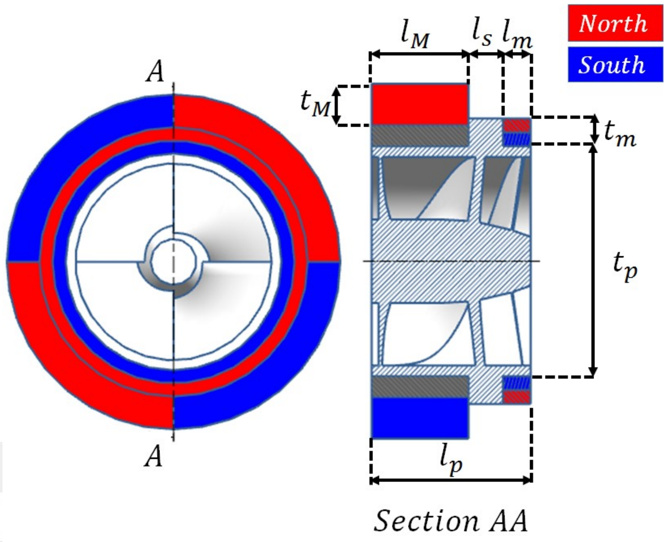

Figure 6.2: The schematic view of the proposed novel design of the rotor

Four blades of the impeller are designed in a symmetrical manner so that the blade configuration does not affect the motor operation in the radial direction and in the axial direction by producing the thrust forces and lift forces as disturbance forces. Because of the symmetrical blade structure, the overall rotor is affected equally by the flow of the fluid through the pump blades and hence no lift is produced. Figure 6.3 shows the schematic view of the impeller, diffuser and the inducer for the proposed design of the axial flow bearingless pump.

Table 6.1: The parametric values of the different sections of the pump

Parameter	Value
Impeller blades axial length, l_p	12.5 mm
Impeller blades thickness, t_p	15.5 mm
The torque and bearing forces permanent magnet axial thickness, l_M	7 mm

The bearing and torque permanent magnet thickness, t_M	3 mm
The length of the radial position permanent magnet in the axial direction, l_m	2.5 mm
The bearing forces and torque permanent magnet thickness, t_m	2.5 mm
Spacer length, l_s	3 mm
Rotor outer radius	14 mm
Stator outer radius	35 mm

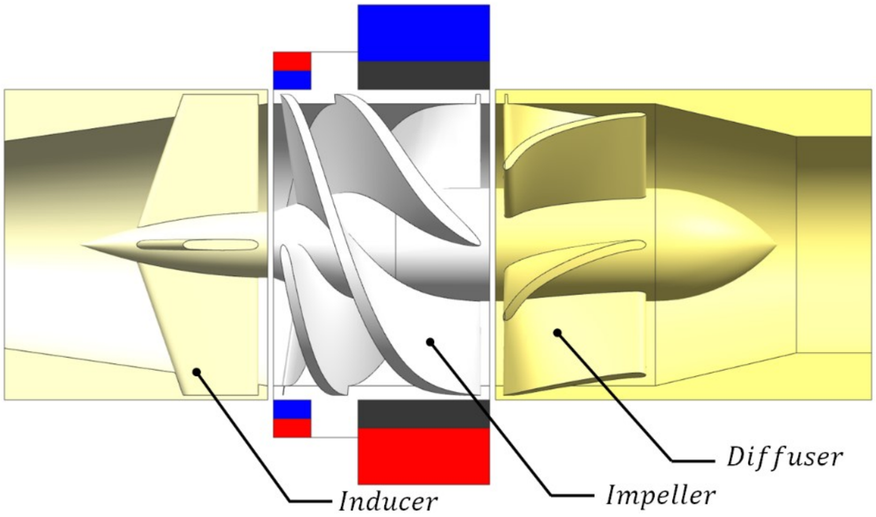

Figure 6.3: Diffuser, inducer and impeller of the proposed pump

There are two windings wound on each of the stator leg. One winding set is used for the generation of torque for the motor and another winding set is used for the generation of bearing forces in the radial direction for the levitating rotor. Figure 6.4 shows the rotor and stator assembly and Figure 6.5 shows the overall pump assembly for the proposed axial pump.

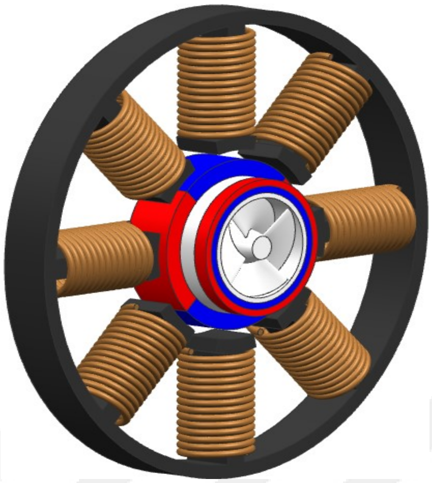

Figure 6.4: Rotor and stator assembly

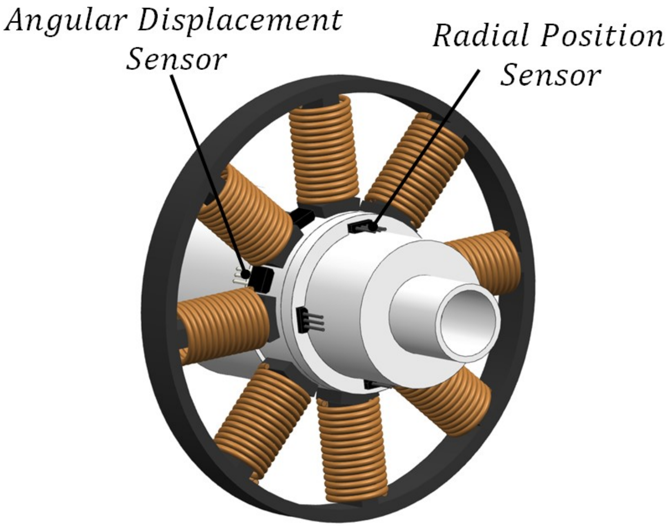

Figure 6.5: Overall assembly of the pump

6.3 Generation of Radial Suspension Forces and Motoring Torque

Passive reluctance forces are utilized in the axial direction in order to stabilize the rotor in the tilt direction and in the axial direction. Figure 6.6 shows the passive reluctance forces exerted on the shaft in order to stabilize it in the tilt and in the axial direction.

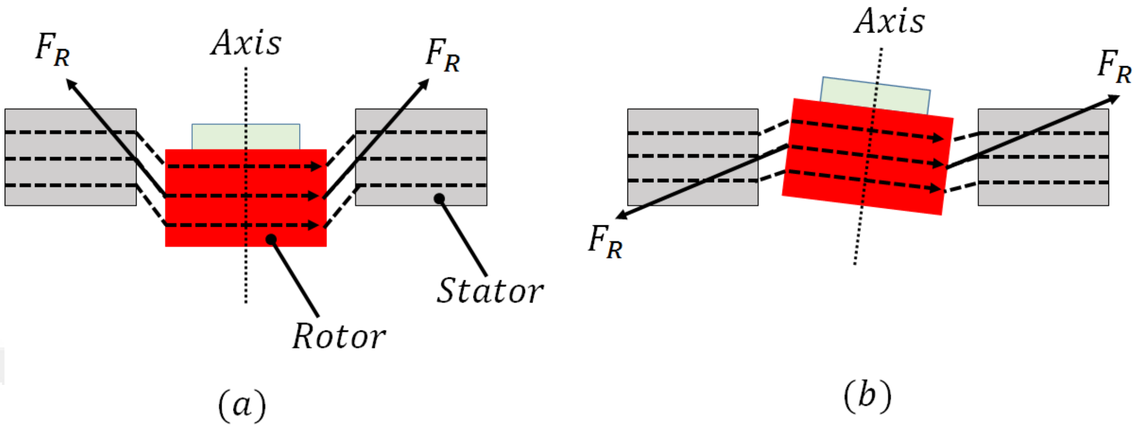

(a) (b)

Figure 6.6: (a) Axial direction stabilization using the reluctance forces (b) Tilt direction stabilization using the reluctance forces

There are two different windings wound on the stator legs. One winding is used for the generation of levitating forces for the rotor and another winding is used for the generation of the motoring torque. One set of winding $a\acute{a}$, $b\acute{b}$ $c\acute{c}$, and $d\acute{d}$ is used by the motor in order to generate the motoring torque. Another set of winding $A\acute{A}$, $B\acute{B}$ $C\acute{C}$, and $D\acute{D}$ is utilized by the bearingless motor in order to generate the radial suspension forces. These two sets of windings are switched in alternate manner for the proper operation of the bearingless motor in one electrical rotation of the rotor. For generating the bearing forces, two pole winding is used. For the generation of the motoring torque, a four pole winding is used. The principle of the generating the torque is showed in Figure 6.7. The angular position of the rotor is measured using the two digital Hall Effect sensors H_1 and H_2. The coils $b\acute{b}$ and $d\acute{d}$ are used for generating the motoring torque when the rotor is in a position as shown in Figure 6.7. The windings $A\acute{A}$ and $C\acute{C}$ are utilized for the generation of the radial bearing forces.

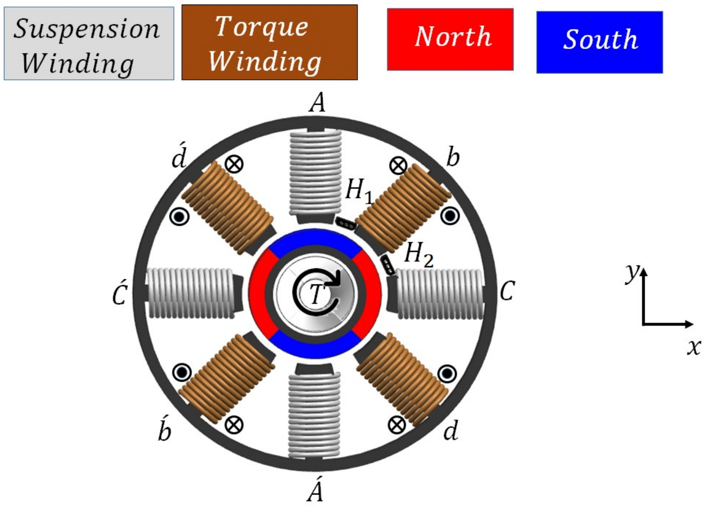

Figure 6.7: Generation of the motoring torque with b and d coils

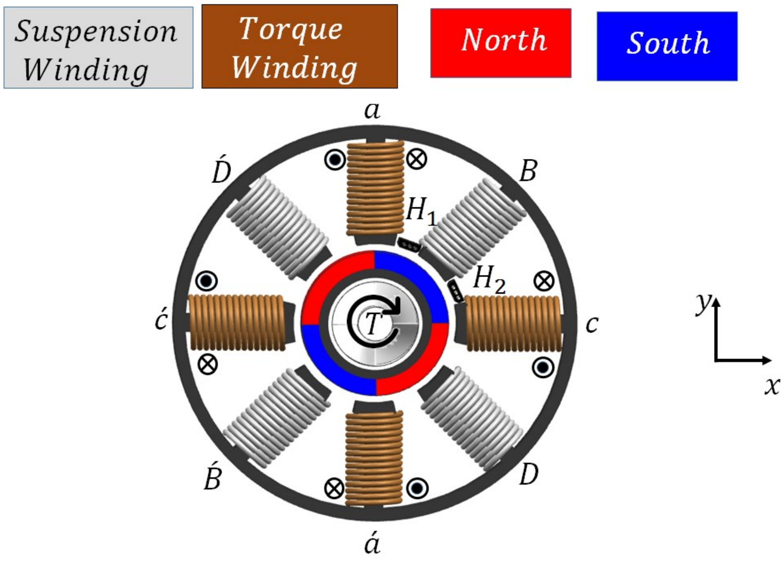

Figure 6.8: Generation of motoring torque with a and c coils

When the rotor is in a position as shown in Figure 6.8, then the windings $a\acute{a}$ and $c\acute{c}$ are used for the generation of the motoring torque and the windings $B\acute{B}$ and $D\acute{D}$ are utilized for the generation of the radial bearing forces. For the generation of the bearing forces in the x direction, the application of current is made in the coils $C\acute{C}$ as shown in Figure 6.9 and for generating in the y direction, the application of current is made in the coils $A\acute{A}$ as shown in Figure 6.10.

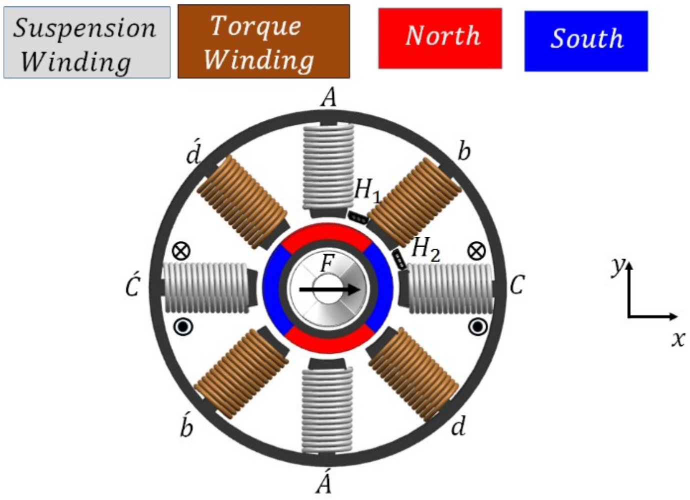

Figure 6.9: Application of current in the winding C for the x direction force generation

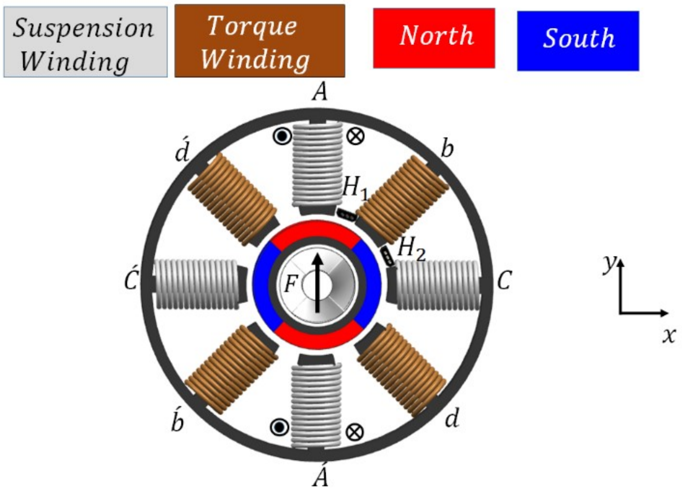

Figure 6.10: Application of current in the winding A for the y direction force generation

For the purpose of generating the radial bearing forces in the x and y direction, when the coils $B\acute{B}$ and $D\acute{D}$ are used, the current is excited through both the windings. Figure 6.11 shows the direction of current when the radial bearing force is generated in the x direction and the coil windings $B\acute{B}$ and $D\acute{D}$ are used.

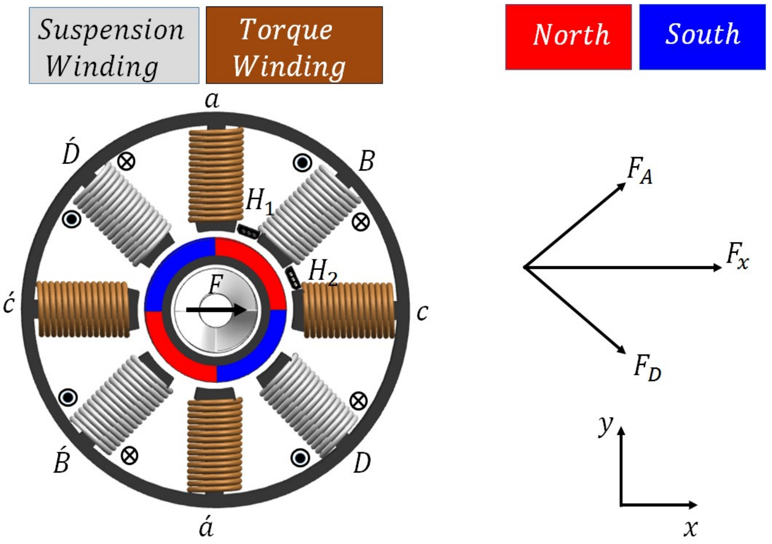

Figure 6.11: Direction of current in windings $B\acute{B}$ and $D\acute{D}$ for generating the radial force in the x direction

Based upon the values obtained from the digital Hall Effect sensors, the windings between the motoring torque $a\acute{a}$, $b\acute{b}$, $c\acute{c}$, and $d\acute{d}$ and the radial bearing force $A\acute{A}$, $B\acute{B}$ $C\acute{C}$, and $D\acute{D}$ is chosen as shown in the Table 6.2. The digital Hall Effect sensors utilized here give a logic 1 when the north pole of the magnet comes closer to the sensor and a logic 0 when the south pole of the magnet comes closer to the sensor surface.

Table 6.2: The selection between the radial suspension windings and motoring torque windings

Rotor Position	Suspension Windings	Torque Windings
$H_1 = 0$, and $H_2 = 0$	$B\acute{B}$ and $D\acute{D}$	$a\acute{a}$ and $c\acute{c}$
$H_1 = 0$, and $H_2 = 1$	$A\acute{A}$ and $C\acute{C}$	$b\acute{b}$ and $d\acute{d}$
$H_1 = 1$, and $H_2 = 0$	$A\acute{A}$ and $C\acute{C}$	$b\acute{b}$ and $d\acute{d}$
$H_1 = 1$, and $H_2 = 1$	$B\acute{B}$ and $D\acute{D}$	$a\acute{a}$ and $c\acute{c}$

6.4 Analytical Modeling

6.4.1 Dynamic Model of the Rotor

The various forces acting on the rotor are shown in the Figure 6.12. The rotor is placed vertically for the analysis. The two coordinates systems are also shown in Figure 6.12. The stator iron exerts the reluctance forces on the rotor which are represented by the forces F_{mx}, F_{my}, and F_{mz} in the diagram and the electromagnetic forces are represented by F_{ex}, F_{ey}, and F_{ez} in the diagram. The center of the reluctance forces is c_M while c_m represents the rotor mass center. There is a distance of l_c between the two centers c_M and c_m as shown in Figure 6.13. The dynamic equation of the rotor along the x-axis is given as follows:

$$m\ddot{x} + d\dot{x} + cx + F_{mx} = F_{ex}$$

$$I_x\ddot{\theta}_x + I_z\omega_m\dot{\theta}_y + d\dot{\theta}_x = F_{ldx}z + mgl_c$$

where the mass moment of inertia is denoted by I_x and I_z about the axis θ_x and θ_z. ω_m is the angular velocity of the rotor system about z-axis. The damping coefficient is given by d and the coefficient of stiffness is given by c. The effect of the lift due to the blades of the rotor is eliminated due to the symmetrical shape of the blades for the axial flow pump. Therefore, the term $F_{ldx}z$ vanishes from the analysis.

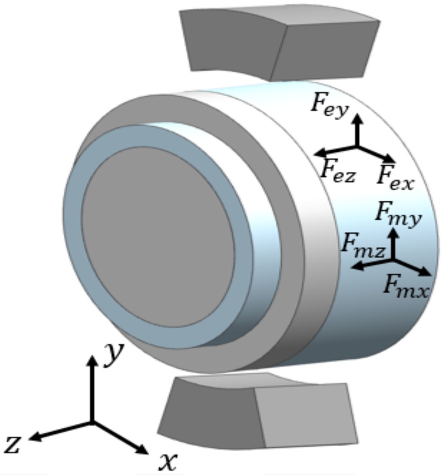

Figure 6.12: The different forces acting on the levitating rotor and their coordinate systems

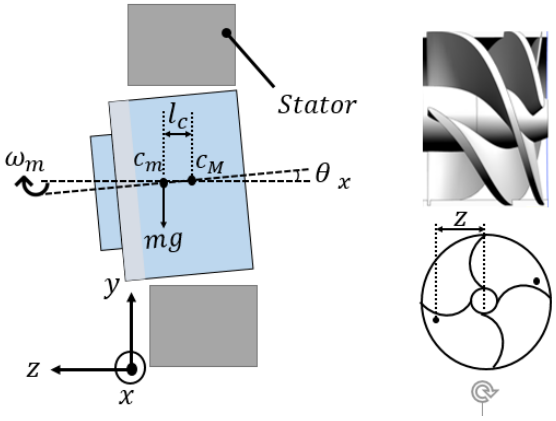

Figure 6.13: The 2-dimensional view of the rotor forces schematic

Similarly, the dynamics about the y-axis are provided as follows:

$$m\ddot{y} + d\dot{y} + cy + F_{my} = F_{ey}$$

$$I_y\ddot{\theta}_y - I_z\omega_m\dot{\theta}_x + d\dot{\theta}_y = F_{ldy}z$$

where the mass moment of inertia is denoted by I_y and I_z about the axis θ_y and θ_z. ω_m is the angular velocity of the rotor system about z-axis. The damping coefficient is given by d and the coefficient of stiffness is given by c. The effect of the lift due to the blades of the rotor is eliminated due to the symmetrical shape of the blades for the axial flow pump. Therefore, the term $F_{ldy}z$ vanishes from the analysis.

The analysis of the dynamics around z-axis is given as below:

$$m\ddot{z} + d\dot{z} = F_{mz} - F_l$$

where F_l is the lift force acting on rotor due to the fluid flowing through the blades of the impeller. The force F_{mz} is used to keep the rotor in stabilized form in the axial direction and is the reluctance force between the stator iron and it should be greater than the lift force F_l.

6.4.2 Mathematical Model of the Radial Bearing Force

The current is passed in a direction as shown in Figure 6.14 through the windings of the bearingless motor in order to produce a bearing force in the positive x-axis direction. There are two type of forces acting on the rotor of the proposed motor. One force is the Maxwell component dF_r also known as the radial component of the force. Another component is the tangential component of the force dF_t. The current passing through the bearing force windings control the radial component force and is given as follows:

$$dF_r = \frac{\left(B_{pm}(\theta) + \Delta B_{wdg}(\theta)\right)^2 r l_m}{2\mu_0} d\theta$$

where the airgap magnetic flux density due to the currents in the bearing windings is given by $\Delta B_{wdg}(\theta)$ and the magnetic flux density in the airgap present due to the rotor permanent magnets is given by $B_{pm}(\theta)$, θ is representing the mechanical angle of the rotor, r is the inner radius of the stator and l_m represents the axial thickness of the rotor.

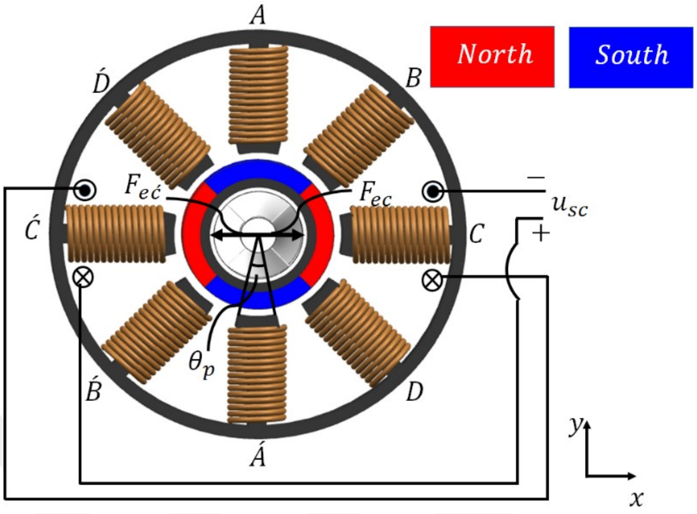

Figure 6.14: The direction of current in the suspension windings in order to produce the bearing force in the positive x direction

The tangential component of the force dF_t is given as follows:

$$dF_t = i_{wdg}.(B_{pm}(\theta).dl_{wdg})$$

where the winding current is given by i_{wdg}, $B_{pm}(\theta)$ represents the magnetic flux density in the airgap present due to the rotor permanent magnets and the term dl_{wdg} represents the magnetic field region's winding length part. The net torque is generated for the rotor in the counterclockwise or clockwise direction with the proper currents in the windings producing proper tangential force components.

The pull on the rotor in the positive x direction, when the rotor is displaced along the positive x direction is given as follows:

$$F_{mc} = \frac{2AI_M^2 t_M^2 B_r^2}{(x_g + t_M)^3 \mu_0} x$$

where the permanent magnet thickness is given as t_M, the airgap between the stator and the rotor is denoted by x_g, the equivalent current of the permanent magnet is represented by I_M, the remanent magnetic flux density is denoted by B_r, the rotor pole face area is given by A

and the relative permeability of vacuum is given by μ_0. The total x axis magnetic pull is given as follows:

$$F_{mx} = \frac{2AI_M^2 t_M^2 B_r^2}{(x_g + t_M)^3 \mu_0}(2cos^2 45^0 + 1)x$$

$$F_{mx} = \frac{4AI_M^2 t_M^2 B_r^2}{(x_g + t_M)^3 \mu_0}x$$

This is the amount of total force which is exerted on the rotor by the stator legs B, C and D. The electromagnetic force which acts on the rotor due to the windings currents in the leg C is given as follows:

$$F_{ec} = \frac{A\mu_0 \left(i_c + \frac{I_M}{N}\right)^2 N^2}{2(x_g + t_M)^2}$$

The force acting on the rotor due to the leg $\acute{C}$ is given as follows:

$$F_{ec} = \frac{A\mu_0 \left(-i_c + \frac{I_M}{N}\right)^2 N^2}{2(x_g + t_M)^2}$$

The net electromagnetic force which acts on the rotor is given as follows:

$$F_{ex} = i_c . \left(\frac{2I_M \mu_{0N} A}{(x_g + t_M)^2}\right)$$

The overall bearing force in the radial direction is calculated as below:

$$F_x = F_{mx} + F_{ex} = \frac{4AI_M^2 t_M^2 B_r^2}{(x_g+t_M)^3 \mu_0}x + i_c . \left(\frac{2I_M \mu_{0N} A}{(x_g+t_M)^2}\right)$$

The force along the y direction is calculated as follows:

$$F_y = F_{my} + F_{ey} = \frac{4AI_M^2 t_M^2 B_r^2}{(y_g+t_M)^3 \mu_0}y + i_c . \left(\frac{2I_M \mu_{0N} A}{(y_g+t_M)^2}\right)$$

6.5 Finite Element Analysis of the Bearingless Motor System

The finite element analysis of the overall bearingless motor is performed. The magnetic flux densities of the stator, rotor and airgap are calculated. The sensor assembly is verified for measuring the radial displacement of the motor. The computational fluid dynamics of the pump system is performed in order to see the pressure and flow rate of the pump system. For minimizing the interference between the two permanent magnets, a spacer is put between them. The four Hall effect sensors are shown in Figure 6.15.

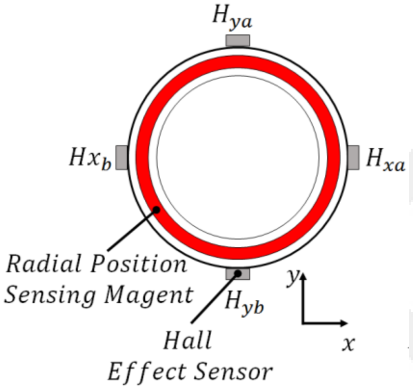

Figure 6.15: The hall effect sensor assembly for measuring the radial position of the rotor

The magnetic flux distribution across the surface of the rotor is shown in Figure 6.16.

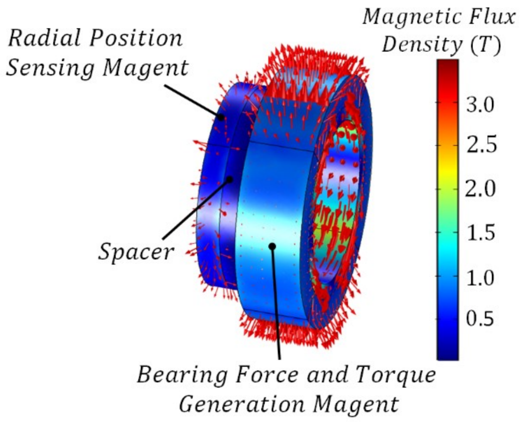

Figure 6.16: Norm of the magnetic flux density across the rotor surface

The spacer length is varied from 1 mm to 4 mm and a 3 mm spacer length is found to be optimal in order to reduce the cross talk as well not offering too much to the axial length of the rotor. There is a minimum cross talk between the two permanent magnets as shown in Figure 6.16. The magnetic flux density of the two opposite Hall sensors denoted by H_{xa} and H_{xb} is shown in Figure 6.17 when the rotor magnet is moved from 0 mm to 0.75 mm in the radial x direction. As shown in the Figure 6.17, there is a linear relationship between the distance of the rotor and the magnetic flux density as seen by the Hall sensors. Therefore, based on the Figure 6.17, the radial displacement covered by the rotor can be calculated as follows;

$$x = \left(-B_{H_{xb}} + B_{H_{xa}}\right).\frac{1}{h}$$

$$y = \left(-B_{H_{yb}} + B_{H_{ya}}\right).\frac{1}{h}$$

where h represents the slope of the radial direction displacement covered by the rotor.

Hence, this sensor assembly can measure the rotor radial displacement with a good accuracy, given that the radial permanent magnet is precisely manufactured having uniform magnetic flux density distribution.

The rotor is displaced in the radial direction from the center position to one end of the stator, where it touches the stator surface and the reluctance force is measure using the finite element method. Figure 6.18 shows the force vs the radial displacement of the rotor. The maximum force of 21.5 N is exerted on the rotor when it touches the stator surface along the x direction. Hence, this is the overall maximum amount of force which the stator bearing windings have to exert in order to bring back the rotor to the center equilibrium position.

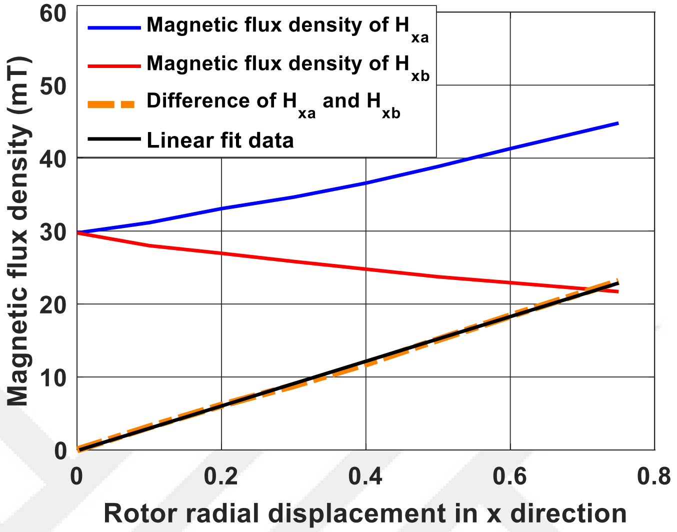

Figure 6.17: The radial displacement of the rotor vs the magnetic flux density

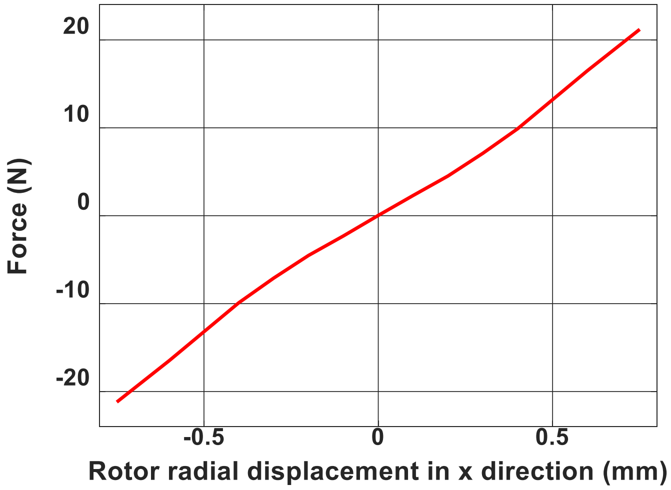

Figure 6.18: Reluctance force on the rotor vs the radial displacement

Similarly, Figure 6.19, shows the force on rotor when it is displaced in the axial direction and the axial stiffness is calculated to be 5.1 N/mm.

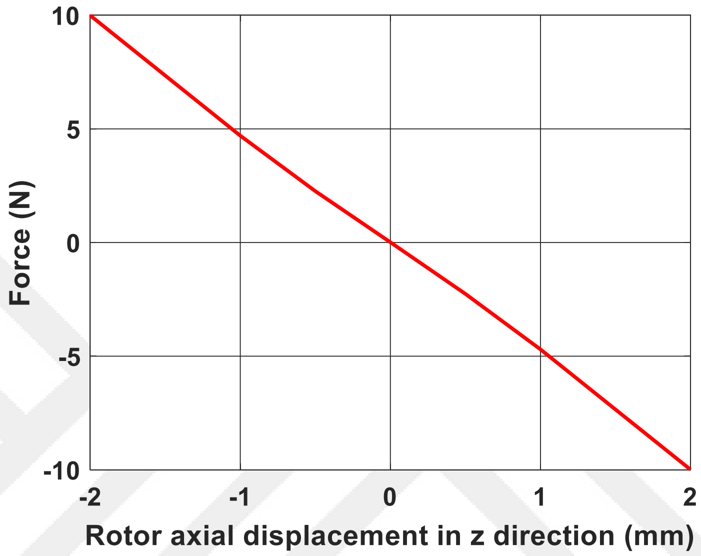

Figure 6.19: Reluctance force on rotor vs the axial displacement of rotor in z direction

The norm of magnetic flux density across the rotor and the stator surface is shown in Fig. 6.20.

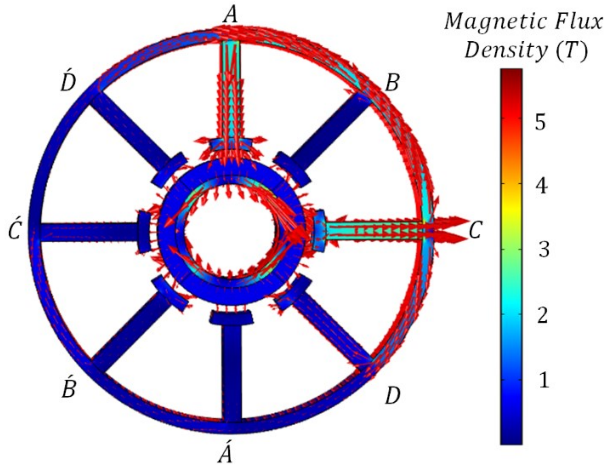

Figure 6.20: Norm of magnetic flux density across the surface of the rotor and the stator

The variation of the radial direction bearing force with respect to the radial bearing forces is as shown in Figure 6.21. The variation of the motoring torque with respect to the current in the motoring torque windings is shown in Figure 6.22. For seeing the decoupling characteristics of the two sets of windings, the radial bearing force variation is calculated with respect to the current variation in the motoring torque windings and the variation of the motoring torque with respect to the current change in the radial bearing force windings. Figure 6.23 and Figure 6.24 shows the corresponding plots for the two cases. It is obvious from these two figures that a good decoupling exists between the radial bearing force windings and the motoring torque windings and they minimally affect each other operation.

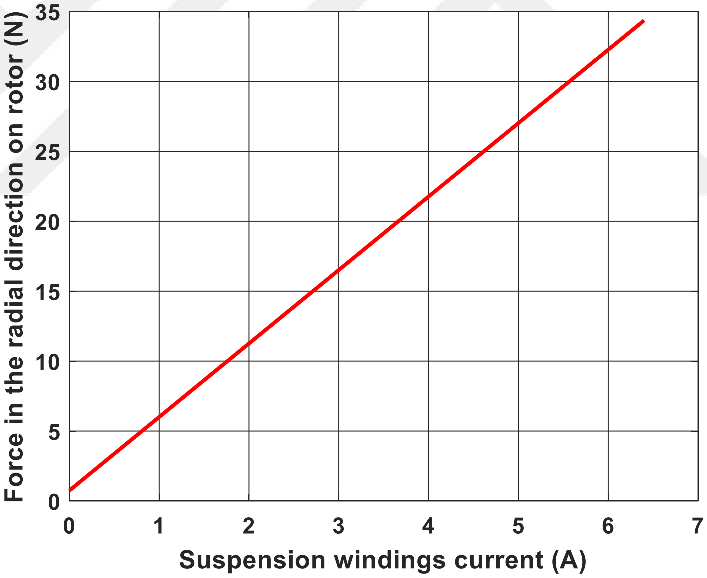

Figure 6.21: Radial bearing force on the rotor vs the current in the bearing windings

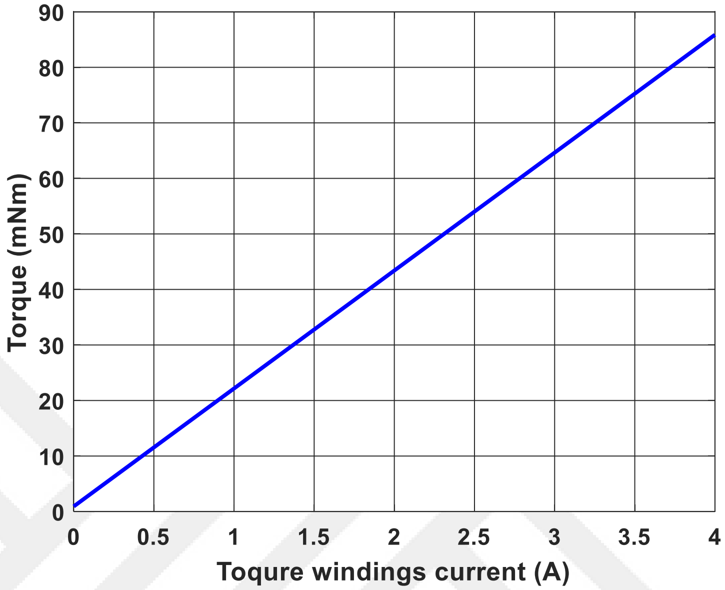

Figure 6.22: Motoring torque of the rotor vs current in the torque windings

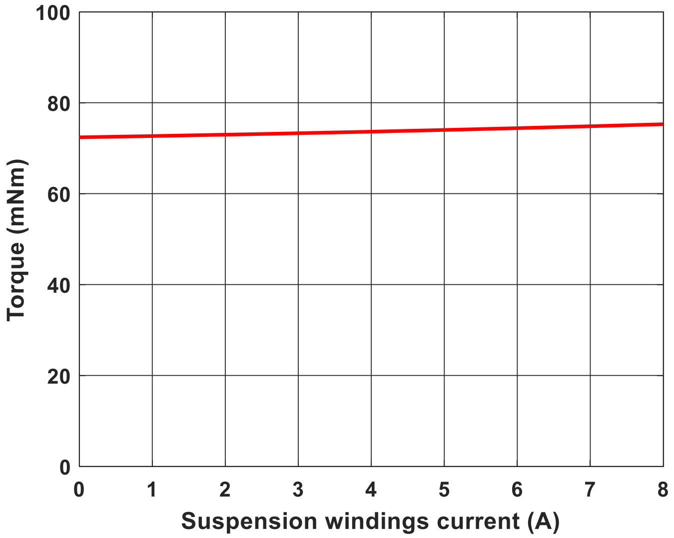

Figure 6.23: Variation of motoring torque with respect to the current change in the radial bearing force windings

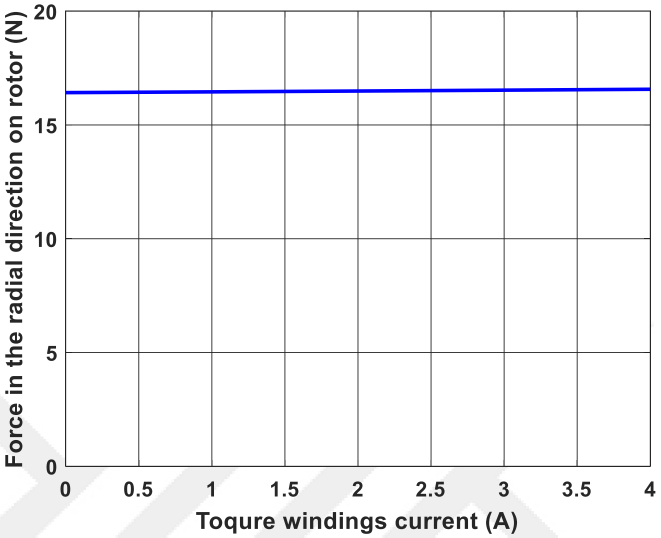

Figure 6.24: Variation of the radial bearing force with respect to the current change in the motoring torque windings

The computational fluid dynamic analysis of the rotor is performed using finite element method. The rotor is rotated at 10000 rpm and the pressure, flow rate and shear stresses are calculated on the rotor. Figure 6.25 shows the velocity streamline of the pump and Figure 6.26 shows the pressure distribution across the rotor various parts while rotating at 10000 rpm.

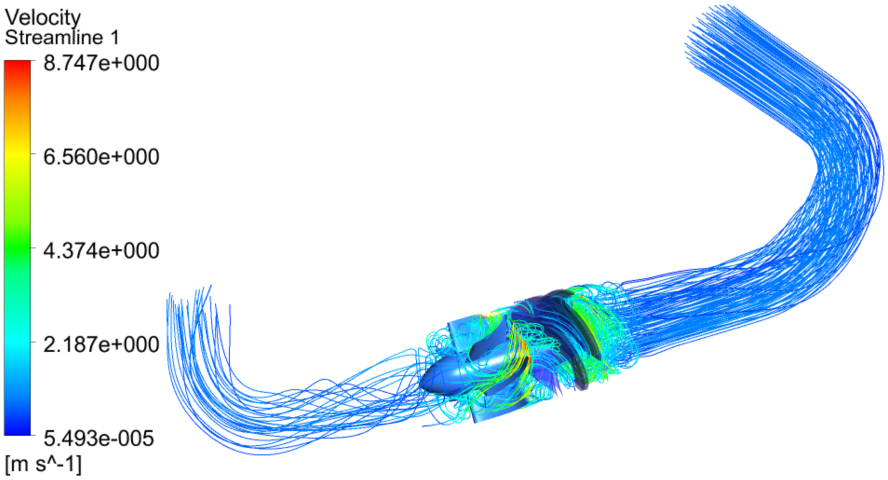

Figure 6.25: Velocity profile of the pump at 10000 rpm

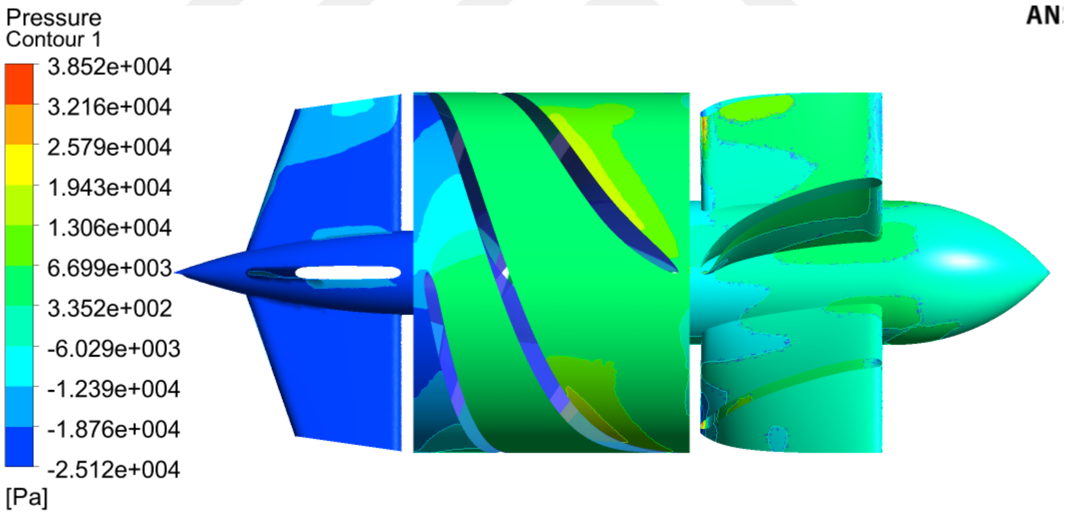

Figure 6.26: Pressure distribution across the rotor, inducer and diffuser parts

The uplift force maximum value comes to be 2.72 N, which the fluid exerts on the rotor while rotating. This force is less than the axial stiffness of the rotor which 5.1 N/mm. At a speed of 10000 rpm, the flow rate of 5 L/min and a 112 mm Hg pressure is obtained. Hence a minimum of 0.55 mm clearance is at least needed between the impeller and inducer. Figure

6.27 shows the velocity vectors and Figure 6.28 shows the shear stresses on various parts of the pump while rotating at 10000 rpm.

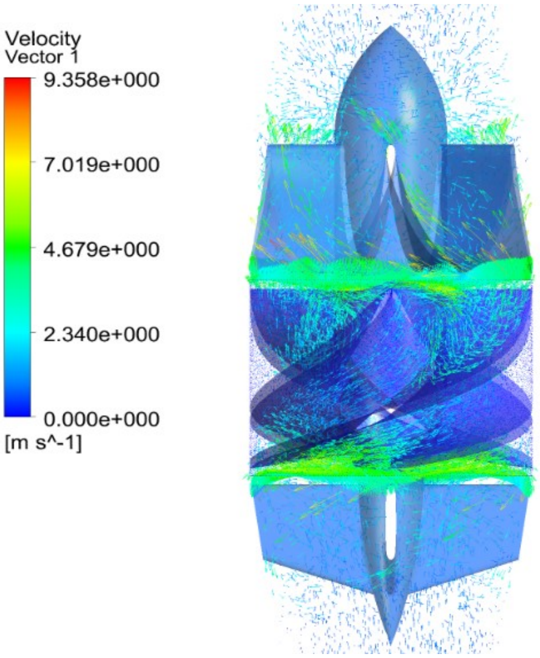

Figure 6.27: The corresponding velocity vectors of rotor while rotating at 10000 rpm

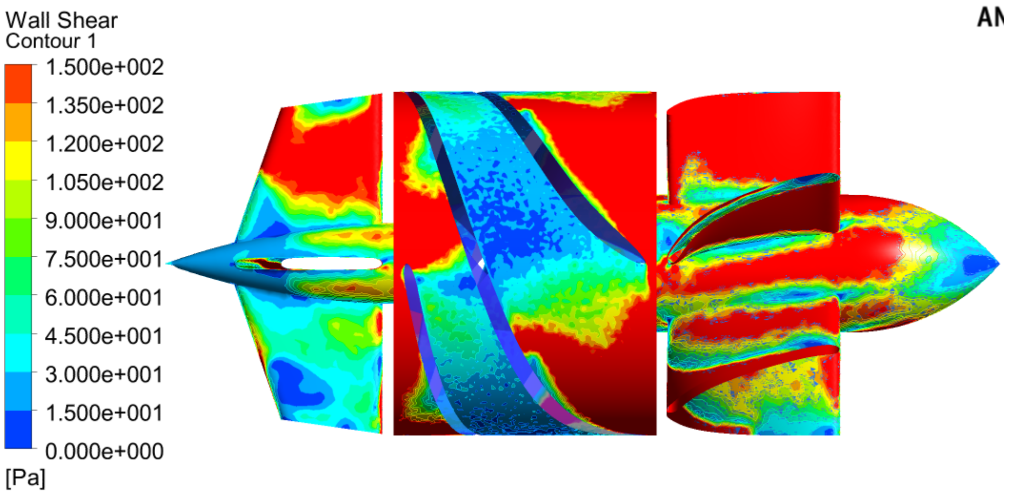

Figure 6.28: Shear stress profile of the rotor with the corresponding operating speed

6.6 Experimental Setup and Results

For verifying the design process of the novel bearingless motor, a prototype setup is manufactured. The prototype consists of a rotor with 4 poles and stator with 8 poles. The experimental prototype setup is shown in Figure 6.29 and Figure 6.30 shows the rotor system.

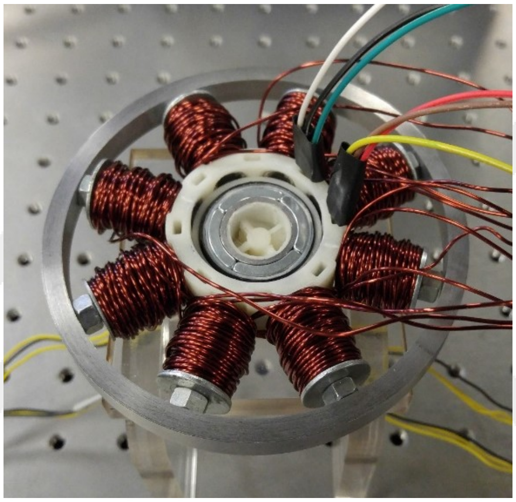

Figure 6.29: The experimental setup of the novel bearingless motor system

Figure 6.30: The different views of the designed rotor system

Two digital Hall effect sensors are utilized for measuring the angular position of the rotor. Four linear Hall effect sensors are utilized in order to measure the radial displacement made by the rotor while levitating. A 15.5 mm diameter impeller is used. The outer radius of the rotor is 14 mm and the outer radius of the stator part is 35 mm. The thickness of the permanent magnet used for the bearing forces and the motoring torque is 3 mm. The thickness of the radially magnetized magnet for sensing the radial distance is 2.5 mm. The airgap along the radial direction between the rotor and the stator assembly is 0.75 mm. N48 grade permanent magnets coated with Zinc are utilized for the rotor. The rotor is 12.5 mm long in the axial direction. The copper wire of 18 gauge is utilized for the windings of the stator. The number of coil windings for the radial bearing force is 80 and for the motoring torque is 40. Linear Hall sensors A1324 are used for the prototype setup with sensitivity of 5 mV/Gauss and having a 17 kHz of bandwidth. Figure 6.31 shows the experimental results of magnetic flux with respect to the rotor displacement along radial direction.

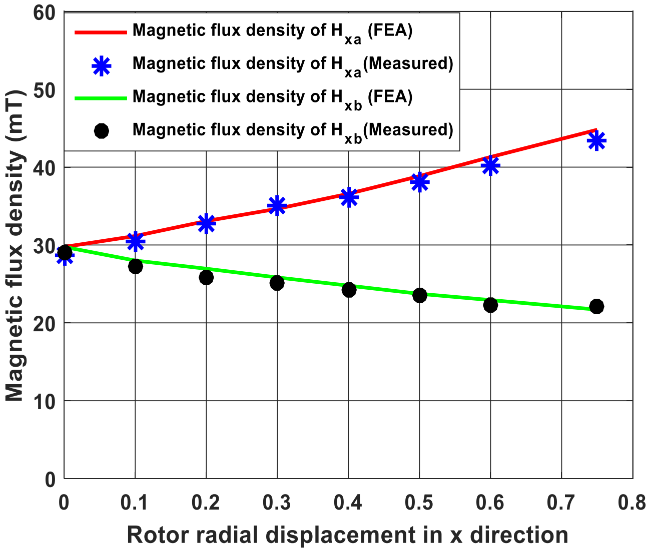

Figure 6.31: The experimental result of Hall effect output magnetic flux vs the rotor displacement in the radial direction

The different forces acting on the rotor and the stiffness are measured using the Kistler dynamometer as shown in Figure 6.32.

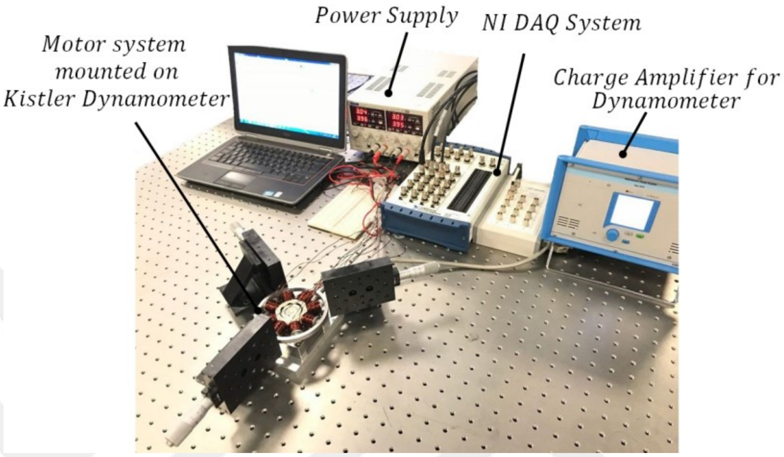

Figure 6.32: Experimental setup used for the measurement of the radial forces, axial forces and stiffness of the rotor system

Figure 6.33 shows the experimental and simulated force on the rotor in the x direction and y direction when the current is passed through the coils $C\acute{C}$ only.

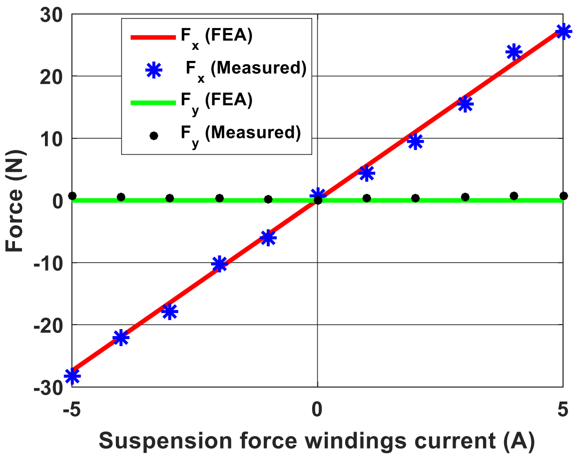

Figure 6.33: The forces exerted on the rotor in the x direction and y direction with only the $C\acute{C}$ coil excited

Figure 6.34 shows the forces on the rotor in the radial direction when the bearing winding $A\acute{A}$ is excited.

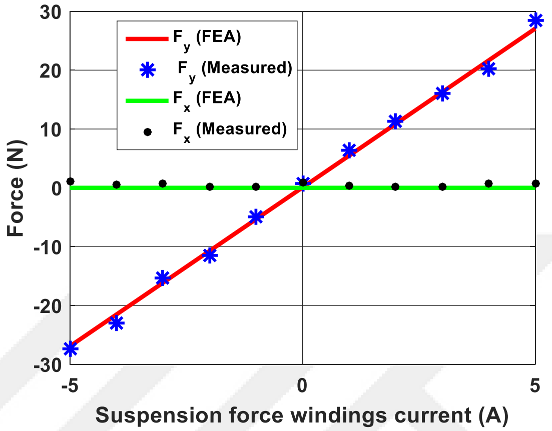

Figure 6.34: The forces exerted on the rotor in the x direction and y direction with only the $A\acute{A}$ coil winding is excited

The reluctance forces on the rotor are measured experimentally and compared with the simulated results. Figure 6.35 shows the reluctance force on the rotor when it is displaced along the x direction.

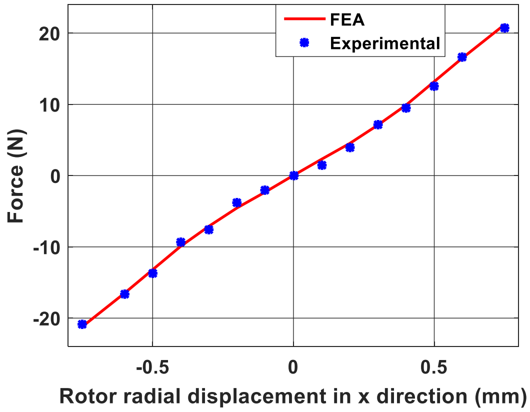

Figure 6.35: The passive force which acts on the rotor when it is displaced from 0 mm to 0.75 mm in the radial x direction

Figure 6.36 shows the passive reluctance force on the rotor when it is displaced along the axial z direction. The experimental axial passive stiffness is measured as 4.93 N/mm.

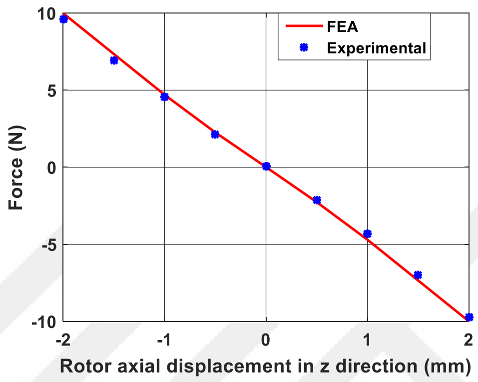

Figure 6.36: The passive force which acts on the rotor when it is displaced from -2 mm to 2 mm in the axial z direction

The rotor is rotated at 9800 rpm. A power amplifier is designed for driving the rotor using 20 kHz PWM voltage. Figure 6.37 shows the radial direction vibrations of the rotor when only the radial bearing force windings are excited.

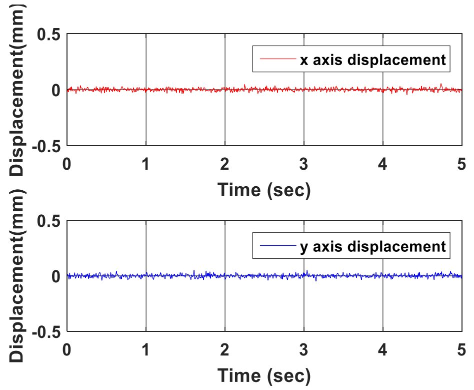

Figure 6.37: Displacement of rotor in radial direction when only the radial bearing force windings are excited

Figure 6.38 shows the oscillations of the rotor when both the motoring torque windings and the radial bearing force windings are excited with a speed of 9800 rpm.

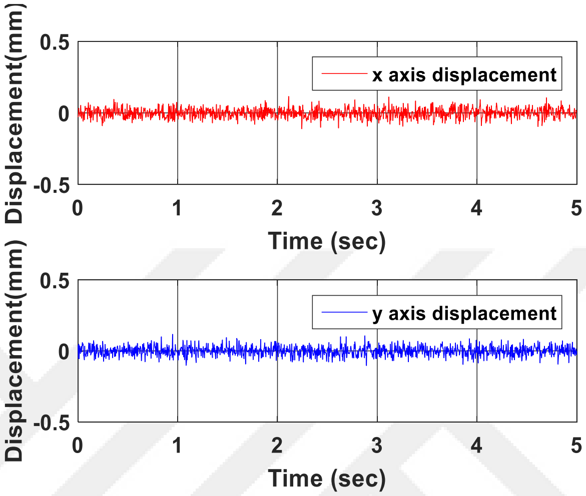

Figure 6.38: Displacement of rotor in radial direction when both the motoring torque windings and the radial bearing force windings are excited

6.7 Summary

In this chapter, a novel design for the bearingless motor is proposed for the miniature axial flow blood pump. The axial length of the rotor is optimized with the analysis performed by the finite element method. Four linear Hall sensors are utilized for the measurement of the rotor displacement in the radial direction. Two Hall sensors are utilized for the measurement of the angular displacement of the rotor. The finite element analysis of the overall bearingless motor is done and the forces, magnetic fluxes, stiffness and the currents are calculated for the various operating conditions. An experimental setup is manufactured and the sensor assembly is implemented in order to measure the radial position of the rotor. The forces, stiffness and magnetic fluxes are experimentally obtained and compared with the simulations. Experimental results show that the proposed sensor assembly measures the radial displacement of the novel bearingless motor with good accuracy.

Chapter 7

CONTROL OF THE NOVEL BEARINGLESS MOTOR

7.1 Introduction

In this chapter, the sliding mode controller is designed for the novel design of the bearingless motor for the miniature sized axial flow blood pump. The sliding mode controller is designed based on the adaptive approximation of the system dynamics function and the system input function in the presence of external interferences, noise and unmodeled dynamics. There are two different permanent magnet rings used in the proposed novel design of the bearingless motor. One magnetic ring is used for the generation of the radial bearing forces and another magnetic ring is used for the measurement of the radial position of the rotor. There is strong nonlinearity and magnetic flux coupling present between the two permanent rings and therefore might affect the position measurement of the rotor using the Hall effect sensors. Hence, for a proper control of the axial flow pump, accurate measurement of the rotor radial displacement is very necessary. For addressing this problem, an adaptive observer is first designed in order to approximate the radial position of the rotor in the presence of noise, unmodeled dynamics and external interferences. Then based on the adaptive observer, an adaptive sliding mode controller is designed for the position control of the novel bearingless motor. The analytical modeling of the rotor is done based on the method of Maxwell stress tensor and the effect of the eccentricity of the rotor is also taken in to account while deriving the analytical model of the proposed bearingless motor. In the proposed control method, no exact knowledge of the unmodeled dynamics, disturbances and the nonlinearities is necessary. For verifying the effectiveness of the proposed adaptive sliding mode controller, the designed controller is applied to the test prototype setup of the bearingless motor. Results show good tracking of the commanded position signal of the rotor in the presence of external interference signals and noise.

7.2 Schematic Diagram of the Proposed Bearingless Motor

The schematic diagram showing the rotor and the stator assembly of the proposed bearingless motor is shown in Figure 7.1 and the overall pump assembly is shown in Figure 7.2.

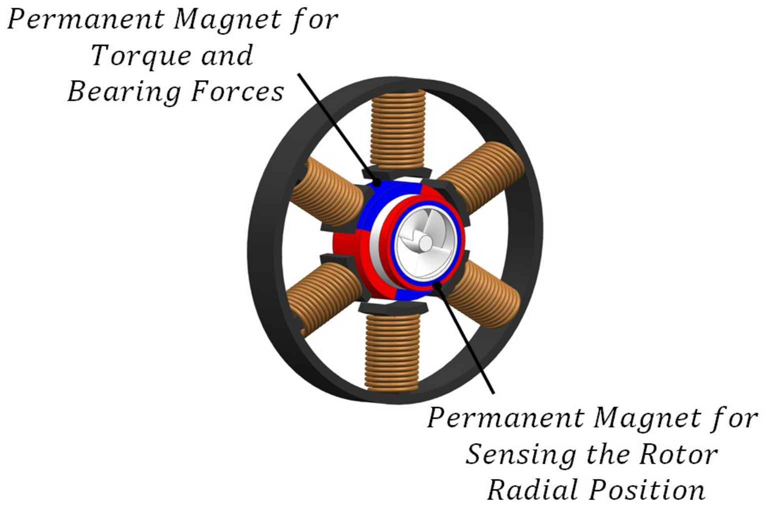

Figure 7.1: The assembly of the proposed rotor and stator

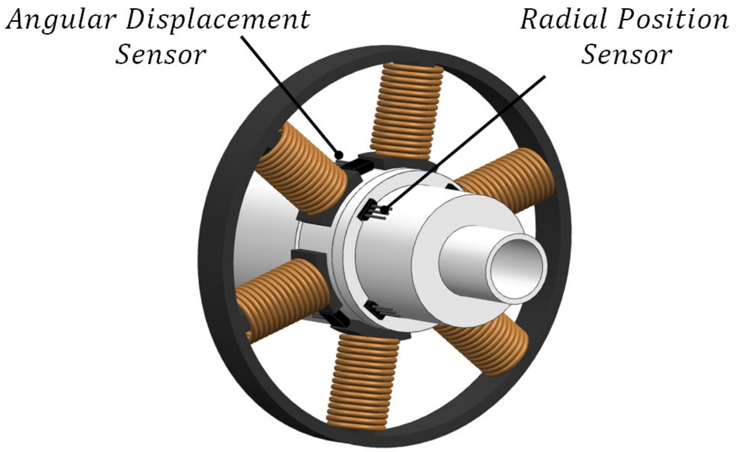

Figure 7.2: The assembly of the overall bearingless pump system

There are two sets of coil windings wound on each of the stator leg. The stator consists of 6 poles and the rotor consists of 4 poles. Four linear Hall effect sensors are used for the measurement of the radial position of the rotor. Two digital Hall effect sensors are utilized for the measurement of the angular displacement of the rotor. The motoring torque windings and the radial bearing force windings are wound in three phase sequence. The bearing winding is two pole and the motoring torque winding is four pole. The rotor length is optimized in the axial direction and hence only bearingless motor is needed for the proper operation of the motor. The rotor is stabilized passively along the tilt direction and along the axial direction utilizing the passive reluctance force which are present between the permanent magnets of the rotor and the iron part of the stator. The stator windings configuration is shown in Figure 7.3. There are three phase windings denoted by s_u, s_v and s_w which are used for generating the radial bearing forces. Another set of three phase windings denoted by d_u, d_v and d_w are wound additionally on the stator connected in three phase sequence in order to generate the motoring torque.

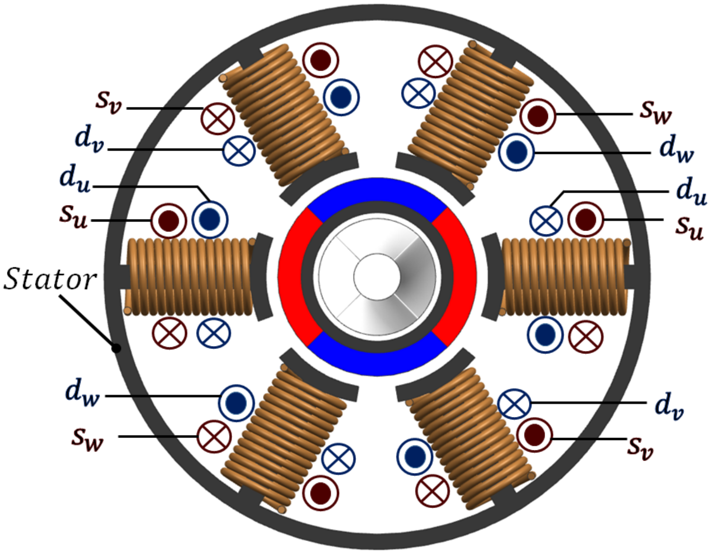

Figure 7.3: The windings arrangement for the motoring torque and the radial bearing forces generation

Figure 7.4 shows the equivalent two phase model for the proposed bearingless motor system. The two pole connected windings N_{Sq} and N_{Sd} are connected in order to generate the radial bearing forces. The four pole connected windings N_{Tq} and N_{Td} are wound for the generation of the motoring torque for the bearingless motor. A four pole magnetic flux denoted by φ_p is generated by the four permanent magnets placed in the rotor for the generation of the radial bearing force and the motoring torque. The magnetic flux which is generated by the radial bearing force windings superimposes the magnetic flux generated by the rotor permanent magnets and as a result a net radial force is generated in the respective α and β directions. For example, in Figure 7.4, the net bearing force is generated in the negative α direction.

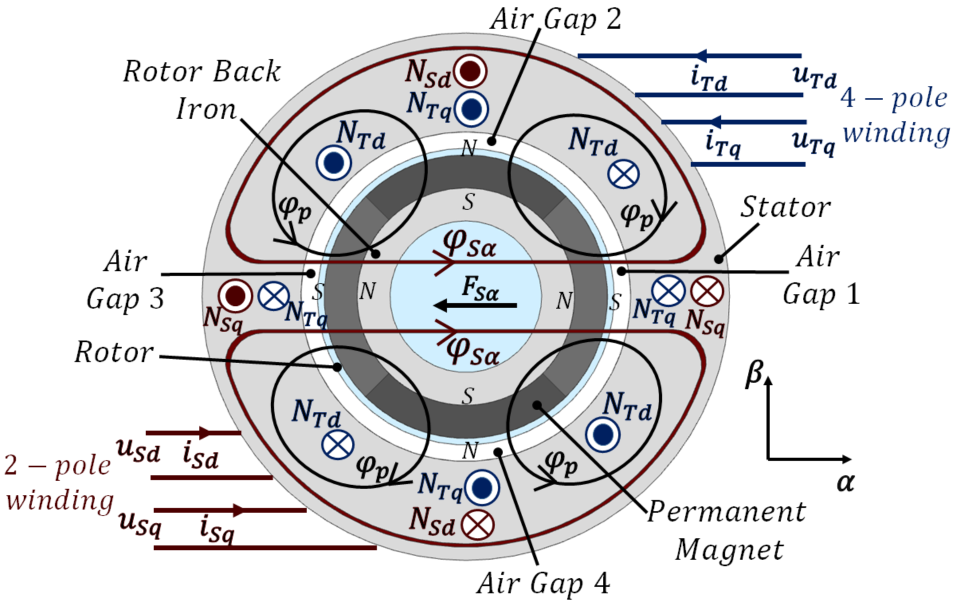

Figure 7.4: The two phase equivalent model of the proposed three phase bearingless motor system

7.3 Analytical Modeling of the Proposed Bearingless Motor

The Maxwell stress force exists in a magnetic circuit across the different materials on their boundary surfaces which have different relative permeabilities. For example, the Maxwell force exists across the stator surface, rotor surface and the airgap. There are two components of this Maxwell force. One component is called the tangential component and another one is called the normal component of the Maxwell force. These components are calculated as given below:

$$dF_{tan} = \frac{(b_{tan}(\theta_r,t)).(b_n(\theta_r,t))}{\mu_0}\mathrm{d}A_r = \left(\frac{(b_{nor}(\theta_r,t)).(b_{tan}(\theta_r,t))}{\mu_0}\right).(r_m l_a d\theta_r) \tag{7.1b}$$

$$dF_{nor} = \left(\frac{b_{nor}^2(\theta_r,t)}{2\mu_0}\right)\mathrm{d}A_r = \left(\frac{b_{nor}^2(\theta_r,t)}{2\mu_0}\right).(r_m l_a d\theta_r) \tag{7.1b}$$

where θ_r is the mechanical angle of the rotor, $\mathrm{d}A_r$ is representing the unit area, r_m is representing the outer radius of the rotor, dF_{tan} is denoting the tangential component of the Maxwell force and the normal component of the Maxwell force is represented by dF_{nor}. The term b_{tan} is denoting the airgap magnetic flux density's tangential component generated due to radial bearing force windings and the motoring torque windings. The term b_{nor} is denoting the airgap magnetic flux density's normal component generated due to radial bearing force windings and the motoring torque windings. The tangential component of the magnetic flux density can be obtained as follows:

$$b_{tan}(\theta_r,t) = -B_{tan}cos(\omega t - P_{To}\theta_r - \xi_{To})$$

where B_{tan} is denoting the amplitude of the magnetic flux density's tangential component, P_{To} is denoting the torque windings pole pairs, ω is the angular velocity and ξ_{To} is the airgap mmf's phase angle which is generated by the pole pairs P_{To} when time t is equal to zero.

From Equation (7.1), the overall magnetic bearing force in the radial α and β directions can be written as below:

$$dF_{S\alpha}(\theta_r) = \left[\left(\frac{b_{nor}^2(\theta_r,t)}{2\mu_0}\right).\left(r_m l_a\, cos(\theta_r)\right) + \left(\frac{\left(b_{nor}(\theta_r,t)\right).\left(b_{tan}(\theta_r,t)\right)}{\mu_0}\right).\left(r_m l_a\, sin(\theta_r)\right)\right] d\theta_r \quad (7.2a)$$

$$dF_{S\beta}(\theta_r) = \left[\left(\frac{b_{nor}^2(\theta_r,t)}{2\mu_0}\right).\left(r_m l_a\, sin(\theta_r)\right) + \left(\frac{\left(b_{nor}(\theta_r,t)\right).\left(b_{tan}(\theta_r,t)\right)}{\mu_0}\right).\left(r_m l_a\, cos(\theta_r)\right)\right] d\theta_r \quad (7.2b)$$

where r_m and l_a values are constant. When there is no deviation of the rotor from the equilibrium position, then this magnetic flux density remains constant. Whenever, there is a rotor eccentricity, then the magnetic flux density value is changed based upon the displacement of the rotor. The eccentricity of the rotor system can be shown in Figure 7.5.

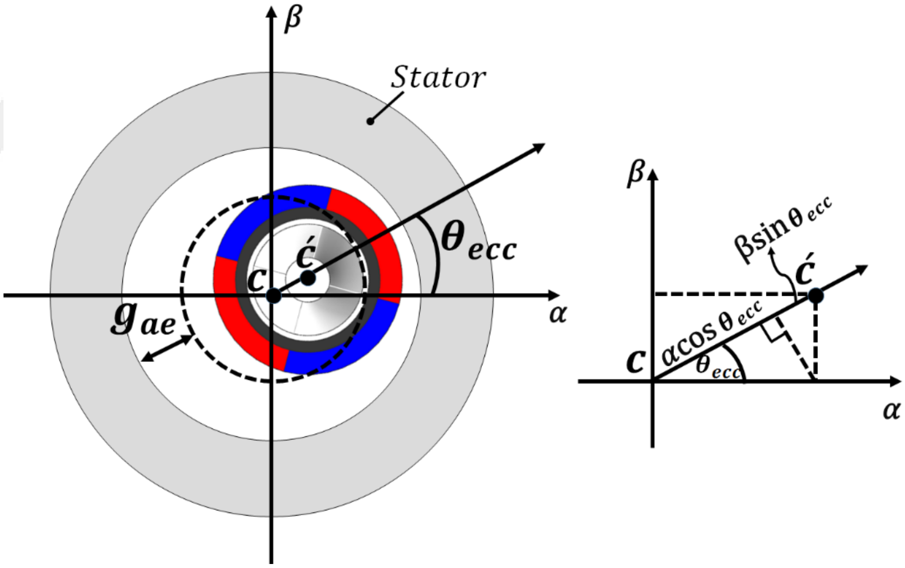

Figure 7.5: The eccentricity of the rotor for the proposed bearingless motor

The eccentricity of the rotor can be found as below:

$$\varepsilon_{rotor} = \frac{\sqrt{\alpha^2 + \beta^2}}{g_{ae}}$$

where ε_{rotor} is denoting the eccentricity of rotor and g_{ae} is the airgap when the rotor is at equilibrium position. The eccentricity distance of the rotor can be obtained as below:

$$g_{ae}(\theta_{ecc}) = g_{ae} - \beta\sin(\theta_{ecc}) - (\alpha\cos(\theta_{ecc}) \tag{7.3}$$

and the angle of eccentricity θ_{ecc} is given as below:

$$\theta_{ecc} = tan^{-1}\frac{\beta}{\alpha}$$

The permeance per unit area for the airgap is found as below:

$$\Lambda(\theta_{ecc}) = \frac{\mu_0}{(\theta_{ecc})g} \approx \frac{\mu_0}{g_{ae}^2}(\alpha\cos(\theta_{ecc}) + \beta\sin(\theta_{ecc}) + g_{ae}) \tag{7.4}$$

where $\Lambda(\theta_{ecc})$ is denoting the airgap permeance. When the higher order terms are neglected, then the airgap's mmf fundamental component can be calculated as follows:

$$f_{To}(\theta_r, t) = F_{To}\cos(\omega t - P_{To}\theta_r - \xi_{To}) \tag{7.5a}$$

$$f_S(\theta_r, t) = F_S\cos(\omega t - P_S\theta_r - \xi_S) \tag{7.5b}$$

where $f_{To}(\theta_r, t)$ is denoting the airgap mmf which is produced due to the motoring torque windings and the rotor permanent magnets and has an amplitude of F_{To}. The $f_S(\theta_r, t)$ is denoting the airgap mmf which is produced due to the radial bearing force windings and the rotor permanent magnets and has an amplitude of F_S. Therefore, the overall distribution of the magnetic flux density in the airgap at all the angles can be calculated as given below:

$$b_{To}(\theta_r, t) = \left(f_{To}(\theta_r, t)\right).\left(\Lambda(\theta_{ecc})\right)$$

$$b_S(\theta_m, t) = \left(f_S(\theta_m, t)\right).\left(\Lambda(\theta_{ecc})\right)$$

where the normal component of the airgap magnetic flux density is given as below:

$$b_{nor}(\theta_r, t) = b_S(\theta_r, t) + b_{To}(\theta_r, t)$$

The amplitude of the corresponding magnetic flux densities in the airgap can be calculated as below:

$$B_{To} = F_{To}\frac{\mu_0}{g_{ae}} = \frac{\mu_0}{g_{ae}}\left(\frac{I_{To}N_{To}}{P_{To}}.\frac{3}{\pi}\right)$$

$$B_S = F_S\frac{\mu_0}{g_{ae}} = \frac{\mu_0}{g_{ae}}\left(\frac{I_S N_S}{P_S}.\frac{3}{\pi}\right)$$

Here, the magnetic flux amplitude which is produced due to the motoring torque windings and the rotor permanent magnets is denoted by B_{To} and the magnetic flux amplitude which is obtained because of the radial bearing force windings is denoted by B_S. N_{To} is representing the number of turns of the motoring torque windings while N_S is denoting the number of turns for the radial bearing force windings. I_{To} is the current through the motoring torque windings while the current in the radial bearing force windings is I_S. Hence, in order to obtain the total amount of radial force in the α and β directions, the integral of Equation (2) is computer from 0 to 2π and the higher order terms are neglected. The radial bearing forces are given as follows:

$$F_{S\alpha} \approx \frac{l_a r_m \pi}{2\mu_0}\left[B_S B_{To}\cos(\xi_{To}-\xi_S)+\frac{B_{To}^2\alpha}{g_{ae}}\right]+\frac{l_a r_m \pi\, B_{tan}\beta}{2g_{ae}\mu_0}B_{To} \qquad (7.6a)$$

$$F_{S\beta} \approx \frac{l_a r_m \pi}{2\mu_0}\left[B_S B_{To}\sin(\xi_{To}-\xi_S)+\frac{B_{To}^2\beta}{g_{ae}}\right]+\frac{l_a r_m \pi\, B_{tan}\alpha}{2g_{ae}\mu_0}B_{To} \qquad (7.6b)$$

The torque windings airgap magnetic flux linkage can be written as follows:

$$\psi_{To} = N_{To}\varphi_{To} = \frac{2r_m l_a N_{To} B_{To}}{P_{To}}$$

Also, we know that;

$$\psi_{To} = L_{To} I_{To}$$

where L_{To} is denoting the mutual inductance of the motoring torque windings. Therefore, the Equation (7.6) can be rewritten as follows:

$$F_{S\alpha} \approx c_2\psi_{To}^2\alpha + c_1 I_S\psi_{To}\cos(\xi_{To}-\xi_S) + c_3\psi_{To}\beta \qquad (7.7a)$$

$$F_{S\beta} \approx c_2\psi_{To}^2\beta + c_1 I_S\psi_{To}\sin(\xi_{To}-\xi_S) + c_3\psi_{To}\alpha \qquad (7.7b)$$

where $c_1 = \frac{9r_m l_a \mu_0 N_{To} N_S}{4\pi L_{To} g_{ae}^2}$, $c_2 = \frac{9r_m \mu_0 l_a N_{To}^2}{8\pi L_{To}^2 g_{ae}^3}$, and $c_2 = \frac{3r_m l_a N_T B_{tan}}{4\pi L_{To} g_a^2}$

The second component in Equation (7.7) is generated due to the current in the radial bearing force windings. It can be easily converted into the d-q reference frame as follows:

$$c_1 I_S\psi_{To}\cos(\xi_{To}-\xi_S) = c_1(\psi_{Toq}I_{Sq} + \psi_{Tod}I_{Sd})$$

$$c_1 I_S\psi_{To}\sin(\xi_{To}-\xi_S) = c_1(-\psi_{T0d}I_{Sq} + \psi_{Toq}I_{Sd})$$

where ψ_{Toq} and ψ_{T0d} are the flux linkage components of the motoring torque windings in the d-q frame of reference. When the vector control is used for the bearingless motor, then it is known that; $\psi_{Toq} = 0$ and $\psi_{Tod} = \psi_{To}$. Therefore,

$$c_1 I_S \psi_{To} \cos(\xi_{To} - \xi_S) = c_1 \psi_{Tod} I_{Sd}$$

$$c_1 I_S \psi_{To} \sin(\xi_{To} - \xi_S) = -c_1 \psi_{T0d} I_{Sq}$$

Therefore, Equation (7.7) can be rewritten as follows:

$$F_{S\alpha} \approx c_2 \psi_{To}^2 \alpha + c_1 \psi_{Tod} I_{Sd} + c_3 \psi_{To} \beta \tag{7.8a}$$

$$F_{S\beta} \approx c_2 \psi_{To}^2 \beta - c_1 \psi_{T0d} I_{Sq} + c_3 \psi_{To} \alpha \tag{7.8b}$$

Therefore, the equation of motion can be written as follows:

$$m\ddot{\alpha} = f_\alpha + F_{S\alpha} - f_{\alpha d} \tag{7.9a}$$

$$m\ddot{\beta} = f_\beta + F_{S\beta} - f_{\beta d} \tag{7.9b}$$

where $f_\alpha = c_2 \psi_{To}^2 \alpha$ and $f_\beta = c_2 \psi_{To}^2 \beta$. Equation (7.9) can be written as follows:

$$\begin{cases} \ddot{\alpha} = \frac{1}{m} c_2 \psi_{To}^2 \alpha + \frac{1}{m} F_{S\alpha} - \frac{1}{m} f_{\alpha d} \\ \ddot{y} = \frac{1}{m} c_2 \psi_{To}^2 \beta + \frac{1}{m} F_{S\beta} - \frac{1}{m} f_{yd} \end{cases} \tag{7.10}$$

By choosing the state variables as: $\alpha_1 = \alpha$, $\alpha_2 = \dot{\alpha}$ and $u = F_{S\alpha}$, the α –direction equation can be rewritten as follows:

$$\begin{cases} \dot{\alpha_1} = \alpha_2 \\ \dot{\alpha_2} = f_b(\alpha_1) + g_b(\alpha_1) u_c + f_d \\ z = \alpha_1 \end{cases} \tag{7.11}$$

The analysis along the β-direction is the same as the x-direction. The term f_d is representing the unmodeled system dynamics and disturbances and $u_c = F_{S\alpha}$, $f_b(\alpha_1) = \frac{1}{m} c_2 \psi_{To}^2 \alpha$.

7.4 Design of Adaptive Sliding Mode Controller

In this chapter, a sliding mode controller is designed for the position control of the novel bearingless motor. First an adaptive observer is designed, based on which a sliding mode controller is designed as a second step.

7.4.1 Adaptive Observer Design

The Equation (7.11) can be written as follows:

$$\begin{cases} \dot{\boldsymbol{\alpha}} = \boldsymbol{A\alpha} + \boldsymbol{b}[f_b(\boldsymbol{\alpha}) + g_b(\boldsymbol{\alpha})u_c + d(t)] \\ \qquad\qquad z = \boldsymbol{C}^T\boldsymbol{\alpha} \end{cases} \tag{7.12}$$

where $\boldsymbol{A} = \begin{bmatrix} 0 & 1 \\ 0 & 0 \end{bmatrix}$, $\boldsymbol{b} = \begin{bmatrix} 0 \\ 1 \end{bmatrix}$, $\boldsymbol{C} = \begin{bmatrix} 1 \\ 0 \end{bmatrix}$, $\boldsymbol{\alpha} = \begin{bmatrix} x_1 \\ x_2 \end{bmatrix}$, $f_b(\boldsymbol{\alpha})$ and $g_b(\boldsymbol{\alpha})$ are nonlinear unknow functions, and d is denoting the disturbance included in the system with $d \le D_{max}$.

The observer based on the radial basis function for the Equation (7.12) can be written as follows:

$$\begin{cases} \dot{\hat{\boldsymbol{\alpha}}} = \boldsymbol{A}\hat{\boldsymbol{\alpha}} + \boldsymbol{b}[\hat{f}_b(\hat{\boldsymbol{\alpha}}) + \hat{g}_b(\hat{\boldsymbol{\alpha}})u_c - r(t)] + \boldsymbol{L}(c - \boldsymbol{C}^T\hat{\boldsymbol{\alpha}}) \\ \qquad\qquad\qquad\qquad \hat{z} = \boldsymbol{C}^T\hat{\boldsymbol{\alpha}} \end{cases} \tag{7.13}$$

where the gain vector is given as $\boldsymbol{L} = [l_1\ l_2]^T$. The output state value from the observer is given as $\hat{\boldsymbol{\alpha}}$**.** $\hat{f}_b(\hat{\boldsymbol{\alpha}})$ is the observed system dynamics function and $\hat{g}_b(\hat{\boldsymbol{\alpha}})$ is the observed system input function. $r(t)$ is representing the robustness term in Equation (7.13). The radial basis function output can be written as follows:

$$v_j = e^{-\left(\frac{\|\alpha_t - c_j\|}{\sqrt{2}b_j}\right)^2} \tag{7.14}$$

where c is denoting the center point of the Gaussian function for the network j. Therefore,

$$f_b(\boldsymbol{\alpha}) = \boldsymbol{M^T v_f}(\boldsymbol{\alpha}) + \rho_f$$
$$g_b(\boldsymbol{\alpha}) = \boldsymbol{N^T v_g}(\boldsymbol{\alpha}) + \rho_g$$

where the input vector to the radial basis function (RBF) network is given as $\boldsymbol{\alpha}$**,** and the ideal weights of the RBF are given as $\boldsymbol{M}$ and $\boldsymbol{N}$**.** Also, $\boldsymbol{M} \le \boldsymbol{M_{max}}$ and $\boldsymbol{N} \le \boldsymbol{N_{max}}$, the ρ_f and ρ_g are denoting the approximation errors of the RBF network with $\rho_f \le \rho_{max}$ and $\rho_g \le \rho_{max}$. Therefore, the two functions can be estimated using the RBF network as follows:

$$\hat{f}_b(\hat{\boldsymbol{\alpha}}) = \boldsymbol{\widehat{M}^T v_f}(\hat{\boldsymbol{\alpha}})$$

$$\hat{g}_b(\hat{\boldsymbol{\alpha}}) = \boldsymbol{\widehat{N}^T v_g}(\hat{\boldsymbol{\alpha}})$$

where $\hat{f}_b$ and $\hat{g}_b$ are denoting the estimates of the original functions. The approximation errors can be calculated as below:

$$\tilde{f}_b(\boldsymbol{\alpha},\widehat{\boldsymbol{\alpha}}) = f_b(\boldsymbol{\alpha}) - \hat{f}_b(\widehat{\boldsymbol{\alpha}}) = \boldsymbol{M}^{\boldsymbol{T}}\boldsymbol{\nu}_{\boldsymbol{f}}(\boldsymbol{\alpha}) - \widehat{\boldsymbol{M}}^{\boldsymbol{T}}\widehat{\boldsymbol{\nu}}_f(\boldsymbol{\alpha}) + \rho_f \tag{7.15}$$

$$\tilde{g}_b(\boldsymbol{\alpha},\widehat{\boldsymbol{\alpha}}) = g_b(\boldsymbol{\alpha}) - \hat{g}_b(\widehat{\boldsymbol{\alpha}}) = \boldsymbol{N}^{\boldsymbol{T}}\boldsymbol{\nu}_{\boldsymbol{g}}(\boldsymbol{\alpha}) - \widehat{\boldsymbol{N}}^{\boldsymbol{T}}\widehat{\boldsymbol{\nu}}_g(\widehat{\boldsymbol{\alpha}}) + \rho_g \tag{7.16}$$

The approximation errors in the weights are given as below:

$$\widetilde{\boldsymbol{M}} = \boldsymbol{M} - \widehat{\boldsymbol{M}}$$

$$\widetilde{\boldsymbol{N}} = \boldsymbol{N} - \widehat{\boldsymbol{N}}$$

The error in output of neuron is given as follows:

$$\tilde{\boldsymbol{\nu}}_f(\boldsymbol{\alpha},\widehat{\boldsymbol{\alpha}}) = \boldsymbol{\nu}_f(\boldsymbol{\alpha}) - \widehat{\boldsymbol{\nu}}_f(\widehat{\boldsymbol{\alpha}})$$

$$\tilde{\boldsymbol{\nu}}_g(\boldsymbol{\alpha},\widehat{\boldsymbol{\alpha}}) = \boldsymbol{\nu}_g(\boldsymbol{\alpha}) - \widehat{\boldsymbol{\nu}}_g(\widehat{\boldsymbol{\alpha}})$$

Adding and subtracting the term $\boldsymbol{M}^{\boldsymbol{T}}\boldsymbol{\nu}_{\boldsymbol{f}}(\widehat{\boldsymbol{\alpha}})$ from Equation (7.15) we get:

$$\tilde{f}_b(\boldsymbol{\alpha},\widehat{\boldsymbol{\alpha}}) = \widetilde{\boldsymbol{M}}^{\boldsymbol{T}}\widehat{\boldsymbol{\nu}}_f(\widehat{\boldsymbol{\alpha}}) + w_1(t) + \rho_f$$

where $w_1(t)$ is given by $\boldsymbol{M}^{\boldsymbol{T}}\tilde{\boldsymbol{\nu}}_f(\boldsymbol{\alpha},\widehat{\boldsymbol{\alpha}})$ with $w_1(t) \le \varepsilon_1$ and also $\varepsilon_1 > 0$.

Also, from Equation (7.16) we obtain the following:

$$\tilde{g}_b(\boldsymbol{\alpha},\widehat{\boldsymbol{\alpha}}) = \widetilde{\boldsymbol{N}}^{\boldsymbol{T}}\widehat{\boldsymbol{\nu}}_g(\widehat{\boldsymbol{\alpha}}) + w_2(t) + \rho_g$$

where $w_2(t)$ is given by $\boldsymbol{N}^{\boldsymbol{T}}\tilde{\boldsymbol{\nu}}_g(\boldsymbol{\alpha},\widehat{\boldsymbol{\alpha}})$ with $w_2(t) \le \varepsilon_2$ and also $\varepsilon_2 > 0$.

There is an upper bound on the control input i.e. $|u_c| \le u_{c_{max}}$ and hence, the observer and its stability proof can be derived as given in [120] and is provided as below:

$$\begin{cases} \dot{\widehat{\boldsymbol{\alpha}}} = \boldsymbol{A}\widehat{\boldsymbol{\alpha}} + \boldsymbol{b}\left[\widehat{\boldsymbol{M}}^{\boldsymbol{T}}\widehat{\boldsymbol{\nu}}_f(\widehat{\boldsymbol{\alpha}}) + \widehat{\boldsymbol{N}}^{\boldsymbol{T}}\widehat{\boldsymbol{\nu}}_g(\widehat{\boldsymbol{\alpha}})u_c - r_1 - r_2\right] \\ \qquad\qquad +\boldsymbol{L}(z - \boldsymbol{C}^T\widehat{\boldsymbol{\alpha}}) \\ \qquad\qquad \hat{z} = \boldsymbol{C}^T\widehat{\boldsymbol{\alpha}} \end{cases} \tag{7.17}$$

Also, the equation of the estimation error for the state is given as follows:

$$\begin{aligned} \dot{\widetilde{\boldsymbol{\alpha}}} &= (\boldsymbol{A} - \boldsymbol{L}C^T)\widetilde{\boldsymbol{\alpha}} + \boldsymbol{b}[\widetilde{\boldsymbol{M}}^{\boldsymbol{T}}\widehat{\boldsymbol{\nu}}_f(\widehat{\boldsymbol{\alpha}}) + r_1 + w_1(t) \\ &\quad +\rho_f + (\widetilde{\boldsymbol{N}}^{\boldsymbol{T}}\widehat{\boldsymbol{\nu}}_g(\widehat{\boldsymbol{\alpha}}) + w_2(t)u_c + \rho_g + r_2 + d) \\ \tilde{z} &= \boldsymbol{C}^T\widetilde{\boldsymbol{\alpha}} \end{aligned} \tag{7.18a}$$

where

$r_1 = -R_1 \frac{\tilde{z}}{|\tilde{z}|}$ and $r_2 = -R_2 \frac{\tilde{z}}{|\tilde{z}|}$ (7.18b)

where the robust terms are given by r_1 and r_2 given that $R_1 \geq \vartheta_M \varepsilon_1$ and $R_2 \geq \vartheta_M \varepsilon_2 u_{c_{max}}$. The term ϑ_M is given as $\vartheta_M = \vartheta_{max}[G^{-1}(s)]$, where the value ϑ_{max} is representing the maximum singular value of the transfer function $G^{-1}(s)$. The transfer function $G^{-1}(s)$ is proper and having all stable poles. And this transfer function is chosen in such a way that the combined transfer function $T(s)G(s)$ should be strictly proper. The transfer function $T(s)$ is given as follows:

$T(s) = \boldsymbol{C}^T(s\boldsymbol{I} - (\boldsymbol{A} - \boldsymbol{L}\boldsymbol{C}^T))^{-1}\boldsymbol{b}$ (7.19)

Therefore,

$\tilde{z} = G(s)[\widetilde{\boldsymbol{M}}^{\boldsymbol{T}}\hat{\boldsymbol{v}}_f(\hat{\boldsymbol{\alpha}}) + (\widetilde{\boldsymbol{N}}^{\boldsymbol{T}}\hat{\boldsymbol{v}}_g(\hat{\boldsymbol{\alpha}}) + w_2(t) + \rho_g)u_c + \rho_f + w_1(t) + r_1 + r_2 + d]$ (7.20)

Stability Analysis:

Equation (7.20) can be rewritten as follows:

$\tilde{z} = G(s)T(s)[\widetilde{\boldsymbol{M}}^{\boldsymbol{T}}\hat{\bar{\boldsymbol{v}}}_{\boldsymbol{f}}(\hat{\boldsymbol{\alpha}}) + \widetilde{\boldsymbol{N}}^{\boldsymbol{T}}\hat{\bar{\boldsymbol{v}}}_{\boldsymbol{g}}(\hat{\boldsymbol{\alpha}})u_c + \bar{w}_2(t)u_c + \bar{\rho}_g u_c + \bar{w}_1(t) +$

$\bar{r}_1 + \bar{r}_2 + \bar{d} + \delta_1 + \delta_2]$ (7.21)

where $\hat{\bar{\boldsymbol{v}}}_{\boldsymbol{f}}(\hat{\boldsymbol{\alpha}}) = T^{-1}(s)\hat{\boldsymbol{v}}_f(\hat{\boldsymbol{\alpha}})$ and in the same manner all the terms with overbar represents that the terms have been filtered through the transfer function $G^{-1}(s)$. Also,

$\delta_1(t) = G^{-1}(s)\left[\widetilde{\boldsymbol{M}}^{\boldsymbol{T}}\hat{\boldsymbol{v}}_f(\hat{\boldsymbol{\alpha}})\right] - \widetilde{\boldsymbol{M}}^{\boldsymbol{T}}T^{-1}(s)\left[\hat{\boldsymbol{v}}_f(\hat{\boldsymbol{\alpha}})\right]$

$\delta_2(t) = G^{-1}(s)\left[\widetilde{\boldsymbol{N}}^{\boldsymbol{T}}\hat{\boldsymbol{v}}_g(\hat{\boldsymbol{\alpha}})\right] - \widetilde{\boldsymbol{N}}^{\boldsymbol{T}}T^{-1}(s)\left[\hat{\boldsymbol{v}}_g(\hat{\boldsymbol{\alpha}})\right]u_c$

and $\|\delta_1(t)\| \leq c_1\|\widetilde{\boldsymbol{M}}\|_{\boldsymbol{F}}$, $\|\delta_2(t)\| \leq c_2\|\widetilde{\boldsymbol{N}}\|_{\boldsymbol{F}}$ with $c_1, c_2 > 0$.

Here the term $\|\boldsymbol{I}\|_{\boldsymbol{F}}^2$ is denoting the frobenius norm for a matrix $\boldsymbol{I}$. Equation (7.21) can be written as follows:

$\dot{\widetilde{\boldsymbol{\chi}}} = \boldsymbol{A}_{\boldsymbol{m}}\tilde{\chi} + \boldsymbol{b}_{\boldsymbol{m}}(\widetilde{\boldsymbol{M}}^{\boldsymbol{T}}\hat{\bar{\boldsymbol{v}}}_{\boldsymbol{f}}(\hat{\boldsymbol{\alpha}}) + \widetilde{\boldsymbol{N}}^{\boldsymbol{T}}\hat{\bar{\boldsymbol{v}}}_{\boldsymbol{g}}(\hat{\boldsymbol{\alpha}})u + \bar{w}_2(t)u + \bar{\rho}_g u_c$

$+\bar{w}_1(t) + \bar{r}_1 + \bar{r}_2 + \bar{d} + \delta_1 + \delta_2)$

$\tilde{z} = \boldsymbol{C}_{\boldsymbol{m}}^T\widetilde{\boldsymbol{\chi}}$

where ($\boldsymbol{A_m} \epsilon \mathbb{R}^{n\times n}$, $\boldsymbol{b_m} \epsilon \mathbb{R}^{n}$ and , $\boldsymbol{C_m} \epsilon \mathbb{R}^{n}$) is denoting a minimal state representation of $T(s)G(s) = \boldsymbol{C_m}^T (s\boldsymbol{I} - \boldsymbol{A_m})^{-1} \boldsymbol{b_m}$.

Therefore, the adaptive is designed as following:

$$\dot{\widehat{\boldsymbol{P}}} = \boldsymbol{V_1} \widehat{\boldsymbol{v}}_{\boldsymbol{f}}(\widehat{\boldsymbol{\alpha}}) \tilde{z} - a_1 \boldsymbol{V_1} |\tilde{z}| \widehat{\boldsymbol{P}} \tag{7.22}$$

$$\dot{\widehat{\boldsymbol{Q}}} = \boldsymbol{V_2} \widehat{\boldsymbol{v}}_{\boldsymbol{g}}(\widehat{\boldsymbol{\alpha}}) \tilde{z} u_c - a_2 \boldsymbol{V_2} |\tilde{z}| \widehat{\boldsymbol{Q}}$$

where $a_1, a_2 > 0$, $\boldsymbol{V_1} = \boldsymbol{V_1}^{\boldsymbol{T}} > 0$ and $\boldsymbol{V_2} = \boldsymbol{V_2}^{\boldsymbol{T}} > 0$

The Lyapunov function is chosen as follows:

$$V = \frac{1}{2} \tilde{\chi}^T S \tilde{\chi} + \frac{1}{2} tr\left(\widetilde{\boldsymbol{M}}^{\boldsymbol{T}} \boldsymbol{V_1}^{-\boldsymbol{1}} \widetilde{\boldsymbol{M}}\right) + \frac{1}{2} tr\left(\widetilde{\boldsymbol{N}}^{\boldsymbol{T}} \boldsymbol{V_2}^{-\boldsymbol{1}} \widetilde{\boldsymbol{N}}\right)$$

where the term $S = S^T > 0$.

As the transfer function $T(s)G(s)$ is strictly proper, therefore there exists R= $R^T > 0$ such that:

$$A_m{}^T R + R A_m = -H \text{ , } R b_m = C_m \text{ with } H = H^T > 0.$$

The time derivative of (23) is given as follows:

$$\dot{V} = -\frac{1}{2} \tilde{\chi}^T H \tilde{\chi} + \tilde{z}(\widehat{\boldsymbol{M}}^{\boldsymbol{T}} \widehat{\boldsymbol{v}}_f(\widehat{\boldsymbol{\alpha}}) + \widehat{\boldsymbol{N}}^{\boldsymbol{T}} \widehat{\boldsymbol{v}}_g(\widehat{\boldsymbol{\alpha}}) u_c + \overline{w}_2(t) u_c$$
$$+ \bar{\rho}_g u + \overline{w}_1(t) + \bar{r}_1 + \bar{r}_2 + \bar{d} + \delta_1 + \delta_2) + tr(\widetilde{\boldsymbol{M}}^{\boldsymbol{T}} \boldsymbol{V_1}^{-\boldsymbol{1}} \dot{\widetilde{\boldsymbol{M}}}) + tr(\widetilde{\boldsymbol{N}}^{\boldsymbol{T}} \boldsymbol{V_2}^{-\boldsymbol{1}} \dot{\widetilde{\boldsymbol{N}}}) \tag{7.24}$$

Therefore, by evaluating Equation (7.24) along trajectories (7.18) and (7.22) yields:

$$\dot{V} \leq -\frac{1}{2} \lambda_{min}(H) \, \|\tilde{\chi}\|^2 + |\tilde{z}|(\overline{w}_2(t) u_c + \overline{w}_1(t) + \bar{d}$$
$$+ c_1 \|\widetilde{\boldsymbol{M}}\|_{\boldsymbol{F}} + c_2 \|\widetilde{\boldsymbol{N}}\|_{\boldsymbol{F}}) + a_1 \boldsymbol{V_1} |\tilde{y}| tr[\widetilde{\boldsymbol{M}}^{\boldsymbol{T}} (\boldsymbol{M} - \widetilde{\boldsymbol{M}})]$$
$$+ a_2 \boldsymbol{V_2} |\tilde{z}| tr[\widetilde{\boldsymbol{N}}^{\boldsymbol{T}} (\boldsymbol{N} - \boldsymbol{N})]$$

where $\lambda_{min}(H)$ is denoting the smallest eigenvalue of the matrix H.

As $-\lambda_{min}(H) \, \|\tilde{\chi}\|^2 \leq -\lambda_{min}(H) |\tilde{z}|^{\boldsymbol{2}}$ and

$$tr\left[\widetilde{\boldsymbol{M}}^{\boldsymbol{T}} \left(\boldsymbol{M} - \widetilde{\boldsymbol{M}}\right)\right] \leq \boldsymbol{M_{max}} \|\widetilde{\boldsymbol{M}}\|_{\boldsymbol{F}} - \|\widetilde{\boldsymbol{M}}\|_{\boldsymbol{F}}^2$$

$$tr\left[\widetilde{\boldsymbol{N}}^{\boldsymbol{T}} \left(\boldsymbol{N} - \widetilde{\boldsymbol{N}}\right)\right] \leq \boldsymbol{N_{max}} \|\widetilde{\boldsymbol{N}}\|_{\boldsymbol{F}} - \|\widetilde{\boldsymbol{N}}\|_{\boldsymbol{F}}^2$$

Therefore:

$$\dot{V} \leq |\tilde{z}|[\frac{1}{2}\lambda_{min}(H)|\tilde{z}| - \vartheta_M\big(D_{max} + \rho_{max} + \rho_{max}u_{c_{max}}\big) - \gamma_1(\alpha_1\|\widetilde{\boldsymbol{P}}\|_{\boldsymbol{F}}$$
$$- \|\widetilde{\boldsymbol{P}}\|_{\boldsymbol{F}}^2) - \gamma_2(\alpha_2\|\widetilde{\boldsymbol{Q}}\|_{\boldsymbol{F}} - \|\widetilde{\boldsymbol{Q}}\|_{\boldsymbol{F}}^2] \qquad (7.25)$$

where $\gamma_1 = a_1\boldsymbol{V_1}$, $\gamma_2 = a_2\boldsymbol{V_2}$, $\alpha_1 = \boldsymbol{M_{max}} + \frac{c_1}{\gamma_1}$ and $\alpha_2 = \boldsymbol{N_{max}} + \frac{c_2}{\gamma_2}$

Therefore, in order to get $\dot{V}$ as a negative value, the following condition must be satisfied:

$$|\tilde{z}| \geq max\left\{\frac{4\vartheta_M(D_{max}+\rho_{max}+ \gamma_1\alpha_1^2}{\lambda_{min}(H)}, \frac{4\vartheta_M\rho_{max}u_{c_{max}}+ \gamma_2\alpha_2^2}{\lambda_{min}(H)}\right\}$$

(7.26)

or

$$\|\widetilde{\boldsymbol{M}}\|_{\boldsymbol{F}} \geq \frac{1}{2}\alpha_1 + \left(\frac{\vartheta_M(D_{max}+\rho_{max})}{\gamma_1} + \frac{\alpha_1^2}{4}\right)^{\frac{1}{2}}$$

(7.27)

$$\|\widetilde{\boldsymbol{N}}\|_{\boldsymbol{F}} \geq \frac{1}{2}\alpha_2 + \left(\frac{\vartheta_M\rho_{max}u_{c_{max}}}{\gamma_2} + \frac{\alpha_2^2}{4}\right)^{\frac{1}{2}} \qquad (7.28)$$

Hence, by using the Lyapunov standard theorem, Equation (7.25) -(7.28) show that $\|\widetilde{\boldsymbol{M}}\|_{\boldsymbol{F}}$, $\|\tilde{\chi}\|$ and $\|\widetilde{\boldsymbol{N}}\|_{\boldsymbol{F}}$ are uniformly ultimately bounded.

The system of Equation (7.18a) can be rewritten as follows:

$$\dot{\widetilde{\boldsymbol{\alpha}}} = (\boldsymbol{A} - \boldsymbol{LC^T})\widetilde{\boldsymbol{\alpha}} + \boldsymbol{b}\tilde{u}_c \qquad (7.29)$$

Then the solution of Equation (7.29) can be written as follows:

$$\tilde{\alpha}(t) = \tilde{\alpha}(0)\emptyset(t,0) + \int_0^t \emptyset(t,\lambda)b\tilde{u}_c(\lambda)d\lambda$$

where $\emptyset(t,0) = e^{\int_0^t(A-LC^T)dt}$,

$\emptyset(t,\lambda) = e^{\int_0^t(A-LC^T)dt - \int_0^\lambda(A-LC^T)d\lambda}$ and

$$\tilde{u}_c = \widetilde{\boldsymbol{M}}^{\boldsymbol{T}}\hat{\boldsymbol{v}}_f(\widehat{\boldsymbol{\alpha}}) + \big(\widetilde{\boldsymbol{N}}^{\boldsymbol{T}}\hat{\boldsymbol{v}}_g(\widehat{\boldsymbol{\alpha}}) + w_2(t) + \rho_g\big)u_c + \rho_f$$
$$+w_1(t) + r_1 + r_2 + d$$

Therefore;

$$e^{\int_0^t (\boldsymbol{A}-\boldsymbol{LC^T})dt-\int_0^\lambda (\boldsymbol{A}-\boldsymbol{LC^T})d\lambda} = e^{(t-\lambda)}e^{(\boldsymbol{A}-\boldsymbol{LC^T})}$$

$$= e^{-\boldsymbol{LC^T}(t-\lambda)}e^{\boldsymbol{A}(t-\lambda)}$$

$$= k_0 e^{-k_1(t-\lambda)}$$

where $k_1 = \boldsymbol{LC^T}$ and $k_0 = e^{\boldsymbol{A}(t-\lambda)}$. Therefore, the expression $\emptyset(t,\lambda)$ is bounded by $k_0 e^{-n(t-\lambda)}$ with positive values of constants k_0 and k_1.

7.4.2 Design of Sliding Mode Controller

Let the desired output radial displacement of the shaft is given by α_r and the actual displacement is given by α. Therefore, the error can be written as follows:

$$e = \alpha_1 - \alpha_r$$

By using the values from observer, we have:

$$e = \hat{\alpha}_1 - \alpha_r$$

$$\dot{e} = \dot{\hat{\alpha}}_1 - \dot{\alpha}_r = \hat{\alpha}_2 - \dot{\alpha}_r$$

The sliding function is designed as follows:

$$s(t) = \varsigma e(t) + \dot{e}(t) \tag{7.30}$$

where $\varsigma > 0$.

The Lyapunov function is selected as below:

$$V_L = \frac{1}{2}s^2 \tag{7.31}$$

Therefore,

$$\dot{s}(t) = \left(\dot{\hat{\alpha}}_2 - \ddot{\alpha}_r\right) + \varsigma(\dot{\hat{\alpha}}_1 - \dot{\alpha}_r) \tag{7.32}$$

By using the designed observer of Equation (7.17) we have,

$$\dot{\hat{\alpha}}_1 = l_1(\alpha_1 - \hat{\alpha}_1) + \hat{\alpha}_2$$

$$\dot{\hat{\alpha}}_2 = \hat{f}_b(\hat{\boldsymbol{\alpha}}) + \hat{g}_b(\hat{\boldsymbol{\alpha}})u_c + l_2(\alpha_1 - \hat{\alpha}_1) - r(t) \tag{7.33}$$

Therefore, by inserting the values from Equation (7.33) in to Equation (7.32) we get,

$$\dot{s}(t) = \hat{f}_b(\hat{\boldsymbol{\alpha}}) + \hat{g}_m(\hat{\boldsymbol{\alpha}})u_c + l_2(\alpha_1 - \hat{\alpha}_1) - r(t) - \ddot{\alpha}_r \\ + \varsigma((l_1(\alpha_1 - \hat{\alpha}_1) + \hat{\alpha}_2) - \dot{\alpha}_r)$$

Therefore, for ensuring $\dot{V}_L = s\dot{s} < 0$, the sliding mode controller input is designed as follows:

$$u_c = \frac{1}{\hat{g}_b(\hat{\boldsymbol{\alpha}})}[-\varsigma(\hat{\alpha}_2 + l_1(\alpha_1 - \hat{\alpha}_1) - \dot{x}_r) - \hat{f}_b(\hat{\boldsymbol{\alpha}}) - r(t) \\ + \ddot{x}_r - l_2(\alpha_1 - \hat{\alpha}_1) - \eta sgns(s)]$$

where η is a constant and $\eta > 0$.

The overall block diagram of the controller is shown in Figure 7.6.

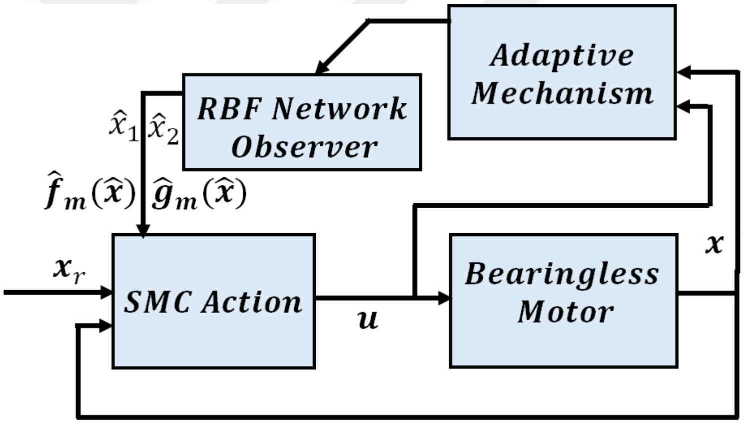

Figure 7.6: The block diagram of the proposed controller for the bearingless motor

7.5 Simulation Results

In order to see the effectiveness of the proposed controller, a simulation is executed using the design parameters which are similar to the experimental prototype setup. The rotor mass is 0.024 kg. The input vector is $[\hat{\alpha}_1 \quad \hat{\alpha}_2]^T$ to the RBF network for α radial direction and $[\hat{\beta}_1 \quad \hat{\beta}_2]^T$ for the β radial direction. The parameters of the RBF are selected as $b_j = 6$ for $j = 1,2,..7$ and $c_{i,j} = \frac{1}{5}[-3 \quad -2 \quad -1 \quad 0 \quad 1 \quad 2 \quad 3]$. Other values are selected as $\boldsymbol{V_1} =$

$diag[700]$, $\boldsymbol{L} = [300\ 600]^T, R = 0.6,\ a_1 = a_2 = 0.003,$ $\boldsymbol{V_2} = diag[0.5],$ $\boldsymbol{\alpha}(0) = [-0.75\ 0]^T,$ $\boldsymbol{\beta}(0) = [0\ 0]^T,$ $\widehat{\boldsymbol{\alpha}}(0) = [0.1\ \ 0]^T, \eta = 0.1,$ $\widehat{\boldsymbol{\beta}}(0) = [0.1\ 0]^T,$ $\varsigma = 15.$ The transfer function $T(s)$ given in Equation (7.19) is calculated as:

$$T(s) = \frac{1}{(s^2+300s+600)} \tag{7.35}$$

For the transfer function $T(s)$ to become a strictly proper, the three conditions given as below must be fulfilled:

1. For a value of s which is real, $T(s)$ should be real.
2. There should be no pole of $T(s)$ lying in the right half plane.
3. For a real ω value, $T(s)$ should also be positive, i.e. $\mathrm{Re}[T(j\omega)] \geq 0$.

Hence, from Equation (7.35), using a real s, $T(s)$ is real. Also, $T(s)$ has poles as -2.01 and -297.99 which lie in the left half plane. The transfer function real part is $\mathrm{Re}[T(j\omega)] = \frac{-(-600+\omega^2)}{((\omega^2-600)^2+90000\omega^2)}$, which can have negative values for real values of the angular frequency ω, therefore the transfer function $T(s)$ is not strictly proper. Hence, from Equation (7.18b), $G^{-1}(s)$ is selected as $\frac{1}{s+2}$ in order to make $G(s)T(s)$ a strictly proper transfer function. Therefore,

$$Y(s) = T(s)\ G(s) = \frac{s+2}{(s^2+300s+600)}$$

The terms $\hat{\boldsymbol{v}}_{\boldsymbol{f}}(\widehat{\boldsymbol{\alpha}})$ and $\hat{\boldsymbol{v}}_{\boldsymbol{g}}(\widehat{\boldsymbol{\alpha}})$ in Equation (22) are computed as follows:

$$\hat{\hat{\boldsymbol{v}}}_{\boldsymbol{f}}(\widehat{\boldsymbol{\alpha}}) = \frac{1}{s+2}\hat{\boldsymbol{v}}_f(\widehat{\boldsymbol{\alpha}}) \text{ and } \hat{\hat{\boldsymbol{v}}}_{\boldsymbol{g}}(\widehat{\boldsymbol{\alpha}}) = \frac{1}{s+2}\hat{\boldsymbol{v}}_g(\widehat{\boldsymbol{\alpha}})$$

Figure 7.7 shows the two state variables and their estimates with the proposed controller along the α radial direction.

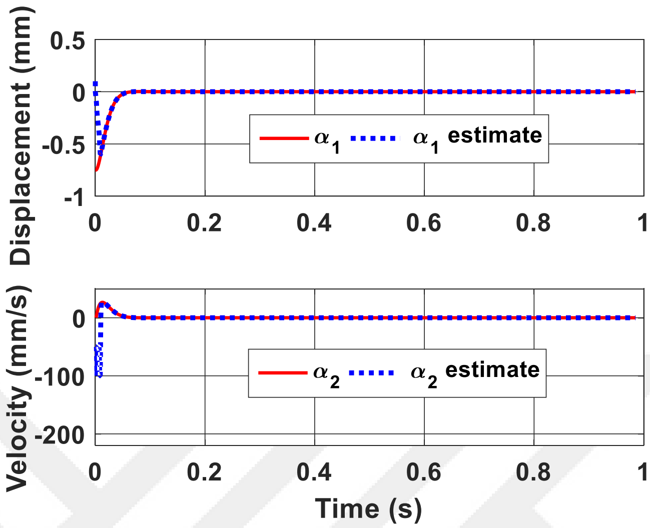

Figure 7.7: The states α_1 and α_2 and their estimated values utilizing the proposed controller

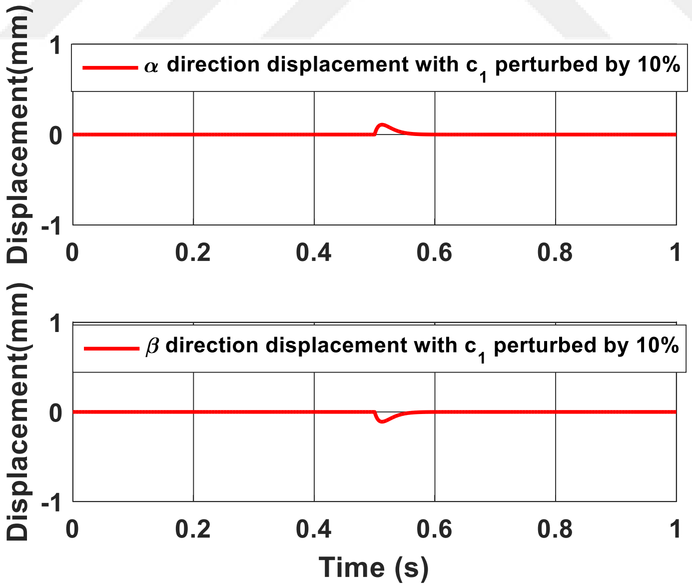

Figure 7.8: Output displacement of the rotor in the α and β directions as a result of perturbation in the parameter c_1

In order to see the robustness of the proposed controller, the parameters of the system model are varied and the resulting output response of the bearingless motor is obtained. The parameter c_1 is changed by 10% when the time is equal to 0.5 seconds. The output displacement of the rotor in the radial direction is shown in Figure 7.8.

The mass of the rotor is changed from nominal value to half and double and the resulting output displacement of the rotor in the α direction is shown in Figure 7.9.

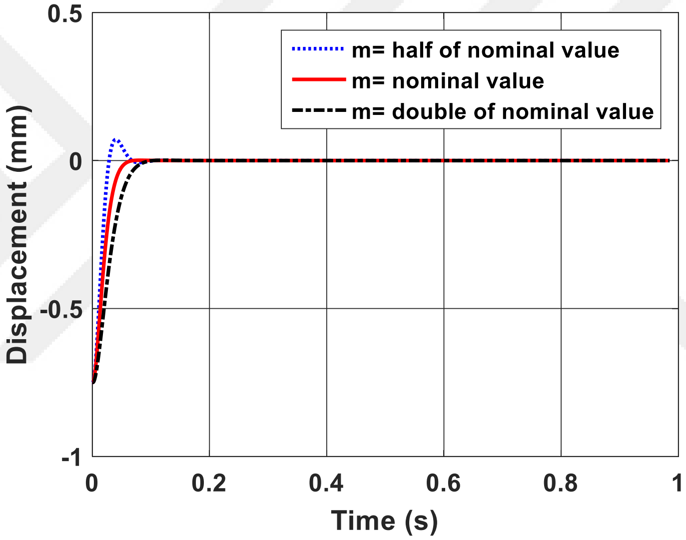

Figure 7.9: Response when the mass of the rotor is varied between half and double of the nominal value

In the similar fashion, the other parameters such as c_2, c_3, and L_{To} were varied and the output remained bounded for the variation of the parameters showing good robustness. A sinusoidal disturbance is included to the system with 10 Hz frequency and the output responses is shown in Figure 7.10. Also, a Gaussian noise with SNR of 10 is included to the system and output is shown in Figure 7.11.

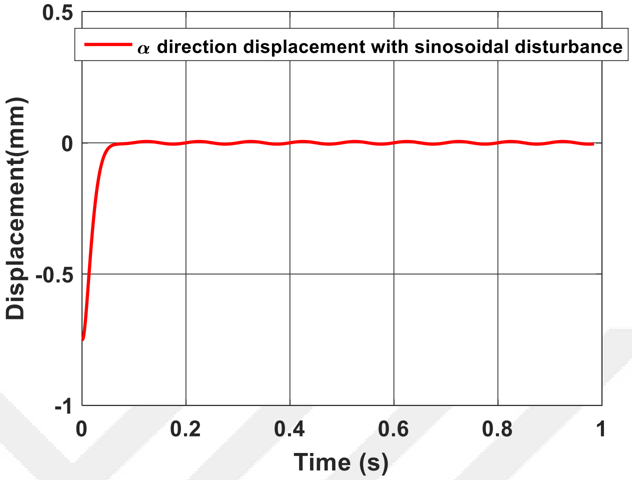

Figure 7.10: Output of the rotor in the α direction with a 10 Hz sinusoidal disturbance added to the system

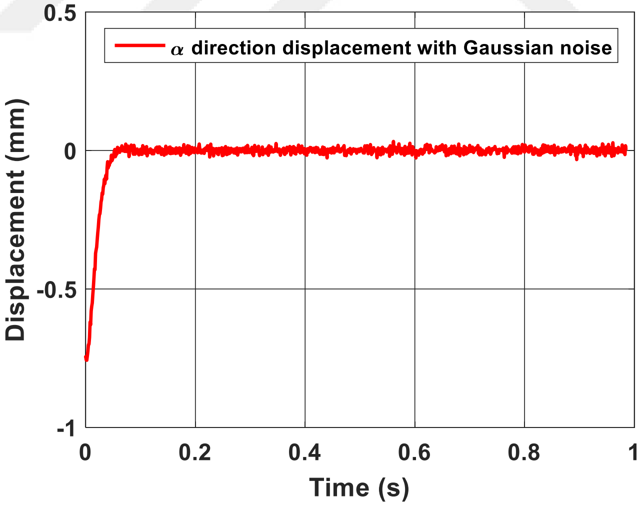

Figure 7.11: Output of the rotor in the α direction with Gaussian noise included

The phase plane trajectories of the error and the change in error are shown in Figure in 7.12 and Figure 7.13.

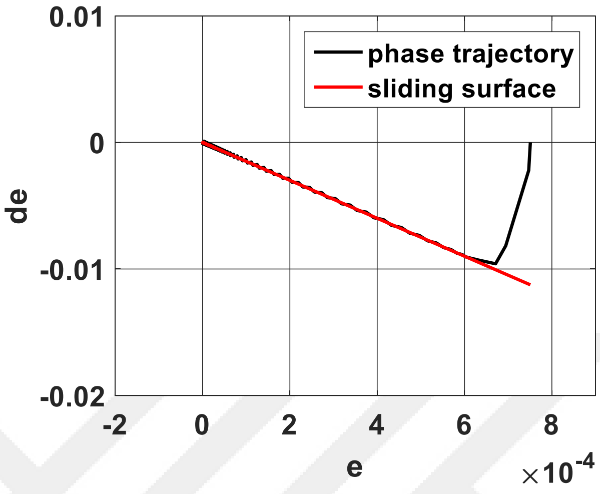

Figure 7.12: Phase plane trajectory of the rotor with the sinusoidal disturbance included in the system

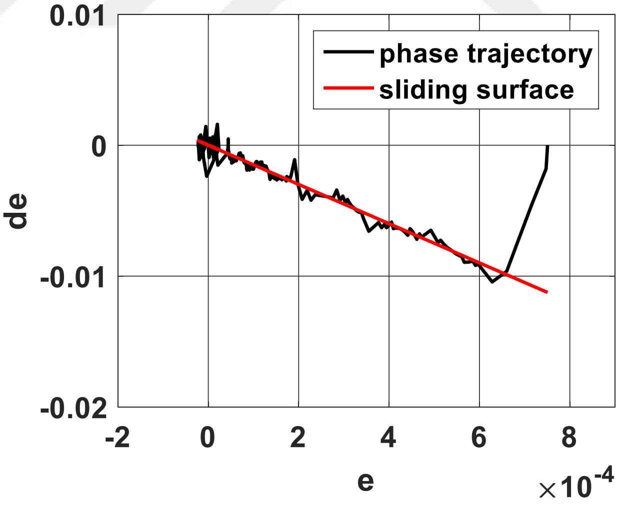

Figure 7.13: Phase plane trajectory of the rotor with the Gaussian random noise included in the system

The performance of the designed controller is compared with a PID controller. The parameter values for the PID controller are K_p= 13, K_i = 27 and K_d = 0.75. In order to compare the disturbance rejection capability of the designed controller with the PID controller, a constant disturbance force of 3.6 N is included to the system at time t= 0.7 seconds.

As a result, the corresponding outputs of the designed controller in the α and β directions are shown in Figure 7.14 while the response with the PID is shown in Figure 7.15. The designed controller's response contains an overshoot of 0.039 mm in the α direction and overshoot of -0.014 mm in the β direction with a settling time equal to 0.073 seconds.

The PID controller response contains an overshoot of 0.057 mm in the α direction and overshoot of -0.031 mm in the β direction with a settling time equal to 0.143 seconds.

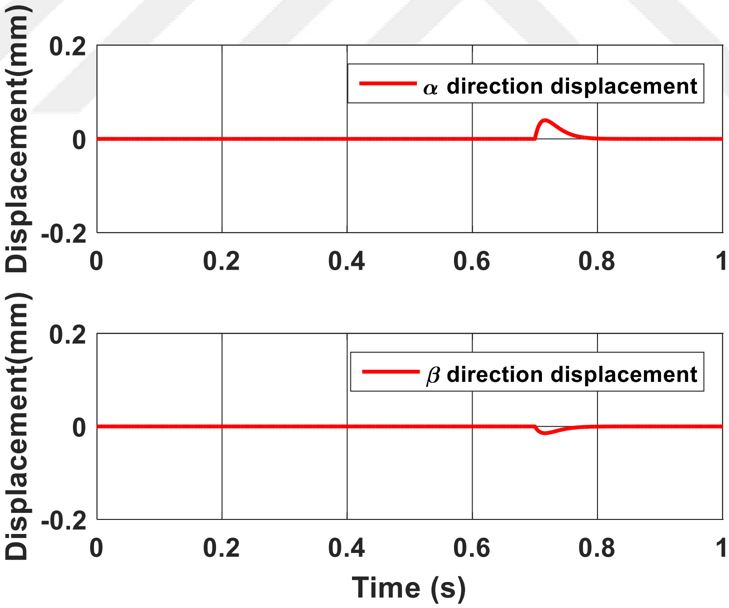

Figure 7.14: Output displacements of the rotor with the designed controller along α and β directions as result of constant disturbance of 3.6 N applied at 0.7 s

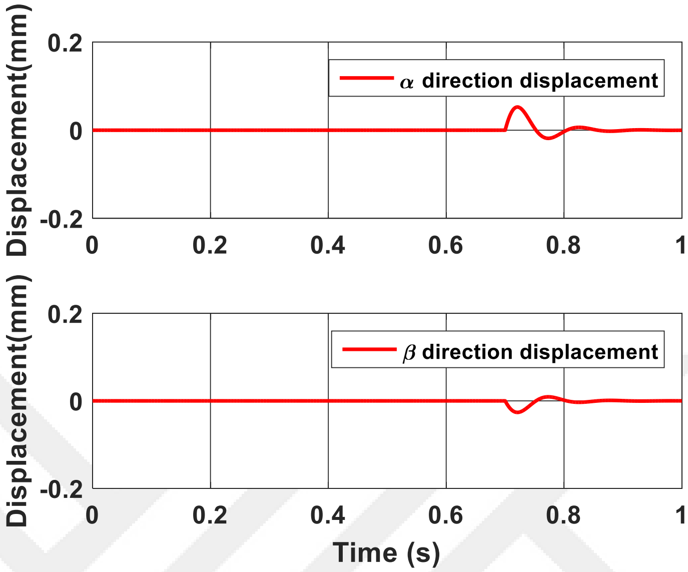

Figure 7.15: Output displacements of the rotor with the PID controller along α and β directions as result of constant disturbance of 3.6 N applied at 0.7 s

The desired position of the α direction is changed to 0.1 mm from 0 mm at the time step of 1 seconds and the output of the two control schemes is simulated. With the designed adaptive controller, there is no overshoot in the α direction. While with the PID controller, there is an overshoot of 0.131 mm in the α direction.

The settling time for the designed adaptive controller is 0.049 s while for the PID controller the settling time is 0.171 s. Along the β direction, there is no variation in the position using the designed adaptive controller while with the PID controller there is an overshoot of -0.034 mm along the β direction.

Therefore, the designed adaptive controller is much better than the PID controller. Figure 7.16 is showing the output response with the designed adaptive controller and Figure 7.17 is showing the output response with the PID controller.

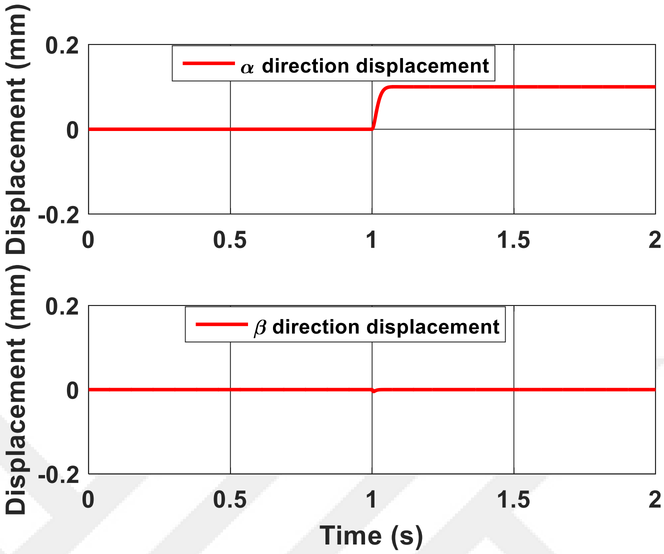

Figure 7.16: Output response with proposed adaptive controller

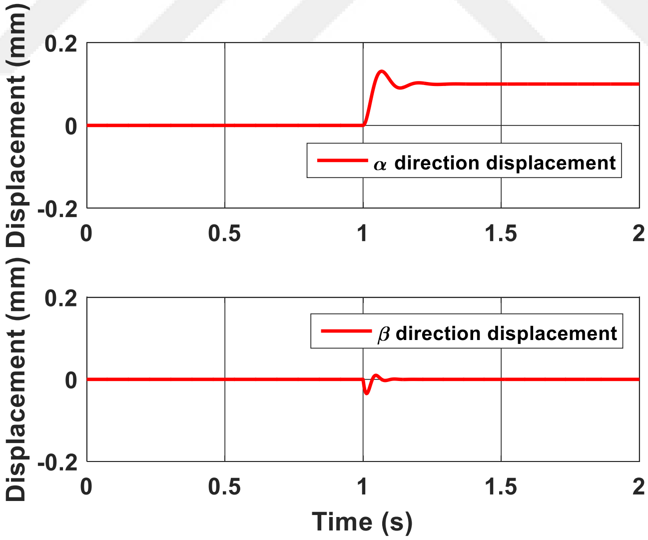

Figure 7.17: Output response with the PID controller

7.6 Experimental Results

For verifying the design process an experimental setup was manufactured as shown in Figure 7.18/

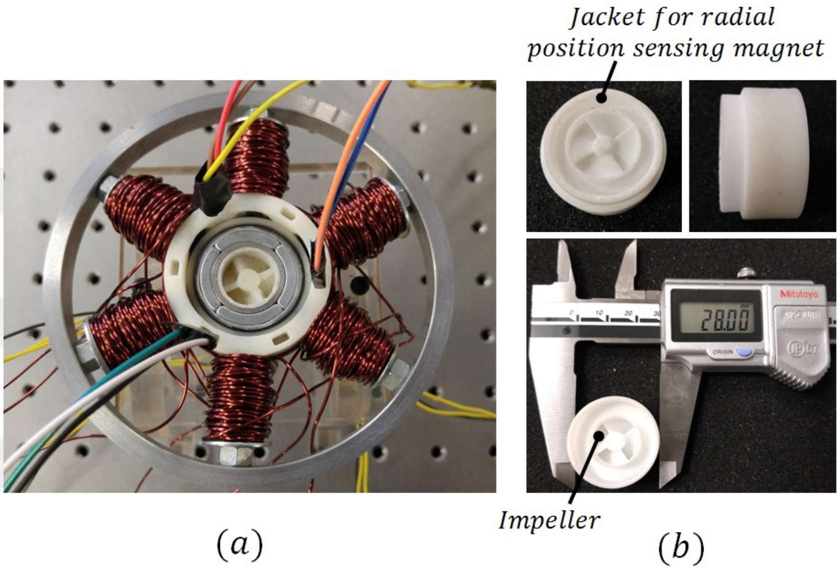

Figure 7.18: (a) Experimental prototype setup (b) Various views of the manufactured rotor system

The rotor is consisted of back iron, impeller, one permanent magnet ring for the generation of the bearing forces and another permanent ring for sensing the radial position of the rotor. There are six stator poles and four rotor poles. The radial bearing force winding is connected in two pole configuration while the motoring torque winding is connected in the four pole configuration. The N48 grade NdFeB permanent magnets have been used in the rotor part. The rotor is axially 12.5 mm long. The outer diameter of the stator part is 70 mm while the outer diameter of the rotor part is 28 mm. Figure 7.19 shows the overall block diagram of the radial direction position and motoring torque control scheme.

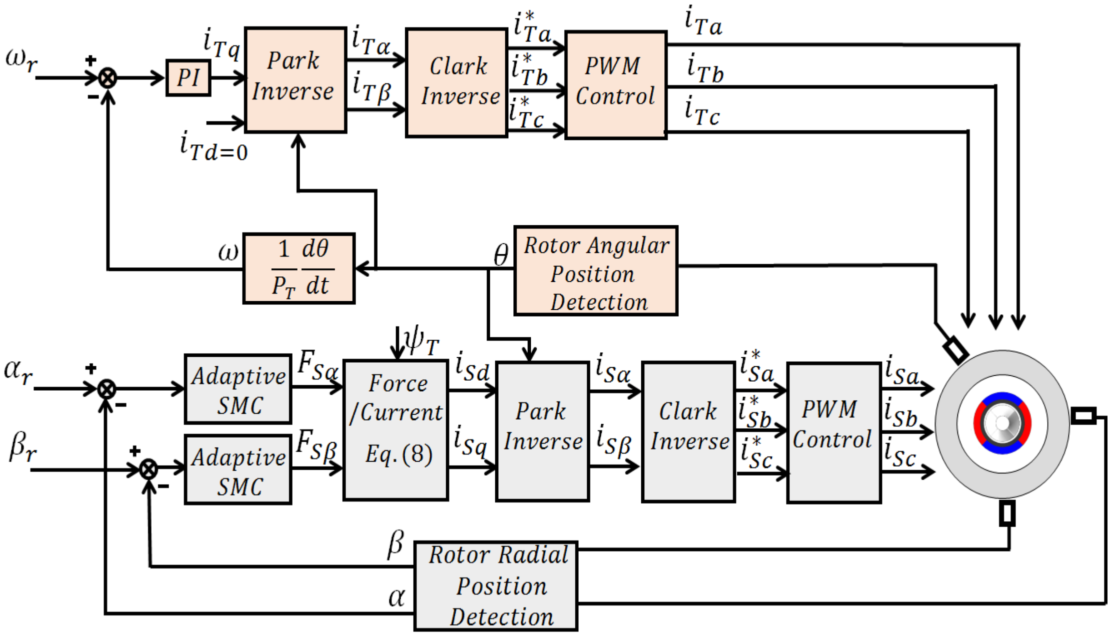

Figure 7.19: The complete block diagram for the motoring torque and radial position control of the proposed bearingless motor

The radial airgap is 0.75 mm. Three Hall effect sensors Allegro A1324 are utilized for measuring the angular displacement of the rotor. Four Allegro Hall effect sensors A3124 are used for measuring the radial position of the rotor system. The passive stiffness of the rotor in the axial direction is calculated as 5.1 N/mm. A maximum of 21.5 N force is needed in the initial startup of the motor to move the rotor to the center position when it touches one side of the stator. The number of windings for the radial bearing force windings and for the motoring torque windings is 60. Low carbon steel AISI-1010 is utilized in order to manufacture the back iron for the rotor and the stator part. A 200 MHz TMSF28377S digital signal processor is utilized for implanting the designed controller. For measuring the current of the radial bearing windings and the motoring torque windings, current sensors A758 are used. A power module FSBB30CH60C is used for driving the motoring torque windings and one FSBB30CH60C power module is used for driving the radial bearing force windings. The power modules are driven with a PWM voltage having frequency of 20 kHz. Figure 7.20 shows the initial startup response of the rotor from rest. A current of 3.7 A is needed to move the rotor to the center from the rest position.

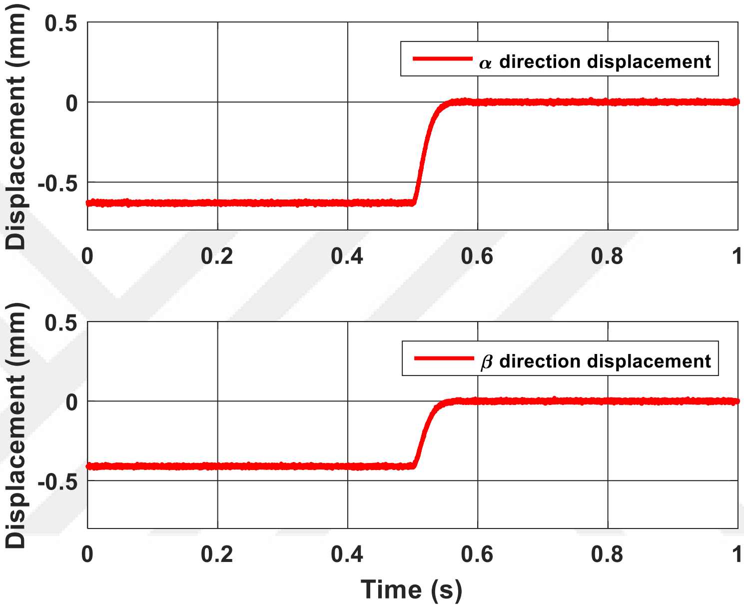

Figure 7.20: The radial position response at the initial startup of the motor

The rotor is rotated at 9800 rpm as required by the application of the axial flow blood pump. Figure 7.21 shows the oscillations of the rotor in the radial direction when only the radial bearing force windings are excited with average peak to peak oscillations of 0.009 mm. Figure 7.22 shows the oscillations of the rotor system in the radial direction when both the radial bearing force windings and the motoring torque windings are excited at an operating speed of 9800 rpm with average peak to peak oscillations of 0.023 mm.

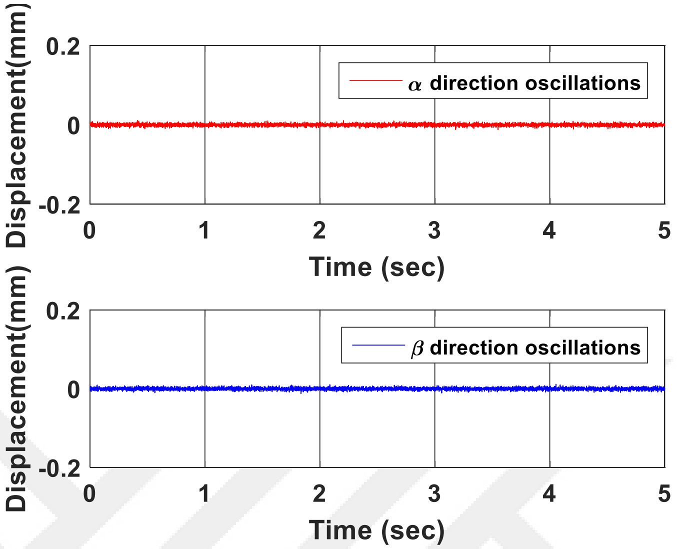

Figure 7.21: Radial oscillations of the rotor with only radial bearing force windings excited

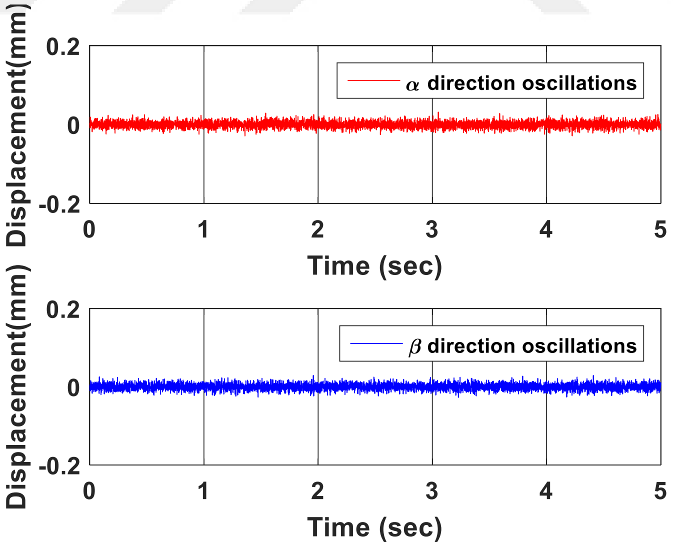

Figure 7.22: Radial oscillations of the rotor with both the radial bearing force windings and the motoring torque windings excited

The response of the proposed controller is compared with the PID controller. The reference position of the α direction is suddenly varied to 0.1 mm from 0 mm. The rotor in case of the designed controller goes to the new reference position 0.053 seconds as compared to the 0.163 seconds for the PID controller. There is no overshoot in case of the response with the designed adaptive controller while there is an overshoot of 0.156 mm in case of response with the PID controller. Also, the average oscillations in case of the proposed controller is 0.023 mm while the PID controller response has oscillations of 0.041 mm. Figure 7.23 shows the output displacements in the radial direction with the designed adaptive controller while Figure 7.24 shows the results with the PID controller.

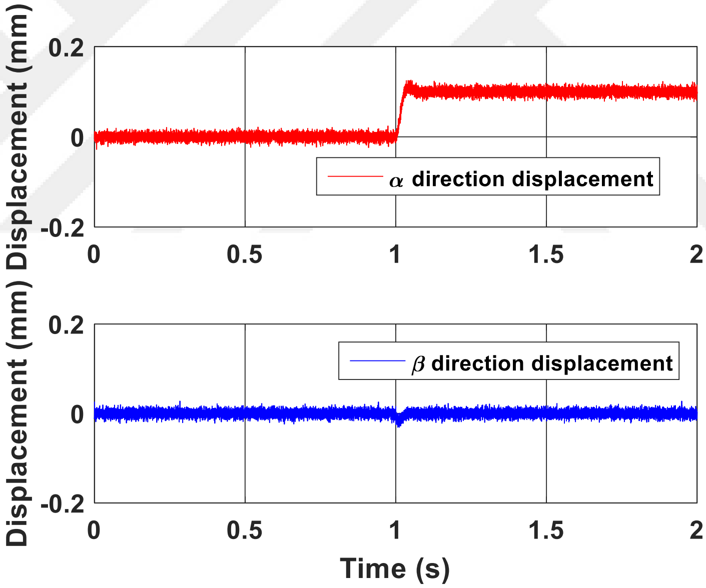

Figure 7.23: Output radial displacements along the α and β directions with the proposed adaptive controller

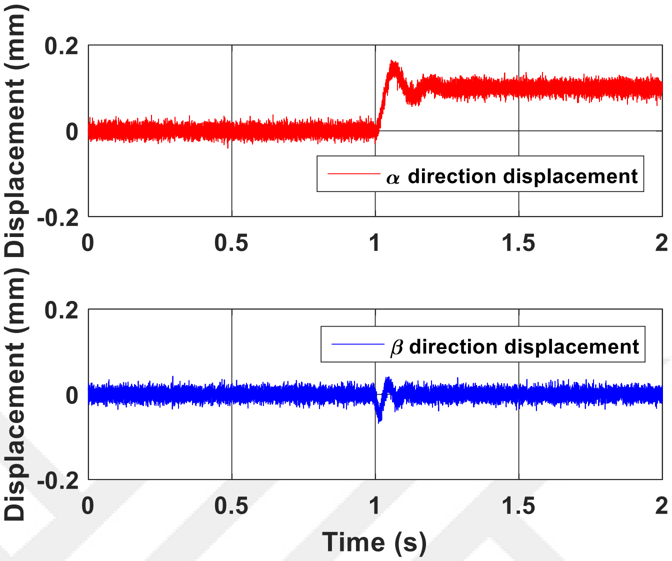

Figure 7.24: Output radial displacements along the α and β directions with the PID controller

A step disturbance force having magnitude of 3.6 N is applied at the time step of 0.7 second. The corresponding responses with the proposed adaptive controller and the PID controller are shown in Figure 7.25 and Figure 7.26 respectively. There is an overshoot of 0.043 mm in the α direction and -0.014 mm in the β direction and having a 0.083 second settling time. With the PID controller, the α direction overshoot is 0.067 mm and the β direction overshoot is -0.041 mm having a settling time of 0.159 seconds. The average oscillations with the adaptive controller are 0.009 mm while the average oscillations with the PID controller are 0.021 mm.

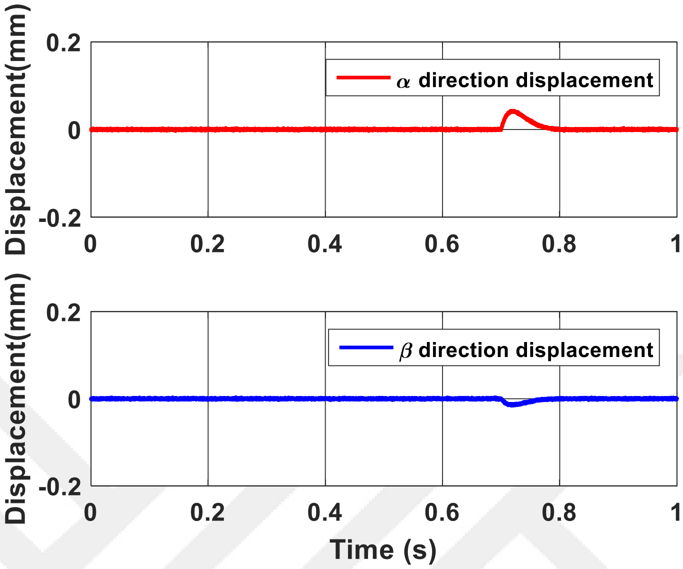

Figure 7.25: α and β directions output responses with the designed SMC controller

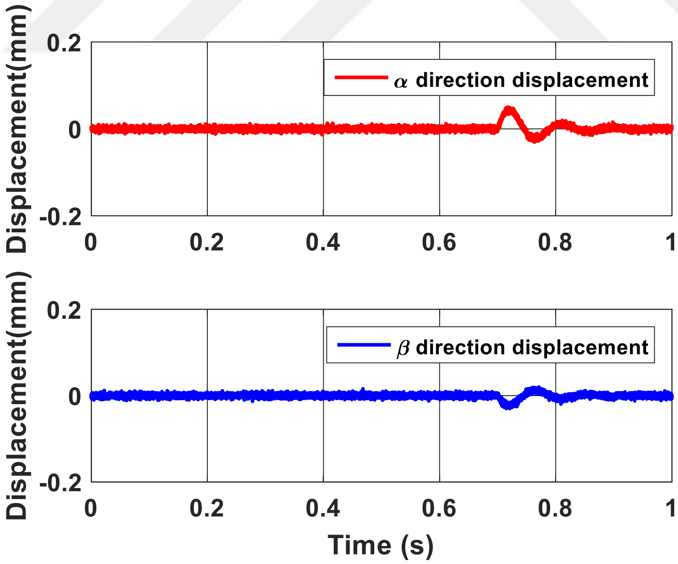

Figure 7.26: α and β directions output responses with the PID controller

7.7 Summary

In this chapter, a sliding mode controller is designed based on the adaptive approximation of the system input function and the system dynamics. The linear Hall effect sensors are used for measuring the rotor radial direction displacement. Digital Hall effect sensors are used for the measurement of the angular displacement of the rotor. Two separate permanent magnet rings have been installed in the rotor. One permanent magnet ring is used to produce the radial bearing forces and the motoring torque. Another permanent magnet ring which is radially magnetized is installed in the rotor to measure the rotor radial direction displacement. There is strong nonlinearity and magnetic coupling present between the two permanent magnet rings. Therefore, for the accurate measurement of the radial position in the presence of disturbances, a radial position observer is first designed based on the RBF network. An adaptive sliding mode controller is then designed based on this observer. The designed controller is simulated and the tested on the experimental setup. The designed controller performance is compared with the PID controller. The comparison results show better position tracking and external interference rejection for the designed sliding mode controller as compared to the PID controller.

Chapter 8
CONCLUSION

Magnetic bearings are applied in high speed motors, molecular pumps, moment wheels, ventricular assist devices and flywheel energy storage systems. They have the main advantages of lower friction, less power consumption and lower heat generation. Magnetic bearings have two types, active magnetic bearings and passive magnetic bearings. The combination of these two types is called hybrid magnetic bearings.

For the design of hybrid magnetic bearings, generally the magnetic circuit method is used. However, in this method the leakage flux, eddy currents and nonlinearities are ignored. Therefore, in this research the finite element method (FEM) was applied for designing the hybrid magnetic bearing prototype system. The geometric parameters of the hybrid magnetic bearing prototype were optimized using the FEM analysis. The stiffness, magnetic flux, currents, number of turns, and forces in the axial and radial direction were computed using the FEA analysis. A brushless DC motor was designed for the prototype setup for rotating the shaft around the axial axis. Based on the optimized parameters, the prototype setup was manufactured. The magnetic properties, stiffness and damping of the designed prototype setup were experimentally verified.

The control of the magnetic bearings in the presence of uncertainties in the system dynamics, external interferences and noise is critical problem. Active magnetic bearing system is unstable in the open loop. The classical control techniques do not provide robust performance against these disturbances and parameter variations. Therefore, for the active control of the hybrid magnetic prototype, an adaptive sliding mode controller was designed. The prototype was stabilized passively in the radial direction while in the axial direction, it was stabilized using the adaptive controller. The controller performance was simulated for different test conditions and also was compared with the PID controller. The controller was then applied to the experimental setup and the performance of the designed controller was then verified experimentally.

The second-generation blood pumps suffer from the problem of blood clotting and hemolysis. For this purpose, third-generation blood pumps with magnetic bearings are used instead of the mechanical bearings. The third-generation axial flow blood pumps require at least two magnetic bearings units in addition to drive unit for the proper operation because of their longer dimensions in the axial direction. In this research, optimized design of the axial flow pump was used based on the optimization performed using the computational fluid dynamics analysis. An enclosed impeller based rotor was used whose axial length was only 12.5 mm. Only one bearingless motor was needed therefore due to the reduced axial length of the rotor. Generally, Hall Effect sensors are utilized for the measurement of the angular position of the rotor while Eddy current sensors are utilized for the measurement of the radial position of the rotor in the bearingless motors. Due to the miniaturized structure of the proposed bearingless motor, eddy current sensors were not possible to be used. Therefore, a novel design of the rotor for the pump was proposed, in which there were two permanent magnet rings used. One ring was used for the generation of the radial bearing forces and another ring was used for the radial direction position measurement of the rotor. A sensor assembly based upon the linear Hall effect sensors was proposed for measuring the rotor radial position. The FEM analysis of the overall novel design of the pump was performed and the magnetic properties, stiffness and forces were computed.

An experimental prototype of the proposed novel design bearingless motor was manufactured and the functionality of the novel sensor assembly was experimentally tested and verified. The different properties of the motor system as experimentally tested and compared with the simulation results. The experimental results had a good agreement with the simulation results. As there are two permanent magnet rings installed in the rotor with a close proximity, there exists a magnetic coupling and interference to the sensor assembly.

Therefore, for the accurate radial position in the presence of the interferences and noise, the designed adaptive sliding mode controller was applied to the position control of the bearingless motor. The system dynamics and the input function were first estimated using the adaptive observer and based on the observer, a sliding mode controller was designed for the position control of the system. The performance of the designed controller was also compared with the PID controller. The designed adaptive controller showed better position tracking, less oscillations and better disturbance rejection ability as compared to the PID controller. The designed controller was applied to the experimental prototype setup of the bearingless motor and the performance of the motor system was assessed under various test conditions.

BIBLIOGRAPHY

[1] M. Granström, "Design and Analysis of a 1-DOF magnetic bearing," Master of Science, KTH Industrial Engineering and Management, KTH Royal Institute of Technology in Stockholm, Sweden, 2011.

[2] H. Bleuler *et al.*, *Magnetic bearings: theory, design, and application to rotating machinery*. Springer Science & Business Media, 2009.

[3] D. Q. Nguyen and V. H. Thourani, "Third-generation continuous flow left ventricular assist devices," *Innovations: Technology and Techniques in Cardiothoracic and Vascular Surgery,* vol. 5, no. 4, pp. 250-258, 2010.

[4] H. Wu, Z. Wang, and X. Lv, "Design and simulation of axial flow maglev blood pump," *International Journal of Information Engineering and Electronic Business,* vol. 3, no. 2, p. 42, 2011.

[5] T. P. Dever, G. V. Brown, K. P. Duffy, and R. H. Jansen, "Modeling and development of a magnetic bearing controller for a high speed flywheel system," *AIAA Paper,* no. 2004-5626, 2004.

[6] B. C. D. Wilson, "Control Designs for Low-Loss Active Magnetic Bearing: Theory and Implementation," Georgia Institute of Technology, 2004.

[7] F. Zurcher, T. Nussbaumer, W. Gruber, and J. W. Kolar, "Comparison of 2-and 3-phase bearingless slice motor concepts," in *11th Int. Symp. Magn. Bearings, Nara, Japan*, 2008.

[8] Q. Li, P. Boesch, M. Haefliger, J. W. Kolar, and D. Xu, "Basic characteristics of a 4kW permanent-magnet type bearingless slice motor for centrifugal pump system," in *Electrical Machines and Systems, 2008. ICEMS 2008. International Conference on*, 2008, pp. 3037-3042: IEEE.

[9] S. Cheng and S. W. Day, "Design and control of hybrid magnetic bearings for maglev axial flow blood pump," in *Advanced Intelligent Mechatronics (AIM), 2010 IEEE/ASME International Conference on*, 2010, pp. 187-192: IEEE.

[10] A. Traxler, "Eigenschaften und Auslegung von berührungsfreien elektromagnetischen Lagern," 1986.

[11] S. Earnshaw, "On the nature of the molecular forces which regulate the constitution of the luminiferous ether," *Trans. Camb. Phil. Soc,* vol. 7, pp. 97-112, 1842.

[12] W. Braunbek, "Freischwebende Körper im elektrischen und magnetischen Feld," *Zeitschrift für Physik A Hadrons and Nuclei,* vol. 112, no. 11, pp. 753-763, 1939.

[13] M. V. Berry, "The Levitron $^{\text {TM}} $: an Adiabatic Trap for Spins," in *Proceedings of the Royal Society of London A: Mathematical, Physical and Engineering Sciences*, 1996, vol. 452, no. 1948, pp. 1207-1220: The Royal Society.

[14] M. D. Simon, L. O. Heflinger, and S. Ridgway, "Spin stabilized magnetic levitation," *American Journal of Physics,* vol. 65, no. 4, pp. 286-292, 1997.

[15] R. Gasch and M. Lang, "Levitron—ein Beispiel für die rein permanentmagnetische Lagerung eines Rotors," *ZAMM-Journal of Applied Mathematics and Mechanics/Zeitschrift für Angewandte Mathematik und Mechanik,* vol. 80, no. 2, pp. 137-144, 2000.

[16] M. Lang, "Levitron - an example of gyroscopic stabilization of a rotor," in *8th Int. Symp. on Magn. Susp. Tech. (ISMST)*, Dresden, 2005, pp. pp. 177–181.

[17] M. Lang, "Berechnung und Optimierung von passiven permanentmagnetischen Lagern für rotierende Maschinen," 2003.

[18] A. Geim, M. Simon, M. Boamfa, and L. Heflinger, "Magnet levitation at your fingertips," *Nature,* vol. 400, no. 6742, p. 323, 1999.

[19] H. Kemper, "Overhead suspension railway with wheel-less vehicles employing magnetic suspension from iron rails," *German Patents,* vol. 643316, 1937.

---

[20] H. Kemper, "Schwebende Aufhängung durch elektromagnetische Kräfte: eine Möglichkeit für eine grundsätzlich neue Fortbewegungsart," *ETZ,* vol. 59, pp. 391-395, 1938.

[21] E. Gottzein, L. Miller, and R. Meisinger, "Magnetic suspension control system for high speed ground transportation vehicles," in *Proc. of World Electrotechnical Congress, Moscow*, 1977.

[22] W. Klimek, "A contribution to the measurement technique using electromagnetic suspension," *DLR Forschungsbericht 72,* vol. 30, 1972.

[23] R. Sindlinger, "Magnetic bearing momentum wheels with vernier gimballing capability for 3-axis active attitude control and energy storage," *IFAC Proceedings Volumes,* vol. 9, no. 1, pp. 849-860, 1976.

[24] G. Schweitzer, "Stabilization of self-excited rotor vibrations by an active damper," *Dynamics of rotors,* pp. 472-493, 1975.

[25] H. Habermann and G. Liard, "Le palier magnétique active: un principe révolutionaire," *SKF Rev. Roulements,* no. 192, 1977.

[26] I. fuer. (2004). *Active Magnetic Bearing*. Available: http://www.mdmt.tuwien.ac.at/forschung/magnetlager/

[27] H. Bleuler, "A survey of magnetic levitation and magnetic bearing types," *JSME international journal. Ser. 3, Vibration, control engineering, engineering for industry,* vol. 35, no. 3, pp. 335-342, 1992.

[28] B. Polajžer, J. Ritonja, G. Štumberger, D. Dolinar, and J.-P. Lecointe, "Decentralized PI/PD position control for active magnetic bearings," *Electrical Engineering (Archiv fur Elektrotechnik),* vol. 89, no. 1, pp. 53-59, 2006.

[29] G. Zames, "Feedback and optimal sensitivity: Model reference transformations, multiplicative seminorms, and approximate inverses," *IEEE Transactions on automatic control,* vol. 26, no. 2, pp. 301-320, 1981.

---

[30] R. Herzog and H. Bleuler, "Stiff AMB control using an H∞ approach," in *Proc. 2nd Int. Symp. Magnetic Bearings*, 1990, pp. 343-348.

[31] M. Fujita, F. Matsumuro, and M. Shimizu, "H-Infinity Robust Control Design for a Magnetic Suspension System," in *Proceedings of the Second international Symposium on Magnetic Bearings, Tokyo, Japan*, pp. 349-356.

[32] D. Vischer, "Sensorlose und spannungsgesteuerte Magnetlager," ETH Zurich, 1988.

[33] D. Vischer and H. Bleuler, "Self-sensing active magnetic levitation," *IEEE Transactions on Magnetics,* vol. 29, no. 2, pp. 1276-1281, 1993.

[34] D. Visher and H. Bleuler, "A new approach to sensorless and voltage controlled AMB's based on network theory concept," in *Proc. 2nd Int. Symp. Magnetic Bearings*, 1990, pp. 301-306.

[35] A. Schammass, R. Herzog, P. Buhler, and H. Bleuler, "New results for self-sensing active magnetic bearings using modulation approach," *IEEE transactions on control systems technology,* vol. 13, no. 4, pp. 509-516, 2005.

[36] L. Kucera, "Robustness of self-sensing magnetic bearing," *Proceedings of MAG,* vol. 97, pp. 261-270, 1997.

[37] M. D. Noh and E. H. Maslen, "Self-sensing magnetic bearings using parameter estimation," *IEEE Transactions on Instrumentation and Measurement,* vol. 46, no. 1, pp. 45-50, 1997.

[38] Z. Gao, "Scaling and bandwidth-parameterization based controller tuning," in *Proceedings of the American control conference*, 2006, vol. 6, pp. 4989-4996.

[39] J.-Q. Han, "Nonlinear design methods for control systems," *IFAC Proceedings Volumes,* vol. 32, no. 2, pp. 1531-1536, 1999.

[40] B. Su-Alexander, "Control of Active Magnetic Bearings for Flywheel Energy Storage," Cleveland State University, 2006.

[41] R. S. Smith, "Magnetic bearing measurement configurations and associated robustness and performance limitations," 2002.

[42] E. H. Maslen, D. T. Montie, and T. Iwasaki, "Robustness limitations in self-sensing magnetic bearings," *Journal of dynamic systems, measurement, and control,* vol. 128, no. 2, pp. 197-203, 2006.

[43] K. Peterson, R. Middleton, and J. Freudenberg, "Fundamental limitations in self-sensing magnetic bearings when modeled as linear periodic systems," in *American Control Conference, 2006*, 2006, p. 6 pp.: IEEE.

[44] M. Barut, S. Bogosyan, and M. Gokasan, "Speed-sensorless estimation for induction motors using extended Kalman filters," *IEEE Transactions on Industrial Electronics,* vol. 54, no. 1, pp. 272-280, 2007.

[45] T. Schuhmann, W. Hofmann, and R. Werner, "Improving operational performance of active magnetic bearings using Kalman filter and state feedback control," *IEEE Transactions on Industrial Electronics,* vol. 59, no. 2, pp. 821-829, 2012.

[46] R.-J. Wai, J.-D. Lee, and K.-L. Chuang, "Real-time PID control strategy for maglev transportation system via particle swarm optimization," *IEEE Transactions on Industrial Electronics,* vol. 58, no. 2, pp. 629-646, 2011.

[47] O.-S. Kim, S.-H. Lee, and D.-C. Han, "Positioning performance and straightness error compensation of the magnetic levitation stage supported by the linear magnetic bearing," *IEEE Transactions on Industrial Electronics,* vol. 50, no. 2, pp. 374-378, 2003.

[48] C. Liu, G. Liu, and J. Fang, "Feedback Linearization and Extended State Observer-Based Control for Rotor-AMBs System With Mismatched Uncertainties," *IEEE Transactions on Industrial Electronics,* vol. 64, no. 2, pp. 1313-1322, 2017.

[49] D. Traoré, F. Plestan, A. Glumineau, and J. de Leon, "Sensorless induction motor: High-order sliding-mode controller and adaptive interconnected observer," *IEEE Transactions on Industrial Electronics,* vol. 55, no. 11, pp. 3818-3827, 2008.

[50] C. Lascu and G.-D. Andreescu, "Sliding-mode observer and improved integrator with DC-offset compensation for flux estimation in sensorless-controlled induction motors," *IEEE Transactions on Industrial Electronics,* vol. 53, no. 3, pp. 785-794, 2006.

[51] L. Zhao, J. Huang, H. Liu, B. Li, and W. Kong, "Second-order sliding-mode observer with online parameter identification for sensorless induction motor drives," *IEEE Transactions on Industrial Electronics,* vol. 61, no. 10, pp. 5280-5289, 2014.

[52] Y. Feng, J. Zheng, X. Yu, and N. V. Truong, "Hybrid terminal sliding-mode observer design method for a permanent-magnet synchronous motor control system," *IEEE Transactions on Industrial Electronics,* vol. 56, no. 9, pp. 3424-3431, 2009.

[53] J. Fei and H. Ding, "Adaptive sliding mode control of dynamic system using RBF neural network," *Nonlinear Dynamics,* vol. 70, no. 2, pp. 1563-1573, 2012.

[54] J. Fei and C. Lu, "Adaptive Sliding Mode Control of Dynamic Systems Using Double Loop Recurrent Neural Network Structure," *IEEE Transactions on Neural Networks and Learning Systems,* 2017.

[55] J. Fei and W. Yan, "Adaptive control of MEMS gyroscope using global fast terminal sliding mode control and fuzzy-neural-network," *Nonlinear Dynamics,* vol. 78, no. 1, pp. 103-116, 2014.

[56] J. Baek, M. Jin, and S. Han, "A new adaptive sliding-mode control scheme for application to robot manipulators," *IEEE Transactions on Industrial Electronics,* vol. 63, no. 6, pp. 3628-3637, 2016.

[57] J. Lee, P. H. Chang, and M. Jin, "Adaptive integral sliding mode control with time-delay estimation for robot manipulators," *IEEE Transactions on Industrial Electronics,* vol. 64, no. 8, 2017.

[58] M.-J. Jang, C.-L. Chen, and Y.-M. Tsao, "Sliding mode control for active magnetic bearing system with flexible rotor," *Journal of the Franklin Institute,* vol. 342, no. 4, pp. 401-419, 2005.

[59] Y.-W. Tsai and V. A. Duong, "Sliding mode control for active magnetic bearings of a flywheel energy storage system," in *Control and Robotics Engineering (ICCRE), 2016 IEEE International Conference on*, 2016, pp. 1-5: IEEE.

[60] S.-Y. Chen and F.-J. Lin, "Robust nonsingular terminal sliding-mode control for nonlinear magnetic bearing system," *IEEE Transactions on Control Systems Technology,* vol. 19, no. 3, pp. 636-643, 2011.

[61] E. Whittle, A. Noshadi, J. Shi, and A. Kalam, "Experimental study on servo linear quadratic Gaussian and observer-based sliding mode control for active magnetic bearing system," in *Power Engineering Conference (AUPEC), 2015 Australasian Universities*, 2015, pp. 1-6: IEEE.

[62] R. Bosch, "Development of a bearingless electric motor," in *ICEM*, 1988, pp. 373-375.

[63] A. O. Salazar, W. Dunford, R. Stephan, and E. Watanabe, "A magnetic bearing system using capacitive sensors for position measurement," *IEEE Transactions on Magnetics,* vol. 26, no. 5, pp. 2541-2543, 1990.

[64] A. O. Salazar and R. Stephan, "A bearingless method for induction machines," *IEEE Transactions on Magnetics,* vol. 29, no. 6, pp. 2965-2967, 1993.

[65] A. Chiba, M. A. Rahman, and T. Fukao, "Radial force in a bearingless reluctance motor," *IEEE Transactions on Magnetics,* vol. 27, no. 2, pp. 786-790, 1991.

[66] A. Chiba, "Principles and characteristics of a reluctance motor with windings of magnetic bearing," *IPEC-Tokyo, 1990,* 1990.

[67] A. Chiba, D. Power, and M. Rahman, "No load characteristics of a bearingless induction motor," in *Industry Applications Society Annual Meeting, 1991., Conference Record of the 1991 IEEE*, 1991, pp. 126-132: IEEE.

[68] K. Dejima, T. Ohishi, and Y. Okada, "Analysis and control of a permanent magnet type levitated rotating motor," in *IEEJ Proceedings of Symposium Dynamics of Electro Magnetic Force*, 1992, pp. 251-256.

[69] J. Bichsel, "The bearingless electrical machine," 1992.

[70] M. A. Preston, J. P. Lyons, E. Richter, and K. Chung, "Integrated magnetic bearing/switched reluctance machine," ed: Google Patents, 1995.

[71] M. Takemoto, H. Suzuki, A. Chiba, and T. Fukao, "A method of generating current command in bearingless switched reluctance motors," in *1999 National Convention Record of the IEE Japan*, 1999, no. 1147, pp. 5-187-5-188.

[72] K. Shimada, M. Takemoto, A. Chiba, and T. Fukao, "A stable rotation in switched reluctance type bearingless motors," in *IEEJ Technical Meeting on Linear Drive*, 1997, vol. 550.

[73] M. Takemoto and T. Fukao, "A design and characteristics of switched reluctance type bearingless motors," in *NASA CONFERENCE PUBLICATION*, 1998, pp. 49-66: NASA.

[74] M. Oshima, S. Miyazawa, T. Deido, A. Chiba, F. Nakamura, and T. Fukao, "Characteristics of a permanent magnet type bearingless motor," *IEEE Transactions on Industry Applications,* vol. 32, no. 2, pp. 363-370, 1996.

[75] M. Ooshima, A. Chiba, T. Fukao, and M. A. Rahman, "Design and analysis of permanent magnet-type bearingless motors," *IEEE Transactions on Industrial Electronics,* vol. 43, no. 2, pp. 292-299, 1996.

[76] M. Ooshima, S. Miyazawa, A. Chiba, F. Nakamura, and T. Fukao, "A rotor design of a permanent magnet-type bearingless motor considering demagnetization," in *Power Conversion Conference-Nagaoka 1997., Proceedings of the*, 1997, vol. 2, pp. 655-660: IEEE.

[77] H.-M. Chin and L. S. Stephens, "Closed Loop Performance of a Slotless Lorentz Self-Bearing Motor," in *ASME Turbo Expo 2003, collocated with the 2003 International Joint Power Generation Conference*, 2003, pp. 583-591: American Society of Mechanical Engineers.

[78] L. S. Stephens and D.-G. Kim, "Force and torque characteristics for a slotless Lorentz self-bearing servomotor," *IEEE transactions on magnetics,* vol. 38, no. 4, pp. 1764-1773, 2002.

[79] F. Wang and L. Xu, "Calculation and measurement of radial and axial forces for a bearingless PMDC motor," in *Industry Applications Conference, 2000. Conference Record of the 2000 IEEE*, 2000, vol. 1, pp. 249-252: IEEE.

[80] W. Amrhein, S. Silber, and K. Nenninger, "Levitation forces in bearingless permanent magnet motors," *IEEE Transactions on Magnetics,* vol. 35, no. 5, pp. 4052-4054, 1999.

[81] Y. Okada, K. Dejima, and T. Ohishi, "Radial position control of a PM synchronous type and induction type rotating motor," in *Industry Applications Society Annual Meeting, 1994., Conference Record of the 1994 IEEE*, 1994, vol. 2, pp. 234-239: IEEE.

[82] Y. Okada, K. Dejima, and T. Ohishi, "Analysis and comparison of PM synchronous motor and induction motor type magnetic bearings," *IEEE Transactions on Industry Applications,* vol. 31, no. 5, pp. 1047-1053, 1995.

[83] D. Dorrell, M. Ooshima, and A. Chiba, "Force analysis of a buried permanent-magnet bearingless motor," in *Electric Machines and Drives Conference, 2003. IEMDC'03. IEEE International*, 2003, vol. 2, pp. 1091-1097: IEEE.

[84] M. Ooshima, A. Chiba, A. Rahman, and T. Fukao, "An improved control method of buried-type IPM bearingless motors considering magnetic saturation and magnetic pull variation," *IEEE Transactions on Energy Conversion,* vol. 19, no. 3, pp. 569-575, 2004.

[85] K. Inagaki, A. Chiba, M. A. Rahman, and T. Fukao, "Performance characteristics of inset-type permanent magnet bearingless motor drives," in *Power Engineering Society Winter Meeting, 2000. IEEE*, 2000, vol. 1, pp. 202-207: IEEE.

[86] Y. Okada, S. Miyamoto, and T. Ohishi, "Levitation and torque control of internal permanent magnet type bearingless motor," *IEEE Transactions on Control Systems Technology,* vol. 4, no. 5, pp. 565-571, 1996.

[87] B. Wang, Z. Wang, and F. Wang, "Levitation forces control by current vector orientation for a bearingless motor with hybrid rotor structure," in *Electrical and Computer Engineering, 2003. IEEE CCECE 2003. Canadian Conference on*, 2003, vol. 1, pp. 383-386: IEEE.

[88] F. Wang, B. Wang, and L. Xu, "A novel bearingless motor with hybrid rotor structure and levitation force control," in *Industry Applications Conference, 2002. 37th IAS Annual Meeting. Conference Record of the*, 2002, vol. 1, pp. 212-215: IEEE.

[89] M. A. Casemore and L. S. Stephens, "Actuator gains for a toothless permanent-magnet self-bearing motor," *IEEE transactions on magnetics,* vol. 35, no. 6, pp. 4482-4489, 1999.

[90] J. Zhou and K. Tseng, "A disk-type bearingless motor for use as satellite momentum-reaction wheel," in *Power Electronics Specialists Conference, 2002. pesc 02. 2002 IEEE 33rd Annual*, 2002, vol. 4, pp. 1971-1975: IEEE.

[91] T. Reichert, T. Nussbaumer, and J. W. Kolar, "Bearingless 300-W PMSM for bioreactor mixing," *IEEE Transactions on Industrial Electronics,* vol. 59, no. 3, pp. 1376-1388, 2012.

[92] Y. C. Liu, H. Q. Zhu, and L. D. Zhu, "Suspension Force Control System Design and Simulation for Bearingless Brushless DC Motor," in *Applied Mechanics and Materials*, 2015, vol. 703, pp. 250-253: Trans Tech Publ.

[93] H. Grabner, W. Amrhein, S. Silber, and W. Gruber, "Nonlinear feedback control of a bearingless brushless DC motor," *IEEE/ASME transactions on mechatronics,* vol. 15, no. 1, pp. 40-47, 2010.

[94] H. Zhu, C. Wang, E. Tan, T. Li, and X. Ji, "Mathematical model and control technology of bearingless PMSM," in *Control and Decision Conference (CCDC), 2010 Chinese*, 2010, pp. 3175-3179: IEEE.

[95] C. Zhao and H. Zhu, "Design and Analysis of A Novel Bearingless Flux-Switching Permanent Magnet Motor," *IEEE Transactions on Industrial Electronics,* 2017.

[96] T. Reichert, J. W. Kolar, and T. Nussbaumer, "Stator tooth design study for bearingless exterior rotor PMSM," *IEEE Transactions on Industry Applications,* vol. 49, no. 4, pp. 1515-1522, 2013.

[97] M. Ooshima, K. Miyashita, and M. Rahman, "Control circuit topology of a time-divided torque and suspension force control type bearingless motor," in *Power and Energy Society General Meeting, 2012 IEEE*, 2012, pp. 1-4: IEEE.

[98] M. Ooshima, K. Miyashita, and M. Nakagawa, "Magnetic levitation tests of a time-divided torque and suspension force control type bearingless motor," in *Electrical Machines and Systems (ICEMS), 2012 15th International Conference on*, 2012, pp. 1-6: IEEE.

[99] K. Miyashita, M. Ooshima, and M. N. Uddin, "Design of a time-divided torque and suspension force control type bearingless motor," in *Power and Energy Society General Meeting, 2011 IEEE*, 2011, pp. 1-4: IEEE.

[100] M. Ooshima, "Winding arrangement to increase suspension force in bearingless motors with brushless DC structure," in *Industrial Electronics Society, 2007. IECON 2007. 33rd Annual Conference of the IEEE*, 2007, pp. 181-186: IEEE.

[101] M. Bartholet, S. Silber, T. Nussbaumer, and J. Kolar, "Performance investigation of two-, three-and four-phase bearingless slice motor configurations," in *Power Electronics and Drive Systems, 2007. PEDS'07. 7th International Conference on*, 2007, pp. 9-16: IEEE.

[102] H. Grabner, S. Silber, and W. Amrhein, "Bearingless torque motor-modeling and control," in *Proceedings of the 13th International Symposium on Magnetic Bearings (ISMB)*, 2012.

[103] S. Silber, H. Grabner, R. Lohninger, and W. Amrhein, "Design aspects of bearingless torque motors," in *Proc. 13th International Symposium on Magnetic Bearings*, 2012.

[104] H. Mitterhofer, W. Amrhein, and H. Grabner, "Comparison of two and four-pole rotors for a high speed bearingless drive," in *ISMB 2012, The 13th International Symposium on Magnetic Bearings*, 2012.

[105] H. Mitterhofer and W. Amrhein, "Design aspects and test results of a high speed bearingless drive," in *Power Electronics and Drive Systems (PEDS), 2011 IEEE Ninth International Conference on*, 2011, pp. 705-710: IEEE.

[106] H. Mitterhofer, W. Gruber, and W. Amrhein, "On the high speed capacity of bearingless drives," *IEEE Transactions on Industrial Electronics,* vol. 61, no. 6, pp. 3119-3126, 2014.

[107] S. Cheng, M. W. Olles, A. F. Burger, and S. W. Day, "Optimization of a hybrid magnetic bearing for a magnetically levitated blood pump via 3-D FEA," *Mechatronics,* vol. 21, no. 7, pp. 1163-1169, 2011.

[108] S. Cheng, M. W. Olles, D. B. Olsen, L. D. Joyce, and S. W. Day, "Miniaturization of a magnetically levitated axial flow blood pump," *Artificial organs,* vol. 34, no. 10, pp. 807-815, 2010.

[109] T. Masuzawa, T. Kita, K. i. Matsuda, and Y. Okada, "Magnetically Suspended Rotary Blood Pump with Radial Type Combined Motor-Bearing," *Artificial organs,* vol. 24, no. 6, pp. 468-474, 2000.

[110] A. FENERCİOĞLU, "Design and analysis of a magnetically levitated axial flux BLDC motor for a ventricular assist device (VAD)," *Turkish Journal of Electrical Engineering & Computer Sciences,* vol. 24, no. 4, pp. 2881-2892, 2016.

[111] J. J. Lee, C. B. Ahn, J. Choi, J. W. Park, S. J. Song, and K. Sun, "Development of Magnetic Bearing System for a New Third-Generation Blood Pump," *Artificial organs,* vol. 35, no. 11, pp. 1082-1094, 2011.

[112] H. Hoshi, T. Shinshi, and S. Takatani, "Third-generation Blood Pumps With Mechanical Noncontact Magnetic Bearings," *Artificial organs,* vol. 30, no. 5, pp. 324-338, 2006.

[113] Z. Ren, S. Jahanmir, H. Heshmat, A. Z. Hunsberger, and J. F. Walton, "Design analysis and performance assessment of hybrid magnetic bearings for a rotary centrifugal blood pump," *ASAIO Journal,* vol. 55, no. 4, pp. 340-347, 2009.

[114] E. Okamoto, Y. Ishida, T. Yano, and Y. Mitamura, "Passive magnetic bearing in the 3rd generation miniature axial flow pump-the valvo pump 2," *Journal of Artificial Organs,* vol. 18, no. 2, pp. 181-184, 2015.

[115] N. A. Greatrex, D. L. Timms, N. Kurita, E. W. Palmer, and T. Masuzawa, "Axial magnetic bearing development for the BiVACOR rotary BiVAD/TAH," *IEEE Transactions on Biomedical Engineering,* vol. 57, no. 3, pp. 714-721, 2010.

[116] T. Masuzawa, S. Ezoe, T. Kato, and Y. Okada, "Magnetically suspended centrifugal blood pump with an axially levitated motor," *Artificial organs,* vol. 27, no. 7, pp. 631-638, 2003.

[117] H. Onuma, M. Murakami, and T. Masuzawa, "Novel maglev pump with a combined magnetic bearing," *Asaio Journal,* vol. 51, no. 1, pp. 50-55, 2005.

[118] J. Asama, T. Shinshi, H. Hoshi, S. Takatani, and A. Shimokohbe, "A new design for a compact centrifugal blood pump with a magnetically levitated rotor," *Asaio Journal,* vol. 50, no. 6, pp. 550-556, 2004.

[119] J. Asama, T. Shinshi, H. Hoshi, S. Takatani, and A. Shimokohbe, "A compact highly efficient and low hemolytic centrifugal blood pump with a magnetically levitated impeller," *Artificial organs,* vol. 30, no. 3, pp. 160-167, 2006.

[120] Y. H. Kim, F. L. Lewis, & C. T. Abdallah, “A dynamic recurrent neural-network-based adaptive observer for a class of nonlinear systems”, Automatica, *33*(8), 1539-1543, (1997).